

Numerical Modelling of Ni/PU Hybrid Foams Coating Process

Dissertation

zur Erlangung des Grades
des Doktors der Ingenieurwissenschaften
der Naturwissenschaftlich-Technischen Fakultät
der Universität des Saarlandes

von

Narges Ghiasi Shirazi, M.Sc.

Saarbrücken
2024

Tag des Kolloquiums: 26.07.2024
Dekan: Prof. Dr.-Ing. Michael Vielhaber
Berichterstatter: Prof. Dr. Martin Müser
Prof. Dr. mont. Christian Motz
Akad. Mitglied: Dr.-Ing. Idriss El Azhari
Vorsitz: Prof. Dr.-Ing. Georg Frey

Abstract

Ni/PU hybrid metal foams are open-cell polyurethane foams that are coated with a nanocrystalline nickel layer via the electrodeposition process. This coating process is often challenging due to the complex geometries and mass transport limitations which lead to a heterogeneous coating thickness. To optimize the coating controlling parameters, a two-sided coupled model based on the mixture theory is developed. This model considers the multi-phase nature of the process and the main transport mechanisms, i.e. diffusion, convection, and migration, and a sink term responsible for the deposition of ions on the struts. In this model, concentration, pressure, and electric field are used as the primary variables and calculated using a system of three coupled equations. A back-coupling technique provides the gradual parameter changes, such as porosity and permeability during the process. The change in flux velocity is considered by calculating pressure from an additional Darcy equation. Moreover, by calculation of local electrical current using the Butler-Volmer equation, the deposition thickness is estimated from Faraday's law. The comparison of numerical and experimental results demonstrates the strong ability of the proposed model to describe the experimentally observed effects.

Zusammenfassung

Ni/PU-Hybridmetallschäume sind offenzellige Polyurethanschäume, die im Elektroabscheidungsverfahren mit einer nanokristallinen Nickelschicht beschichtet werden. Dieser Beschichtungsprozess ist wegen der komplexen Geometrien und Massentransportbeschränkungen, die zu einer heterogenen Beschichtungsstärke führen, oft eine Herausforderung. Zur Optimierung der Beschichtungssteuerungsparameter wird ein zweiseitig gekoppeltes Modell basierend auf der Mischungstheorie entwickelt. Dieses Modell berücksichtigt die Mehrphasennatur des Prozesses und die Haupttransportmechanismen, d. h. Diffusion, Konvektion und Migration, sowie einen Senkenterm, der für die Abscheidung von Ionen auf den Streben verantwortlich ist. In diesem Modell werden Konzentration, Druck und elektrisches Feld als Primärvariablen verwendet und mithilfe eines Systems aus drei gekoppelten Gleichungen berechnet. Eine Rückkopplungstechnik ermöglicht die schrittweise Änderung von Parametern wie Porosität und Permeabilität während des Prozesses. Die Änderung der Flussgeschwindigkeit wird durch die Berechnung des Drucks aus einer zusätzlichen Darcy-Gleichung berücksichtigt. Darüber hinaus wird durch die Berechnung des lokalen elektrischen Stroms mithilfe der Butler-Volmer-Gleichung die Beschichtungsstärke anhand des Faradayschen Gesetzes geschätzt. Der Vergleich von numerischen und experimentellen Ergebnissen zeigt, dass das vorgeschlagene Modell die experimentell beobachteten Effekte gut beschreiben kann.

Acknowledgement

The presented research has been carried out during my time as a PhD student at the Chair of Applied Mechanics, Saarland University, Saarbrücken. I would like to thank all those who have supported me during this journey.

Above all, I would like to express my deepest gratitude to my advisor Prof. Dr.-Ing. Stefan Diebels. Prof. Diebels provided me the opportunity to work in a pleasant working atmosphere, which was a turning point in my life. He generously devoted his time and knowledge to the scientific discussions and supported me patiently with invaluable guidance and insightful feedback throughout the entire research process.

I am also indebted to the members of my thesis committee, who agreed to review this work. Their constructive criticism and thoughtful suggestions have greatly enhanced the quality of my research.

I extend my thanks to the German Science Foundation (DFG), whose financial support made this research possible.

A special thanks to my colleague and friend, Dr.-Ing. Prateek Sharma who was always there whenever I needed assistance.

As an international member of the Applied Mechanics Chair dealing with German language barriers, I would like to thank all my colleagues who were supportive and kindly helped me and made the past 4 years much more enjoyable.

Finally, I would like to thank my family for their unwavering support, understanding, and encouragement. Their belief in my abilities has been a constant source of motivation.

Saarbrücken, 2024

Narges Ghiasi Shirazi

Contents

| | | |
|----------|---|-----------|
| 1 | Introduction | 1 |
| 1.1 | Motivation | 3 |
| 1.2 | Thesis Outline | 3 |
| 2 | Porous Materials and Hybrid Foams | 5 |
| 2.1 | Cellular Material | 5 |
| 2.2 | Hybrid Foams | 7 |
| 2.2.1 | Production Procedure of Ni/PU Hybrid Foams | 8 |
| 2.3 | Influencing Factors in Electrodeposition/ Background and Shortcomings | 10 |
| 3 | Theory and Material Model | 13 |
| 3.1 | Fundamentals of Mixture Theory | 14 |
| 3.1.1 | Kinematics | 14 |
| 3.1.2 | Balance Equations | 17 |

| | | |
|----------|---|-----------|
| 3.2 | Modelling the Coating Process of Ni/PU Hybrid Foams | 19 |
| 3.2.1 | Kinematics and Balance Equations | 21 |
| 3.2.2 | Simplifying Assumptions and Constitutive Equations | 23 |
| 3.2.3 | Back-coupling and Coating Thickness Formulation | 29 |
| 4 | Numerical Implementation | 35 |
| 4.1 | Finite Difference Method (FDM) | 36 |
| 4.1.1 | Solving the System of Discrete Equations | 40 |
| 4.1.2 | Predictor-Corrector Step: Runge-Kutta Method | 41 |
| 4.1.3 | Convergence, Stability, and Consistency | 43 |
| 4.2 | Transformation to Normalized Form | 45 |
| 5 | Results and Discussion | 47 |
| 5.1 | Validation of the Developed FDM Code | 48 |
| 5.1.1 | Reaction: Sink | 49 |
| 5.1.2 | Diffusion | 50 |
| 5.1.3 | Convection and Migration | 54 |
| 5.2 | Implementing the Model on a One-Dimensional Domain | 59 |
| 5.2.1 | Influence of Input Parameters | 62 |
| 5.2.2 | Influence of Back-Coupling Calculations | 66 |
| 5.2.3 | Influence of Diffusion and Convection Intensities | 69 |

| | | |
|----------|---|-----------|
| 5.2.4 | The Solution to the Full Two-Sided Model | 72 |
| 5.2.5 | Convergence Study | 76 |
| 5.3 | Modelling the Ni/PU Coating Process: Simulation vs. Experiment | 79 |
| 5.3.1 | Numerical Simulation: Global Results | 83 |
| 5.3.2 | Numerical vs. Experimental Results: Global Coating Thickness Distribution | 87 |
| 5.3.3 | Numerical vs. Experimental Results: Local and Semi-local Coating Thickness Distribution | 89 |
| 5.3.4 | Numerical vs. Experimental Results: Investigation of Flow | 92 |
| 6 | Conclusion and Future Works | 95 |
| 6.1 | Conclusion | 95 |
| 6.2 | Outlook | 97 |

1

Introduction

The study of mass transport and reaction of fluids in natural and synthetic porous media is an interesting research topic encountered in a wide range of engineering and industrial problems, from oil extraction and petroleum industry to the chemical processes involving catalysts, development of electrodes and batteries [1, 2].

Porous materials are a class of materials typically characterized by their unique structures and properties, such as pore size distribution, internal surface area, and comprising material. Due to their potential to deal with various technological challenges, these materials are suitable for specific applications, including energy storage and insulation, filters, and biomedical implants [3–5]. However, their application is often limited by their poor mechanical strength, stability, and bio-compatibility. As a result, the field of porous materials research has been rapidly growing and advancing. Metal coating via electrodeposition offers a solution to some of these challenges by creating a conformal coating on the surface of the open-cell porous foams, commonly known as hybrid metal foams, which can improve the mechanical and geometrical properties of the original substrate material [6].

Electrodeposition ion coating, also known as electroplating, is a process in which a metal ion is reduced and deposited onto a conductive surface to form a thin layer of metal. The thickness and quality of the coating can be con-

trolled by adjusting different process parameters such as the electric current, the flow of electrolyte, the concentration of the metal ions in the solution, and the duration of the process. However, the surface modification of open-cell foams using this coating technique is often challenging due to the complex geometries and large internal surface areas of these materials [7, 8]. Furthermore, the mass transport limitations [9–11] lead to a non-homogeneous coating thickness which affects the efficiency of these hybrid foams.

To overcome these limitations, modelling and simulation techniques have been developed to study and optimize this process. In this context, simulation offers a powerful tool to investigate the underlying mechanisms and optimize the coating controlling parameters for an improved performance. Moreover, understanding the flow behaviour through open-cell porous materials is of great importance to be able to expand their applications and develop new efficient materials.

The mass transport through the open-cell foam in the electrodeposition process is governed by a highly non-linear coupled system. The flow in these processes is controlled by multiple mechanisms: the convection of the fluid is realised by a pump, which produces a pressure gradient; the migration of the ions is realised by an electrical current, which is produced by an electrical potential gradient; and the diffusion of ions is realised by different ion concentrations at the inlet and outlet of the foam. Furthermore, by the deposition of ions on the struts and the foam's geometrical evolution, an additional sink term for the ions is introduced which complicates the problem further [12, 13].

In order to get a better perception of the electrodeposition process and a general understanding of flow behaviour inside the porous medium, the first necessary step is to develop a quantitative model at the macroscale. This model should be built in such a way that it takes into account all the main transport mechanisms as well as the multi-phase nature of the process. In this regard, mixture theory provides an appropriate mathematical framework to deal with such complex problems.

Mixture theory is a branch of continuum mechanics used to describe and analyse the behaviour of heterogeneous materials which are made up of multiple constituents or phases, each with their own distinct properties and behaviour that affect the overall behaviour and deformation of the system. The main idea is to consider the entire system as superimposed continua and deal with each phase as a separate continuum with its own governing equations. These equations take into account the interactions between the constituents, such as the exchange of mass, momentum, and energy. Hence, the overall behaviour of the material is the result of the superposition of individual behaviours of each constituent [14–16].

1.1 Motivation

The focus of this study is to numerically model the coating process of polyurethane foams with nanocrystalline nickel via electrodeposition, which leads to the production of Ni/PU hybrid foams. These hybrid foams not only have lightweight features of highly porous solids and an increased strength due to nickel coating but they also are economical in comparison to similar metal foams. However, some difficulties emerge during the production of Ni/PU foams such as heterogeneous coating thickness due to mass transport limitations which leads to a heterogeneous distribution of the mechanical properties. To improve the production procedure, leveraging the results of numerical simulations can be valuable.

A mathematical model has been developed which is able to describe the flow behaviour within the electrodeposition process. It is a two-sided coupled model based on the mixture theory on a macroscopic scale which can give an insight on the parameter changes under the influence of coating. In this model, concentration, pressure and electric field can be calculated using a system of three coupled equations. With the help of a back-coupling technique, the changes of parameters in each iteration have been taken into account for the calculation of parameters in the next iteration. Moreover, by calculation of local electrical current using the Butler-Volmer equation, the thickness of deposition can be estimated from Faraday's law.

The obtained system of equations has been solved numerically with the help of the Finite Difference Method (FDM). Subsequently, the numerical results have been compared with the experimental results to evaluate the performance and efficiency of the proposed model. The desired goal is to improve the experimental results by proposing suitable values for different parameters based on the simulations' predictions.

1.2 Thesis Outline

This study, from the introductory chapter to the conclusive findings, has been structured and organized into 6 chapters as follows:

After a short introduction on the motivation of the present study in **Chapter 1**, a brief literature review on porous materials and hybrid foams is given

in **Chapter 2**. The electrodeposition process and the influencing factors in this process are discussed to provide a general perspective on the subject. The encountered problems are also mentioned so that the necessity of the present study can be realized.

The fundamentals of mixture theory required for modelling the desired problem are explained in **chapter 3**. In this chapter, a mathematical model in the framework of continuum mechanics is proposed which defines the problem in terms of process variables and describes different transport mechanisms in the electrodeposition process.

In **chapter 4**, the numerical schemes used to approximate the obtained partial differential equations are explained. The accuracy of these numerical approaches is validated in **Chapter 5** and the efficiency and performance of the method are investigated. Furthermore, by solving some 1D and 2D examples, the applicability of the proposed model is evaluated. These approximated results are then compared with the corresponding experimental measurements to perform a suitable parameter identification. Finally, the thesis is completed in **chapter 6**, by discussing the findings of the work and proposing potential ideas for further improvements of the model.

2

2.1 Porous Materials and Hybrid Foams

2.1 Cellular Material

Cellular materials or foams are continuously interconnected frameworks of materials that contain void spaces or pores. Hence, they are also simply called porous materials. They exist widely in nature, in different forms and materials. They can exist in gaseous, liquid, or solid form. Galaxies and beer foam can be mentioned as an example for the first two forms, respectively [17]. However, the most common form is the solid form, which is abundantly found in nature and has increasingly been utilized across various industries. Cellular solids are made up of a solid phase which is in fact the interconnected porous network of solid struts or plates that forms the edges and faces of pores or cells, and a fluid phase that fills these pores.

Porous materials can be categorized based on different aspects. They can be classified into *natural* and *artificial* porous materials. Human bones, wood, cork, pumice, and lava are some examples of natural porous media that are also very applicable in different engineering areas [3]. Inspired by nature, scientists started to mimic the same structure to produce man-made or bio-inspired cellular materials [4, 5].

Another classification can be done based on the cell type, which introduces *open-cell* and *closed-cell* foams. The first group consists of interconnected pores that are permeable and have a very high internal surface area. On the other hand, the pores in closed-cell structures are isolated from each other by thin solid membranes [4, 5, 18].

Based on cell size and the number of pores (i.e., porosity), they can be classified as *low*, *middle* or *high* porosity structures [4, 5, 18].

Porous materials can also be categorized based on their structure. Those consisting of regular cellular structures which can be characterized by a unit cell, introduce the *periodic* cellular structure. However, in *stochastic* structures, one observes a random distribution of pores with non-uniform pore and strut dimensions [4, 5, 18].

Due to their unique topology and depending on the base material, porous materials possess special characteristics that make them suitable to be used for many purposes. The most significant property of these materials is their multi-functional light-weight structure, which in combination with their other properties like high specific strength and structural rigidity, thermal and acoustic insulation, energy absorption capacity, and vibrational damping make them an interesting material in many fields of engineering like aerospace and automotive industries, biomedical implants and construction applications [3]. Furthermore, permeability and a large internal surface area especially in open-cell foams, make these materials perfect candidates to be used as filters, heat exchangers, electrodes, batteries, and bearings [4, 5].

Common materials used to manufacture cellular solids are metals, polymers, and ceramics. Polymer foams are the most commercialized variety [17]. In spite of the many advantages of polymer foams like low relative density, excellent performance of heat and sound insulation, and good energy absorption, it is difficult for them to fulfill conditions where high strength, high energy absorption capacity, and high temperature tolerance are needed simultaneously. Porous metals, however, not only have the typical characteristics of metals like weldability and electrical conductivity but also can meet the above-mentioned characteristics [5]. However, problems such as their expensive manufacturing process and bad reproducibility may result in the limited application of metal foams [19]. Due to the increasing applications of porous metals over the past years, great attention was drawn to the improvement of their different production procedures and the improvement of the resulting properties. Many innovations were proposed in this field. Two reinforced types of these materials have been developed, namely cellular composites and cellular nanocomposites. Furthermore, by combining different materials (e.g. polymer and metal) hybrid foams can be produced which enhance the multi-functionality of individual foams [4–6].

Hybrid metal foams are one of the suggested solutions that could partially compensate for the mentioned shortcomings. Hybrid metal foams are basically open-cell foams that are coated by a metallic layer via an electrodeposition process [6, 20]. The major advantages of this method are twofold: First, the properties of the foam can be improved based on the mechanical properties of the chosen coating material and by tailoring the coating thickness. Second, based on the material of the template, the manufacturing costs can be significantly reduced [7].

In the following subsection, a comprehensive overview of these materials, including an in-depth explanation of their manufacturing procedures is provided.

2.2 Hybrid Foams

With the increasing interest in the application of cellular material in different engineering fields, the necessity to optimize these materials started to gradually draw the attention of many scientists. As such, it was suggested to treat the base foam with a metal coating to produce the hybrid foams. The main idea behind these new materials is to develop new properties by eliminating the weaknesses of each individual component and taking advantage of their strong points. One of the recent types of hybrid foams is the polyurethane foam that is coated with nanocrystalline nickel which is briefly referred to as Ni/PU hybrid foam. The main advantages of these hybrid foams are that they possess the light-weight characteristics of highly porous solids and an increased strength due to nickel coating while being economical in comparison to similar metal foams. Jung and Diebels [7] showed that Al and PU hybrid foams coated with nickel have similar mechanical properties but Ni/Al is more expensive per volume by an order of magnitude.

One of the methods to produce Ni/PU foams is the electrodeposition method. Electrodeposition ion coating, also known as electroplating, is a process in which a metal ion is reduced and deposited onto a conductive surface to form a thin layer of metal. In the following the production procedure of Ni/PU hybrid foams using electrodeposition is described step by step.

2.2.1 Production Procedure of Ni/PU Hybrid Foams

Electrochemical deposition, or shortly electrodeposition, is a conventional process that uses an electric current to form a thin layer of metal coating on the surface of a conductive material. In this process positively charged desired metal ions (cations), which are dissolved in the electrolyte, are deposited on the surface of the substrate connected to the negatively charged electrode (cathode) by the passage of electric current. Electrodeposition has been a subject of interest to metallurgists due to its capability to produce new materials with modified properties in any arbitrary three-dimensional geometries. Comprehensive studies on the production of hybrid foams via electrodeposition method have been carried out by Jung et al. [6, 7, 19–21] and they improved the coating process significantly compared to the former studies by Bouwhuis et al. [22], Boonyongmaneerat et al. [23] and Sun et al. [24–26]. Jung et al. investigated the metal coating of metallic and polymeric substrates and compared their mechanical properties with each other as well as their own properties before and after coating. Jung et al. [7, 8] were among the first who used an electrodeposition process to produce Ni/PU hybrid foams and compared the advantages of this method with conventional production methods like chemical vapor deposition (CVD) or electroless plating. Since the focus of this study is the Ni/PU foams, in the following the electrodeposition process for these hybrid foams is described.

Pretreatment of Polyurethane Foams

For the electrodeposition process, it is required for the substrate to be electrically conductive so that it can be coated by an electrodeposition process. However, polyurethane is a non-conductive polymer that needs a special pretreatment procedure. So, the first step is to make PU foams electrically conductive by dip-coating the open-cell foams in a conductive graphite lacquer. To remove the excess lacquer from the pores and struts, a compressed airflow is blown through the foams [8, 13]. The dip-coated foam is used as a template for the Ni/PU foam in the electrodeposition process.

Electrodeposition Process

The aqueous nickel sulfamate electrolyte contains Ni^{2+} ions as nickel source for the coating process. During the deposition process, the electrolyte is kept at a constant temperature of $50^{\circ}C$. In the beginning, in the absence of an electrical current, the porous template is plunged into the aqueous electrolyte with homogeneously distributed nickel ions and connected to the cathode. It is assumed that the electrolyte is supplied with an infinite nickel ion source with the concentration C_{∞} , realized by two sacrificial anodes on both sides of the foam, according to Fig. 2.1 [21]. These anodes carry spherical nickel pellets and they are covered with a layer of non-woven fabric to avoid sludge contamination into the electrolyte [8].

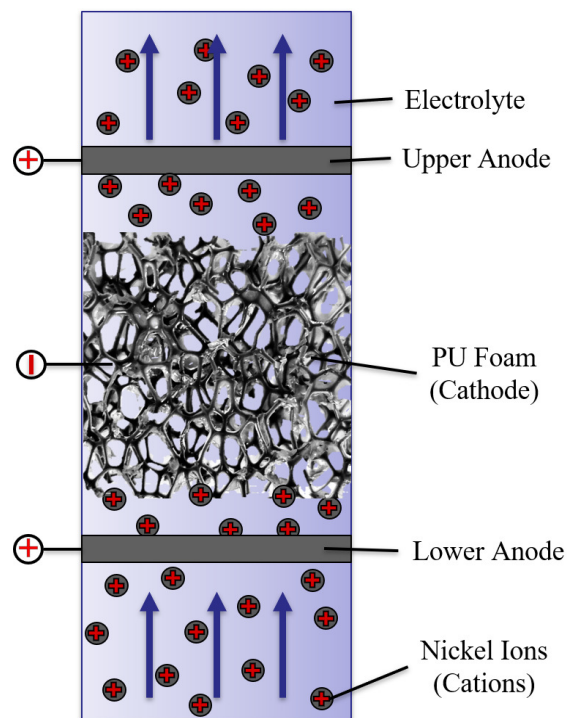


Figure 2.1: Schematic representation of the electrodeposition reactor.

The cylindrical carbon-coated PU foam with the diameter of 210 mm and thickness of 40 mm, is connected to the cathodic pole of the power supply using four insulated cables. Under an applied external electrical current density of 16.5 mA/cm^2 , positively charged nickel ions (cations) migrate to the

polyurethane substrate (cathode), where they are discharged and deposited as metallic nickel layer according to:



This leads to a decreasing ion concentration in the electrolyte filling the pores of the foam. The resulting inhomogeneity in concentration is reduced by the diffusion of ions in the electrolyte. A pump has also been used to drive the flow and to distribute the ions in the foam more homogeneously by convection, when pure diffusion is too slow due to low concentration gradient [8, 21].

As a result of the reaction, two zones with different ion concentration will be developed in the electrolyte. One far away from the cathode (substrate) with constant concentration C_{∞} , and the other zone in the vicinity of the cathode with lower concentration. Hence, the mass transport is required to compensate for the decrease in the ion concentration close to the substrate driven by the deposition process. The mass transport is mainly governed by three processes, namely migration, convection, and diffusion due to the existence of the electrical field, pump, and concentration gradient in the electrolyte, respectively. Moreover, nickel ions react with the electrons on the foam cathode, forming a metallic coating layer and hence introducing a sink term for the ions in the electrolyte which is the responsible term for the coating process [13].

2.3 Influencing Factors in Electrodeposition/ Background and Shortcomings

Properties of the electrodeposited layer are under the influence of many factors. The duration of deposition, current density, solution concentration, pressure and velocity of the flow, and the geometry and properties of the substrate are among the important factors that determine the quality, thickness, and homogeneity of the coating. One of the most common problems in coating of porous materials is the mass transport limitation during the electrodeposition process which leads to inhomogeneity of the coating throughout the foam. Improving the experiments requires very time- and money-consuming

trials and errors if one wants to depend only on the experimental results. Therefore, it is important to reach a numerical model which can describe the process precisely. The goal is to use the model to improve the experiment in order to achieve a homogeneous distribution of the coating thickness which results in homogeneous mechanical properties.

Understanding the flow behaviour through the porous medium is one of the most important steps in developing such a model. K. Terzaghi presented the first study of flow through porous materials in 1925 [27]. Since then, the attention of many scientists has been drawn to different problems regarding porous materials. M. Biot followed the scientific works of Terzaghi and developed porous media theories partly based on mechanical principles and mainly based on ensured experimental data [28]. His extensive work in poroelasticity, known as Biot's theory, has been fundamental in understanding the coupled behaviour of fluid flow and deformation in compressible porous materials [29]. M. Hassanizadeh derived the basic equations of mass transport in porous media using classical balance equations [30]. By further simplifications and linearizations of constitutive equations and balance laws, he obtained general extensions of Darcy's and Fick's laws, applicable to the cases where the fluid has more than one main component [31]. In another study, M. Hassanizadeh and W. G. Gray developed a systematic procedure for averaging continuum equations over representative regions of multi-phase systems [32–35]. M. Miyan and P. Pant investigated the multi-phase flow in porous rocks and derived the diffusion equation and the related Darcy's law [36]. Hiltunen et al. gave a comprehensive review of the theory of multi-phase flows, analysed different mixture models and suggested closure approaches [37].

Mixture theory is amongst the most common approaches that has been used to model the flow through porous media. The first works on the mixture theories were initiated by C. Truesdell [16, 38–40] who presented a systematic construction of a continuous approach to multi-component fluid systems [41]. Later on, this purely mechanical model was extended by other authors such as I. Müller [42] and R. M. Bowen [14]. Bowen developed field theories for mixtures and discussed the mathematical foundations of non-linear mechanical, electrical, and magnetic phenomena that take place in mixtures [14]. W. Ehlers and J. Bluhm [15] gathered various developments in the theory of porous media including the basic theoretical concepts in continuum mechanics on porous and multi-phasic materials as well as the wide range of experimental and numerical applications. Subsequently, it has been widely used in various fields of engineering, including chemical engineering and materials science and particularly in analysing complex materials such as porous materials that exhibit non-homogeneous behaviour [15, 43–49] and

has proven particularly useful in modelling such problems.

Regarding the current study on the production of hybrid foams via electrodeposition process, a handful of studies on different aspects of this subject have been performed. Hughes et al. [50] developed the equations for modelling electrodeposition under forced convection and used numerical algorithms to set up a simulation. Joekar-Niasar et al. [51] investigated the coupled hydrodynamic and electrochemical interactions caused by the presence of charged solid surfaces, ions in the fluid, and chemical reactions between the ions in the fluid and the solid surface. However, there are only a few studies on the simulation of the coating of complex structures like porous materials. Grill et al. [52, 53] numerically simulated the electroplating process of open-cell foams and investigated the influence of electrodeposition parameters. In another study, Grill et al. [13] simulated the electrodeposition process of nickel ions on polyurethane foams and investigated the homogeneity of the coating thickness and, finally, compared the numerical results with the experimental data. The model that was developed by Grill et al. is based on the Nernst-Planck equation, where they deal with a one-sided coupled electrodeposition process. In their model, they assume constant values for process parameters such as velocity and electrical field as well as geometrical parameters such as porosity and permeability. However, in the real process, the changes in the coating thickness cause changes in the geometry of the foam which means changes in the surface, permeability and porosity which in turn results in a change in the flow behaviour. Therefore, the purpose of this study is to obtain a precise numerical coupled model which can describe the flow behaviour inside the porous medium and takes into account all the structural and physical changes during the coating process.

3

Theory and Material Model

Modelling the flow behaviour through a porous medium requires a formulation in the framework of multi-phase continuum mechanics. In these types of problems, the representative elementary volume (REV) under study is no longer a single continuous material, but it rather consists of two or more constituents which simultaneously occupy the same macroscopic position in the current configuration, leading to the concept of superimposed continua. On that account, the problem is investigated in the framework of mixture theory [14, 15, 49, 54]. This theory is combined with the concept of volume fractions and yields a consistent framework to describe different fields and properties.

Mixture theory is developed based on the continuum mechanics assumptions. It consists of three main concepts namely, kinematics, balance equations, and constitutive equations. The first two are general statements describing deformation, motion, and material body interactions with its surroundings. They are universal laws of nature for every system. Whereas, constitutive equations are particular statements related to individual material properties [14, 15, 55, 56].

Following the concepts of mixture theory, e.g. Trussdell [16], Bowen [14] and etc., the required basic definitions of mixture theory are presented in section 3.1. Then, the mathematical model for our specific desired problem is devel-

oped and the governing partial differential equations are derived to be used in numerical simulations.

3.1 Fundamentals of Mixture Theory

3.1.1 Kinematics

Consider n material bodies \mathcal{B}^i , each of which is composed of an infinite set of continuously distributed material points, as shown in Fig. 3.1.

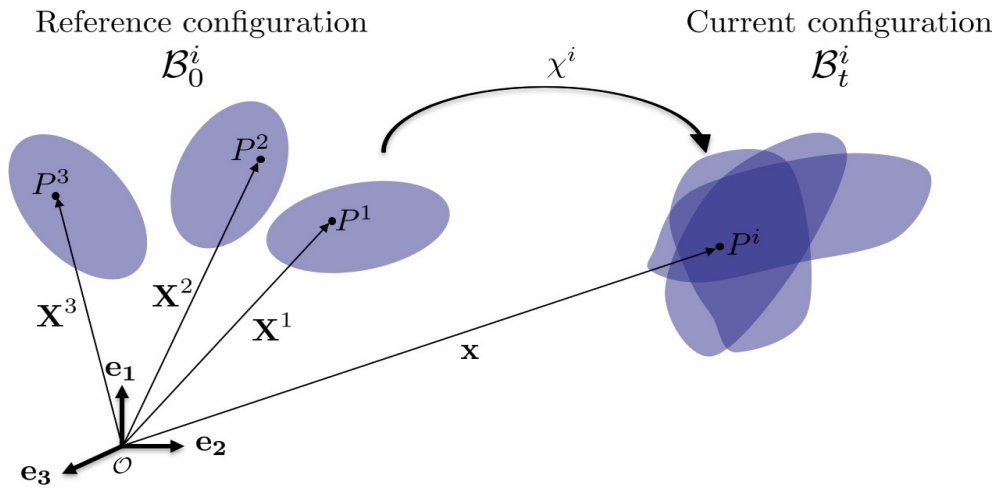


Figure 3.1: Schematic representation of n material bodies \mathcal{B}^i in the reference and current configurations. Each spatial position \mathbf{x} is occupied by different material points P^i .

Each of these material points are carriers of different physical properties and can be uniquely identified by the position they occupy, at a chosen reference time t_0 . By choosing the reference configuration at time $t = t_0$ as the fixed configuration, one can define the motion function χ to describe the mapping of the material body \mathcal{B}^i ($i = 1, \dots, n$) from the reference configuration to the

current configuration, as:

$$\mathbf{x} = \boldsymbol{\chi}^i(\mathbf{X}^i, t) \quad (3.1)$$

where \mathbf{X}^i is the position of a material point of the i th material body in its reference configuration or material configuration, t is the time, and \mathbf{x} is the spatial position occupied at the time t by the material point labeled P^i .

A fundamental assumption in mixture theory is that for a mixture, individual components of the mixture can be modeled by superimposed continua. Therefore, each spatial position \mathbf{x} in the current configuration of the mixture is occupied simultaneously by n material points, one from each material body, as shown in Fig.3.2. Therefore, the definition of the mixture is always concerning the current configuration.

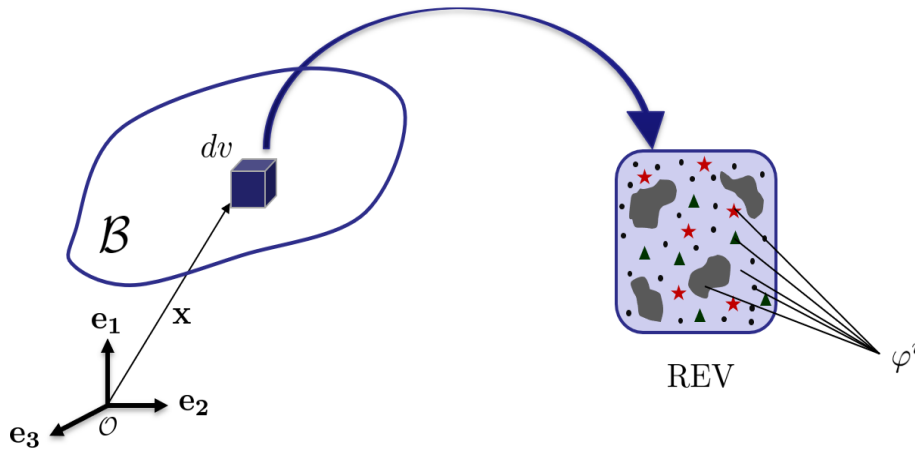


Figure 3.2: Schematic representation of a material body \mathcal{B} . Each spatial position \mathbf{x} is occupied simultaneously by n constituent φ^i .

Different properties can be defined for each constituent i ($i = \{1, \dots, n\}$) occupying the same material point \mathbf{x} .

The real or intrinsic density ρ^R (kg/m^3) of each constituent i is defined as:

$$\rho^{iR}(\mathbf{x}, t) = \frac{dm^i}{dV^i} \quad (3.2)$$

where dm^i and dV^i are the mass and occupied volume of i th constituent. On the other hand, the partial density ρ (kg/m^3) of each constituent can be defined as the ratio of its mass to the total volume of the mixture, as shown

in equation 3.3:

$$\rho^i(\mathbf{x}, t) = \frac{dm^i}{dV} = \frac{dV^i}{dV} \rho^{iR}(\mathbf{x}, t) \quad (3.3)$$

By summing over the densities of all the constituents, the total density of the mixture at point \mathbf{x} and time t is obtained as:

$$\rho(\mathbf{x}, t) = \sum_{i=1}^n \rho^i(\mathbf{x}, t) \quad (3.4)$$

The mass concentration c of the i th constituent at (\mathbf{x}, t) is defined as:

$$c^i(\mathbf{x}, t) = \frac{\rho^i}{\rho} \quad (3.5)$$

It is evident from equation 3.4 that:

$$\sum_{i=1}^n c^i = 1 \quad (3.6)$$

Similarly, the volume fraction n of each constituent can be defined as:

$$n^i = \frac{dV^i}{dV} \quad (3.7)$$

which leads to the saturation condition of equation 3.8, since there is no vacant space in the overall REV.

$$\sum_{i=1}^n n^i = 1 \quad (3.8)$$

Different velocities can be defined for the mixture as a whole and for each constituent. The mixture mean velocity \mathbf{v} at (\mathbf{x}, t) is the velocity of its center of mass which is defined by:

$$\mathbf{v}(\mathbf{x}, t) = \frac{1}{\rho} \sum_{i=1}^n \rho^i \mathbf{v}^i(\mathbf{x}, t) = \sum_{i=1}^n c^i \mathbf{v}^i(\mathbf{x}, t) \quad (3.9)$$

where, \mathbf{v}^i is the velocity of each constituent (m/s).

Another velocity defined in mixture theory is *diffusion velocity*, \mathbf{d} , which is the relative velocity of constituent i with respect to the center of mass of the mixture and is formulated as:

$$\mathbf{d}^i(\mathbf{x}, t) = \mathbf{v}^i(\mathbf{x}, t) - \mathbf{v}(\mathbf{x}, t) \quad (3.10)$$

Using equations 3.9 and 3.10 along with equation 3.4, it is concluded that:

$$\sum_{i=1}^n \rho^i \mathbf{d}^i(\mathbf{x}, t) = \mathbf{0} \quad (3.11)$$

3.1.2 Balance Equations

As can be seen in the previous section, kinematics serves to describe the geometry, motion, and deformation of a material body. The next step is to consider the interactions of the material body with the outside world which is done with the help of balance equations. These statements which exist in global and local formulations, describe the temporal change of a material body's property at its current configuration. According to Trussdell's metaphysical principles [16], the balance equations of individual constituents are identical to the balance equations of a single-phase continuum except for the local interactions of the constituents. These interactions are taken into account by appropriate production terms. In the following, the local axioms of balance equations of mass and momentum for a mixture are briefly discussed.

Balance of Mass

The mass balance axiom implies the conservation of the total mass within the mixture. Thus, in the presence of chemical reactions, phase change, or deposition, the mass of each constituent would change in such a manner that the total mass of the mixture remains constant. The local form of mass balance for each constituent i is defined as:

$$\partial \rho^i / \partial t + \operatorname{div}(\rho^i \mathbf{v}^i) = \hat{\rho}^i \quad (3.12)$$

In equation 3.12, the quantity $\hat{\rho}^i$ is called the *mass supply* (kg/m³ s) of constituent φ^i , $i = \{1, \dots, n\}$ and it represents the rate of mass supplied to the i th constituent from the other constituents in the same spatial position.

The local mass balance for the mixture as a whole can be obtained by summation of the mass balances of all constituents. Moreover, according to the mass conservation principle, the total mass of the system remains constant and there will be no total mass production. Hence, the right-hand side of the equation should be equal to zero.

$$\partial\rho/\partial t + \text{div}(\rho\mathbf{v}) = 0 \quad (3.13)$$

In these equations, $\frac{\partial}{\partial t}$ is the partial derivative with respect to the time, and $\text{div}(\bullet)$ is divergence with respect to the Eulerian system, related to the gradient operator defined as:

$$\text{grad}(\bullet) = \frac{\partial(\bullet)}{\partial\mathbf{x}} \quad (3.14)$$

Since the mass of the mixture should remain unchanged, the total amount of mass supply in the mixture is equal to zero. Hence, comparing the two equations 3.12 and 3.13, it is evident that:

$$\sum_{i=1}^n \hat{\rho}^i = 0 \quad (3.15)$$

Balance of Momentum

Balance of momentum states that the resultant forces acting on a material body cause a change in its linear momentum. The local form of the momentum balance for each constituent i is defined as:

$$\frac{\partial(\rho^i\mathbf{v}^i)}{\partial t} + \text{div}(\rho^i\mathbf{v}^i \otimes \mathbf{v}^i) = \text{div}\boldsymbol{\sigma}^i + \rho^i\mathbf{g} + \hat{\mathbf{s}}^i \quad (3.16)$$

where $\boldsymbol{\sigma}^i$ is the partial stress tensor (Pa), \mathbf{g} is the external body force (e.g. gravity) (m/s²) and $\hat{\mathbf{s}}^i$ is the complete local interaction of the constituents

(kg/m² s²). This term consists of two parts:

$$\hat{\mathbf{s}}^i = \hat{\mathbf{p}}^i + \hat{\rho}^i \mathbf{v}^i \quad (3.17)$$

where $\hat{\mathbf{p}}^i$ is called the *momentum supply* (kg/m² s²) which accounts for the change of momentum of a phase due to stresses imposed on it by the other phases, and the second term is the resulting momentum induced by the mass exchange between the constituents. By applying the differentiating operator on the first product term on the left-hand side of equation 3.16 and by substituting equation 3.17 in 3.16, it is concluded that:

$$\rho^i \frac{\partial \mathbf{v}^i}{\partial t} + \rho^i \text{grad} \mathbf{v}^i \cdot \mathbf{v}^i + \left[\frac{\partial \rho^i}{\partial t} + \text{div}(\rho^i \mathbf{v}^i) - \hat{\rho}^i \right] \mathbf{v}^i = \text{div} \boldsymbol{\sigma}^i + \rho^i \mathbf{g} + \hat{\mathbf{p}}^i \quad (3.18)$$

The term in the bracket is equal to zero, as indicated by equation 3.12. Hence, the local forms of momentum balance for each constituent i and for the mixture as a whole are written as follows, respectively:

$$\rho^i \frac{\partial \mathbf{v}^i}{\partial t} + \rho^i \text{grad} \mathbf{v}^i \cdot \mathbf{v}^i = \text{div} \boldsymbol{\sigma}^i + \rho^i \mathbf{g} + \hat{\mathbf{p}}^i \quad (3.19)$$

$$\rho \frac{\partial \mathbf{v}}{\partial t} + \rho \text{grad} \mathbf{v} \cdot \mathbf{v} = \text{div} \boldsymbol{\sigma} + \rho \mathbf{g} + \hat{\mathbf{p}} \quad (3.20)$$

3.2 Modelling the Coating Process of Ni/PU Hybrid Foams

To obtain a numerical representation of the mentioned electrodeposition process in section 2.2.1, it is important to choose a method that can depict the highly coupled governing interactions between different phases of the problem. On the other hand, due to complexities arising from the multi-scale characteristic of the problem, it is necessary to simplify the model as much as possible and only consider the essential features in the macroscale without going into exact microscale mechanical and geometrical details. Therefore, mixture theory gives an appropriate framework for the development of such

a mathematical model.

Consider the REV shown in Fig. 3.3. In this figure, the spatial position \mathbf{x} in the mixture is occupied simultaneously by three constituents. The domain in the current configuration is occupied by a solid phase, φ^s , which is in fact the porous skeleton, and a fluid phase, φ^f , which fills the pores. The fluid phase, i.e. the electrolyte, itself is assumed to be a two-component phase, namely water, φ^w , and nickel ions, φ^{ni} . For the sake of simplicity, the other constituents in the fluid phase are neglected.

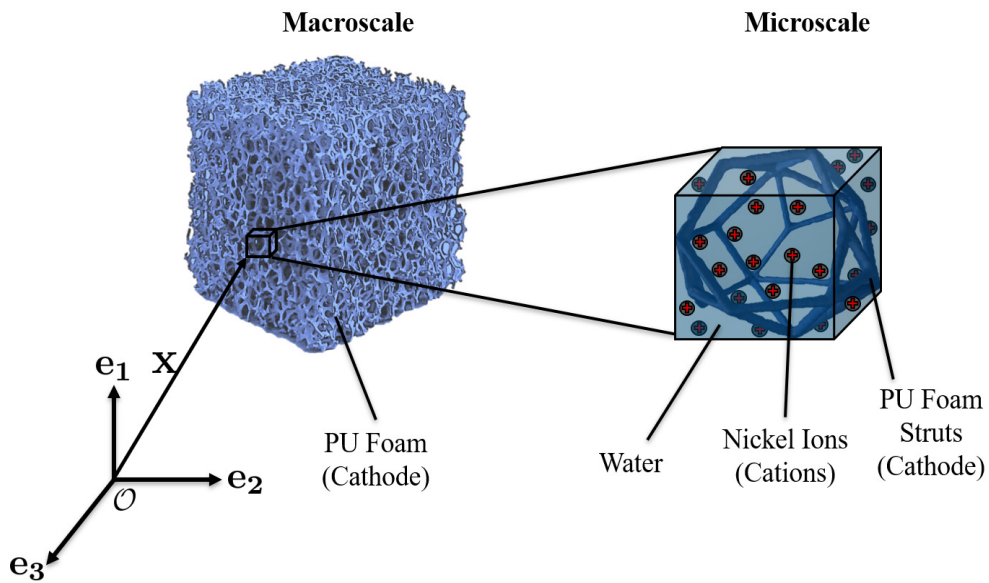


Figure 3.3: Schematic representation of the problem as a 3-phase mixture. A material point on the macroscale can be resolved on the microscale by an REV.

Following the continuum's mechanics scheme for mixtures [14, 15, 49, 54], the first step is to specify the kinematics and field equations. Then by defining appropriate constitutive equations and considering simplifying thermodynamically admissible assumptions, the final closed set of governing equations for this particular mixture model can be obtained.

3.2.1 Kinematics and Balance Equations

According to Fig. 3.3, each position \mathbf{x} at time t is simultaneously occupied by material points \mathbf{X}^s , \mathbf{X}^w and \mathbf{X}^{ni} . Each constituent follows its own function of motion at each time t as follows:

$$\mathbf{x} = \boldsymbol{\chi}^s(\mathbf{X}^s, t) = \boldsymbol{\chi}^w(\mathbf{X}^w, t) = \boldsymbol{\chi}^{ni}(\mathbf{X}^{ni}, t) \quad (3.21)$$

The volume element dV in the current configuration contains the mass of all the constituents.

$$dm = dm^s + dm^w + dm^{ni} \quad (3.22)$$

Hence, the total density is defined in terms of the partial densities of each constituent, as follows:

$$\rho = \frac{dm}{dV} = \frac{dm^s}{dV} + \frac{dm^w}{dV} + \frac{dm^{ni}}{dV} = \rho^s + \rho^w + \rho^{ni} = \rho^s + \rho^f \quad (3.23)$$

where ρ^f is the partial density of the fluid phase.

Based on the definition of volume fraction in equation 3.7, the *porosity* can be defined as the volume fraction of the pore space which is equivalent to the volume fraction of the fluid part.

$$n^f = \frac{dV^f}{dV} \quad (3.24)$$

Therefore, equation 3.3 leads to:

$$\rho^f = n^f \rho^{fR} \quad (3.25)$$

According to equation 3.9, the mixture mean velocity is defined as:

$$\mathbf{v}(\mathbf{x}, t) = \frac{1}{\rho} (\rho^s \mathbf{v}^s + \rho^w \mathbf{v}^w + \rho^{ni} \mathbf{v}^{ni}) \quad (3.26)$$

Based on the above-mentioned definitions and according to equation 3.12, the mass balance equation for each constituent can be written as follows:

$$\partial\rho^s/\partial t + \text{div}(\rho^s\mathbf{v}^s) = \hat{\rho}^s \quad (3.27)$$

$$\partial\rho^w/\partial t + \text{div}(\rho^w\mathbf{v}^w) = 0 \quad (3.28)$$

$$\partial\rho^{\text{ni}}/\partial t + \text{div}(\rho^{\text{ni}}\mathbf{v}^{\text{ni}}) = \hat{\rho}^{\text{ni}} \quad (3.29)$$

The mass balance equation for the total system can be obtained by summing the mass balances of each constituent (equations 3.27, 3.28, and 3.29).

$$\partial\rho/\partial t + \text{div}(\rho\mathbf{v}) = \hat{\rho}^s + \hat{\rho}^{\text{ni}} = 0 \quad (3.30)$$

As it is evident, the total mass of the system should remain constant and there should be no mass production in the whole mixture. Therefore,

$$\hat{\rho}^s = -\hat{\rho}^{\text{ni}} \quad (3.31)$$

That means that the deducted amount of nickel ions from the electrolyte is deposited on the solid and will further contribute to the solid's mass.

The mass balance equation for the fluid phase (water + nickel) is obtained by summing equations 3.28 and 3.29.

$$\partial\rho^f/\partial t + \text{div}(\rho^f\mathbf{v}^f) = \hat{\rho}^{\text{ni}} \quad (3.32)$$

Likewise, using equation 3.19 the momentum balance equation for the fluid phase can be written as:

$$\rho^f \frac{\partial \mathbf{v}^f}{\partial t} + \rho^f \text{grad} \mathbf{v}^f \cdot \mathbf{v}^f = \text{div} \boldsymbol{\sigma}^f + \rho^f \mathbf{g} + \hat{\mathbf{p}}^f \quad (3.33)$$

The solid phase is assumed to be rigid, stationary, and without deformation. According to the assumption of a rigid solid phase, the momentum balance of the solid phase is not further investigated.

3.2.2 Simplifying Assumptions and Constitutive Equations

So far, the fundamental kinematic and kinetic laws, describing the general state of the considered problem have been demonstrated. The last step in developing a mathematical model is to characterize the interactions between different constituents and to consider further simplifying assumptions.

The process can be described by defining appropriate constitutive equations for the fluid flux. It consists of a diffusion and migration part which can be described by Fick's law and a pressure-driven (convective) part that is described by a generalized Darcy's law.

The forces acting on the mixture are assumed to be composed of a hydrostatic pressure, which exerts a compressing normal stress, and a part which produces shear stresses. Hence, the stress tensor applied on the fluid phase is defined as:

$$\boldsymbol{\sigma}^f = -n^f p \mathbf{I} + \boldsymbol{\tau}^f \quad (3.34)$$

The terms p and $\boldsymbol{\tau}^f$ in this equation are pressure (Pa) and shear viscous stress (Pa), respectively [57].

The fluid momentum supply \hat{p}^f contains forces such as buoyancy which is related to average pressure and gradient of volume fraction, and a viscous drag which might be correlated to volume fractions and average velocity differences. It can be expressed as follows:

$$\hat{p}^f = K(\mathbf{v}^s - \mathbf{v}^f) + p \text{grad } n^f \quad (3.35)$$

where K is the *drag coefficient* ($\text{kg/m}^3 \text{ s}$) due to relative motion, and is defined as the ratio of viscosity of the flow μ ($\text{Pa} \cdot \text{s}$) to the permeability k (m^2) of the porous media [36, 57, 58].

$$K = \frac{\mu}{k} \quad (3.36)$$

The porous skeleton is assumed to be rigid and stationary without any deformation. Since it is not moving during the process ($\mathbf{v}^s = 0$), it is concluded from the mass balance for the solid phase (equation 3.27), that the solid's

density changes with respect to the fluid's mass supply.

$$\partial\rho^s/\partial t = \hat{\rho}^s = -\hat{\rho}^f \quad (3.37)$$

Furthermore, based on Newton's third law, the pressure and hence, the stress applied on solid is a reaction force from fluid. Therefore, the momentum exchange for the solid can be computed from the fluid momentum exchange.

$$\hat{\mathbf{s}}^s = -\hat{\mathbf{s}}^f \quad (3.38)$$

Therefore, it is possible to neglect the solid phase and it would be simpler if only the pore fluid phase (water + nickel) is considered instead of the whole 3-phase mixture (solid + water + nickel), and the effect of solid on the fluid is considered only through forces and stresses. Based on this argument, the available equations to describe the problem would be reduced to the mass and momentum balance equations for the fluid phase and its constituents, i.e. water and nickel ions.

Considering these balance equations of the fluid and the constituents, it can be noticed that there are many parameters to be determined. Therefore, to simplify the problem, it is necessary to reduce the number of needed parameters as much as possible. One way to do this is to limit the investigation to the fluid properties and define constituents' properties in terms of fluid properties.

Considering the fluid phase as the REV, the mass concentration of nickel ions can be defined as:

$$c^{\text{ni}} = \frac{\rho^{\text{ni}}}{\rho^f} \quad (3.39)$$

Equations 3.10 and 3.39 result in:

$$\rho^{\text{ni}} = c^{\text{ni}}\rho^f \quad (3.40)$$

$$\mathbf{v}^{\text{ni}} = \mathbf{v}^f + \mathbf{d}^{\text{ni}} \quad (3.41)$$

In this study, the main variable of interest is the concentration of nickel ions. So, for simplicity in the rest of this manuscript, it is illustrated by c instead of c^{ni} .

Ultimately, following the mentioned assumptions and considerations, the

equations required to describe the problem are the mass balance equations for the fluid phase and for the nickel ions, which describe the changes in the composition of the fluid phase, and the momentum balance equation for the fluid phase.

$$\rho^f \frac{\partial \mathbf{v}^f}{\partial t} + \rho^f \text{grad} \mathbf{v}^f \cdot \mathbf{v}^f = \text{div} \boldsymbol{\sigma}^f + \rho^f \mathbf{g} + \hat{\mathbf{p}}^f \quad (3.42)$$

$$\partial \rho^f / \partial t + \text{div}(\rho^f \mathbf{v}^f) = \hat{\rho}^{\text{ni}} \quad (3.43)$$

$$\partial \rho^{\text{ni}} / \partial t + \text{div}(\rho^{\text{ni}} \mathbf{v}^{\text{ni}}) = \hat{\rho}^{\text{ni}} \quad (3.44)$$

In this simplified setting, the model can be developed by knowing solely the fluid mean velocity, which can be derived from the fluid momentum balance equation. Hence, there is no benefit to investigate the momentum balance equations for the constituents, explicitly.

Derivation of Darcy's Law

The most common approach to investigate the flow through porous media is to apply Darcy's equation which can be derived as a special case of the fluid momentum balance [15]. It is generally based on the principle of a linear relation between the velocity and the pressure gradient of flow through the porous media [36]. It is assumed that the fluid is a Newtonian fluid with laminar flow through a porous medium with a rigid solid matrix. Due to the assumption of a small Reynolds number for the flow, the fluid inertia can be neglected, compared to the interaction forces of the fluid and the solid matrix. Also, the flow is assumed to be stationary and hence there is no acceleration. That means the material time derivative of fluid velocity is equal to zero. Furthermore, the viscous part of stress is negligible and the effects of viscosity are included in the momentum interaction term. Therefore, by substituting equations 3.34 and 3.35 into the equation 3.42 and applying the above-mentioned assumptions, it is concluded that:

$$0 = \text{div}(-n^f p \mathbf{I}) + \rho^f \mathbf{g} + K(-\mathbf{v}^f) + p \text{grad} n^f \quad (3.45)$$

By applying the divergence operator on equation 3.45, it results in Darcy's law [58].

$$\mathbf{v}^f = \frac{-1}{K}(n^f \text{grad} p - \rho^f \mathbf{g}) \quad (3.46)$$

Derivation of Governing Equations

In order to establish a model that accounts for the coating thickness, it is necessary to derive the equations that determine the distribution of concentration rate within the porous medium. Furthermore, due to the geometry changes during the coating process, developing a pressure and an electrical field formulation was of importance, since the concentration rate is coupled with pressure and electrical potential rates.

By substituting Darcy's equation 3.46 into the mass balance equation 3.43 of the fluid, and equations 3.40 and 3.41 into the mass balance equation 3.44 of the nickel ions, it is concluded that:

$$\frac{\partial \rho^f}{\partial t} + \text{div}\left(\frac{-\rho^f}{K}(n^f \text{grad} p - \rho^f \mathbf{g})\right) = \hat{\rho}^{\text{ni}} \quad (3.47)$$

$$\rho^f \frac{\partial c}{\partial t} + \frac{-\rho^f}{K}(n^f \text{grad} p - \rho^f \mathbf{g}) \cdot \text{grad} c = (1 - c)\hat{\rho}^{\text{ni}} - \text{div}(\rho^{\text{ni}} \mathbf{d}^{\text{ni}}) \quad (3.48)$$

Taking a glance at equations 3.47 and 3.48, it can be seen that they are in terms of the primary unknowns which are pressure p and concentration c . However, there are still three more unknowns namely, the partial density of fluid ρ^f , the production term $\hat{\rho}^{\text{ni}}$, and the diffusion velocity of ions \mathbf{d}^{ni} . That raises the need for defining three more constitutive equations in terms of the primary unknowns to reach to a closed system of equations.

The diffusive flux $\rho^{\text{ni}} \mathbf{d}^{\text{ni}}$, relative to the motion of the fluid phase, is partly due to the concentration gradient of ions in the electrolyte which introduces a diffusion term, and partly caused by the electrical field which results in a migration term. The diffusive motion can be described by *Fick's law* [14],

which alongside the migration term [59] will result in the whole flux term as:

$$\rho^{\text{ni}} \mathbf{d}^{\text{ni}} = -D \text{grad } c - \frac{z^e F}{R\theta} Dc \text{grad } \phi \quad (3.49)$$

In equation 3.49, D is the diffusion constant (kg/m s), z^e is the electric charge of the ions, F is the Faraday constant (C/mol), R is the universal gas constant (Nm/K mol), θ is the absolute temperature (K) and ϕ is the electrical potential (V).

The next step is to define a relation for the production term. Evidently, the larger the available ion concentration is, the larger the production term will be. Hence, the constitutive equation for the production term can be defined in the simplest case as:

$$\hat{\rho}^{\text{ni}} = A_1 c \quad (3.50)$$

The parameter A_1 may additionally depend on further local quantities, e.g. the electrical potential. Here, for the sake of simplicity, it will be assumed to be a constant.

The last equation is concerning the fluid density which can be defined as an equation of state of a barotropic fluid. Moreover, for the sake of simplicity, only isothermal processes are investigated. There is a direct relation between fluid density, pressure, and ion concentration. So we can define an equation based on the first terms in a Taylor series expansion of $\rho^{\text{f}}(c, p)$ as follows:

$$\rho^{\text{f}} = \rho_0 + A_2 c + A_3 (p - p_0) \quad (3.51)$$

where ρ_0 is the density of pure water and p_0 is the reference pressure. However, the fluid is assumed to be incompressible or hardly compressible. Therefore, the pressure changes should not have a profound influence and its effect should be way smaller than the effect of the concentration, resulting in $A_3 \ll A_2$.

The parameters A_1 , A_2 , and A_3 in equations 3.50 and 3.51 are unknown constants that must be identified through parameter identification.

Finally by substituting equations 3.49 - 3.51 into equations 3.47 and 3.48 the final coupled governing equation system can be obtained.

$$\begin{aligned} \frac{\partial c}{\partial t} = & \frac{1}{\rho_0 + A_2c + A_3(p - p_0)} \left[A_1c(1 - c) + D\text{div}(\text{grad}c) \right. \\ & \left. + \frac{z^eFD}{R\theta}(\text{grad}c \cdot \text{grad}\phi + c \text{div}(\text{grad}\phi)) \right] \\ & + \frac{1}{K} \left(n^f \text{grad}p - (\rho_0 + A_2c + A_3(p - p_0))\mathbf{g} \right) \cdot \text{grad}c \end{aligned} \quad (3.52)$$

$$\begin{aligned} \frac{\partial p}{\partial t} = & \frac{1}{A_3} \left[(A_1c) \left(1 - \frac{A_2}{\rho_0 + A_2c + A_3(p - p_0)}(1 - c) \right) \right. \\ & - \frac{A_2D}{\rho_0 + A_2c + A_3(p - p_0)} \left[\text{div}(\text{grad}c) + \frac{z^eF}{R\theta}(\text{grad}c \cdot \text{grad}\phi \right. \\ & \left. \left. + c \text{div}(\text{grad}\phi)) \right] + \frac{\rho_0 + A_2c + A_3(p - p_0)}{K} \left[n^f \text{div}(\text{grad}p) - \mathbf{g} \cdot (A_2\text{grad}c \right. \\ & \left. \left. + A_3\text{grad}p) \right] + \frac{A_3}{K} \left(n^f(\text{grad}p)^2 - (\rho_0 + A_2c + A_3(p - p_0))\mathbf{g} \cdot \text{grad}p \right) \right] \end{aligned} \quad (3.53)$$

Taking a glance at equations 3.52 and 3.53, one can clearly observe the contribution of different ionic transport mechanisms (diffusion, convection, migration, and sink term) to the whole electrodeposition process. However, it is still necessary to describe the electrical potential, ϕ , through the electric field, \mathbf{E} , formed by the applied external current and movement of ions. The electric field is related to the electrical potential as:

$$\mathbf{E} = -\text{grad}\phi \quad (3.54)$$

The displacement current equation describes the temporal change of the electric field according to the following equation [60, 61]:

$$\frac{\partial \mathbf{E}}{\partial t} = \frac{\mathbf{I}_{\text{ext}}}{\epsilon} - \frac{Fz^e\mathbf{J}}{\epsilon} \quad (3.55)$$

where \mathbf{I}_{ext} is the external current density (A/m²), ϵ is the absolute permittivity (C²/Nm²) and \mathbf{J} is the flux of ions (mol/m²s) which is described by

the Nernst-Planck equation.

$$\mathbf{J} = c^* \mathbf{v} - D \text{grad} c^* - \frac{z^e F}{R\theta} D c^* \text{grad} \phi \quad (3.56)$$

The term c^* in equation 3.56 is the ion concentration and has the unit mol/m³. In order to make this compatible with the definition for ion concentration in this article, c^* is replaced by the following relation in terms of c .

$$c^* = \frac{c \rho^f}{MW^{\text{ni}}} \quad (3.57)$$

where MW^{ni} is the molar weight of nickel (kg/mol).

By substituting equation 3.54 and 3.56 into equation 3.55 it is possible to calculate the rate of gradient of electric potential.

$$\frac{\partial \mathbf{E}}{\partial t} = \frac{\mathbf{I}_{\text{ext}}}{\epsilon} - \frac{F z^e}{\epsilon} \left(\frac{c \rho^f}{MW^{\text{ni}}} \mathbf{v} - \frac{D \rho^f}{MW^{\text{ni}}} \text{grad} c - \frac{z^e F \rho^f}{R\theta MW^{\text{ni}}} D c \text{grad} \phi \right) \quad (3.58)$$

This equation alongside equations 3.52 and 3.53 yields a coupled system of equations that should be solved simultaneously. With the help of this system of equations, the time derivative of concentration, pressure, and electric field within the foam can be calculated. In the considered simplified model, these data can be used to estimate the distribution of ions on the foam and finally to give an estimation of the coating thickness.

3.2.3 Back-coupling and Coating Thickness Formulation

In the previous subsection, the equations to calculate the rate of concentration, pressure, and electrical field are obtained. However, it is important to consider the changes within the foam structure during the coating process, which lead to a change in all the other parameters.

The aim in the present study is to assume the process as simple as possible so that the number of process parameters can be reduced. Therefore, the description of the geometrical properties has to be as simple as possible. In this idealization, the struts are considered as simple cylinders and the nodes between the struts are disregarded.

The concentration obtained from equation 3.52 gives information about the transported nickel ions by diffusion, convection, and migration mechanisms as well as the deducted nickel ions from the fluid phase which are coated on the foam struts. Using this concentration data, it is possible to estimate the coating thickness in each spatial point on the foam.

Moreover, with the start of the coating process, the porosity of the foam will start to change, which results in a change in permeability.

Hence, a back-coupling calculation is necessary in order to take into account the above-mentioned geometrical changes and to use the updated values to calculate the variables in the next time steps. As shown in Fig. 3.4, the foam is divided into small volume elements. It is assumed that these volume elements are so small that inside each of them, only one strut can fit. The struts can be represented by cylindrical figures. Therefore, with nickel deposition inside each volume element, the radius of these cylinders will increase.

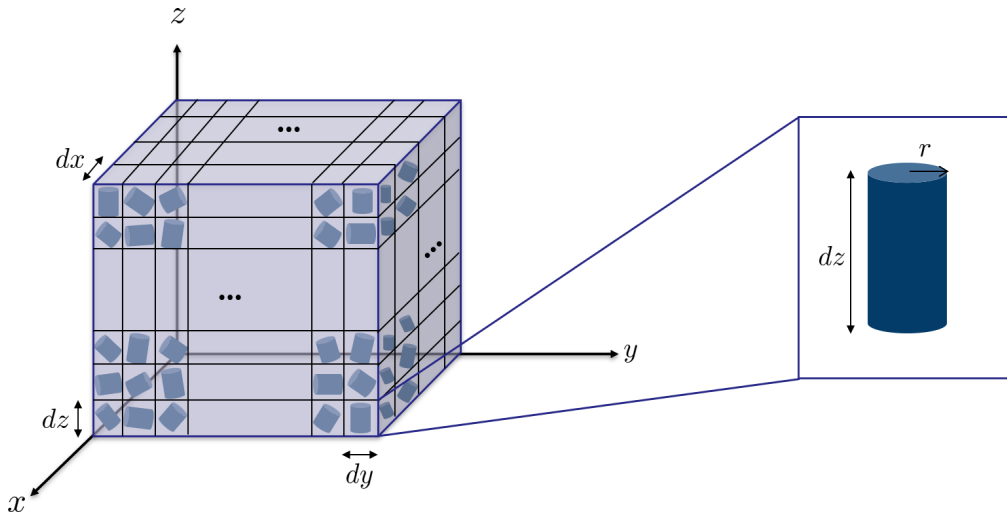


Figure 3.4: Schematic representation of struts inside each volume element.

To simplify the problem it is assumed that all the struts inside each volume element have the same size at the beginning of the coating process. Moreover, it is assumed that the initial total porosity is equal to the initial porosity of each volume element. The total volume of each volume element, dV^{el} , can

be obtained as:

$$dV^{\text{el}} = dx dy dz \quad (3.59)$$

The volume, dv^{s} , and surface, ds^{s} , of each strut inside each volume element are:

$$dv^{\text{s}} = \pi r^2(\mathbf{x}, t) dz \quad (3.60)$$

$$ds^{\text{s}} = 2\pi r(\mathbf{x}, t) dz \quad (3.61)$$

Hence, the initial radius of the struts can be calculated from the solidity,

$$n^{\text{s}} = 1 - n^{\text{f}}, \quad (3.62)$$

as:

$$n^{\text{s}}(\mathbf{x}, 1) = \frac{dv^{\text{s}}(\mathbf{x}, 1)}{dV^{\text{el}}} \quad (3.63)$$

With the start of the process, the nickel ions are coated on the surface of the strut inside the volume element. The rate of change of the coating thickness will be equivalent to the radius change. Based on Faraday's law of electrolysis [62, 63], the amount of deposition on an electrode is directly proportional to the electrical charge Q (C). This statement can be defined in terms of moles of reduced metal, M (mol) via charge, as follows:

$$M = \frac{Q}{z^e F} \quad (3.64)$$

Using the definition of molar weight of nickel (MW^{ni}), the deposition mass m (kg) can be obtained from the molar mass of deposition, as follows:

$$m = MW^{\text{ni}} M \quad (3.65)$$

Moreover, to obtain the amount of total charge being used over the deposition process, the integral of the electrical current, $I(\mathbf{x}, t)$ (A), during the

deposition time should be calculated.

$$Q = \int I(\mathbf{x}, t) dt \quad (3.66)$$

According to the definition of density, the coating thickness $\delta(\mathbf{x}, t)$ can be defined in terms of deposition mass m (kg) as:

$$\delta(\mathbf{x}, t) = \frac{m}{\rho^{\text{ni}} A} \quad (3.67)$$

where ρ^{ni} is the density of nickel and A is the area of deposition, i.e. the internal surface of the foam. Substituting equations 3.65 and 3.66 in equation 3.64, and then using the result in equation 3.67, the coating thickness at each point \mathbf{x} and each time t can be computed.

$$\delta(\mathbf{x}, t) = \frac{MW^{\text{ni}} \int I(\mathbf{x}, t) dt}{z^e F \rho^{\text{ni}} A} \quad (3.68)$$

Taking a glance at equation 3.68, it can be noticed that the local coating thickness at any time t is proportional to the integral of local electric current at that time. The Butler-Volmer equation [63–65] gives a comprehensive insight in formulation of electrode kinetics and makes it possible to calculate the local current density, I/A (A/m^2), as a function of ion concentration.

$$\frac{I(\mathbf{x}, t)}{A} = I_{\text{ext}} \left[\frac{c(\mathbf{x}, t)}{C_{\infty}} \exp\left(\frac{0.5z^e F \eta}{R\theta}\right) - \exp\left(\frac{-0.5z^e F \eta}{R\theta}\right) \right] \quad (3.69)$$

where C_{∞} is the initial reference concentration and η denotes the overpotential [59, 65, 66].

Therefore, by calculating the coating thickness, the new radius, the new solidity and therefore the new porosity can be calculated. Many practical equations are suggested in the literature for porosity-permeability relation, which have been discussed comprehensively in a review article by Hommel et al. [67]. Using these equations, e.g. exponential or power law relations, the new permeability can be obtained. The following relation has been chosen

from [67] to calculate the new permeability:

$$\frac{K}{K_0} = \left(\frac{n^f}{n_0^f} \right)^\beta \quad (3.70)$$

The exponent β in this equation is an empirical parameter [67], which depends on the local topology of the foam and has to be determined from experiments.

Hence, based on these updated values of porosity and permeability, the pressure, concentration and electrical field in the next time step will be calculated.

4

Numerical Implementation

Numerical methods play a crucial role in various fields of science, engineering, and mathematics. They provide indispensable tools for solving complex problems that are often intractable through algebraic or analytical calculations.

Modelling the electrodeposition process is a complex mathematical challenge which leads to a coupled system of non-linear equations. These equations are interconnected and influence each other's solutions. Finding the exact analytical solution to these types of problems can be very difficult or even impossible. Therefore, it is important to adopt a method which can result in an approximate reliable solution and yet be computationally efficient.

Among the various existing computational methods, the Finite Difference Method (FDM) [68–73] has shown practical and efficient performance in treating complicated equations which makes it a valuable asset in modelling and analysis of physical and mathematical problems. The ability to handle high-dimensional systems, accommodate non-linearities within a coupled system and dealing with complicated problem domains are among the many advantages of this numerical method. However, there are some challenges as well. Numerical instability, round-off errors, and the choice of appropriate algorithms are some of the issues that demand careful considerations.

Taking a glance at equations 3.52, 3.53 and 3.58, it can be easily noticed that

it is not possible to solve these equations analytically. Due to the complexity and high non-linear nature of the system choosing a proper method among the available numerical methods is greatly limited. In the present study, a finite difference method [68–71] is employed to solve the preceding coupled system of governing equations obtained in section 3.2 with predefined initial and boundary conditions. The finite difference method is a very simple and straightforward numerical approach to solve non-linear partial differential equations (PDE), which is a suitable choice for the purpose of this study. Eventually, an error analysis is performed and the convergence and stability of the solution are investigated.

4.1 Finite Difference Method (FDM)

The set of coupled non-linear PDEs 3.52, 3.53 and 3.58, consists of four main physical terms; the source/sink term, diffusion, migration and convection. An explicit approach is used to discretize these time- and space-dependent PDEs, which avoids the time-consuming, coupled treatment of the set of equations. FDM offers different discretization schemes for different problems. These schemes are derived from the Taylor series expansion of a variable $u(x)$, where $u(x)$ is differentiable up to k -th order. It can be written as a series as follows:

$$u(x + \Delta x) = u(x) + \Delta x u'(x) + \frac{\Delta x^2}{2} u''(x) + \dots + \frac{\Delta x^k}{k!} u^{(k)}(x) + \mathcal{O}(\Delta x^k) \quad (4.1)$$

where Δx is called the step size and $\mathcal{O}(\Delta x^k)$ is the approximation error term or the truncation error.

The chosen specific scheme can significantly impact the accuracy, stability, and efficiency of the numerical solution. In the following, the step by step FDM algorithm to solve the equation system of the presented model is explained.

1. Domain Discretization

The first step is to discretize the spatial and temporal domains into a grid.

$$x_i = i\Delta x \quad (4.2)$$

$$t^n = n\Delta t \quad (4.3)$$

where Δx and Δt are the space and time increments, respectively. The solution will be approximated at the discrete points (nodes) x_i at each time t^n on this grid. The chosen values for Δx and Δt have a significant influence on the performance of the scheme and on the solution. On the one hand, choosing a smaller value Δx and Δt results in a more accurate approximation. On the other hand, these values must fall within a specific range and maintain a suitable ratio to each other to ensure adherence to stability criteria. Moreover, smaller time and space increments will increase the computational time. Furthermore, a very small time increment means more iterations are required to approximate the solution, which will cause the build-up of more errors. Hence it is important to find suitable values for space- and time increments which balance stability with accuracy and computational efficiency.

2. Approximation of the Derivatives

Different FDM schemes can be obtained, from equation 4.1 for the approximation of first- and second-order derivative terms in the governing equation system. These schemes are obtained by different choices of Δx . Common schemes for the first-order spatial derivatives are

$$\text{Forward: } \frac{\partial u}{\partial x} = \frac{u_{i+1}^n - u_i^n}{\Delta x} + \mathcal{O}(\Delta x) \quad (4.4)$$

$$\text{Backward: } \frac{\partial u}{\partial x} = \frac{u_i^n - u_{i-1}^n}{\Delta x} + \mathcal{O}(\Delta x) \quad (4.5)$$

$$\text{Central: } \frac{\partial u}{\partial x} = \frac{u_{i+1}^n - u_{i-1}^n}{2\Delta x} + \mathcal{O}(\Delta x^2) \quad (4.6)$$

The common scheme to discretize the second-order derivatives is the central (symmetric) scheme.

$$\text{Central: } \frac{\partial^2 u}{\partial x^2} = \frac{u_{i+1}^n - 2u_i^n + u_{i-1}^n}{\Delta x^2} + \mathcal{O}(\Delta x^2) \quad (4.7)$$

To approximate the first- and second-order time derivatives in time-dependent problems, using the above-mentioned schemes, Δx will be substituted by Δt .

In this study, an explicit forward scheme is used for the time derivatives, and a central scheme is used for second-order spatial derivatives resulting from diffusive processes (forward in time, central in space (FTCS), see Fig. 4.1). In this scheme, the values at time t^{n+1} are calculated from the known values of previous time t^n .

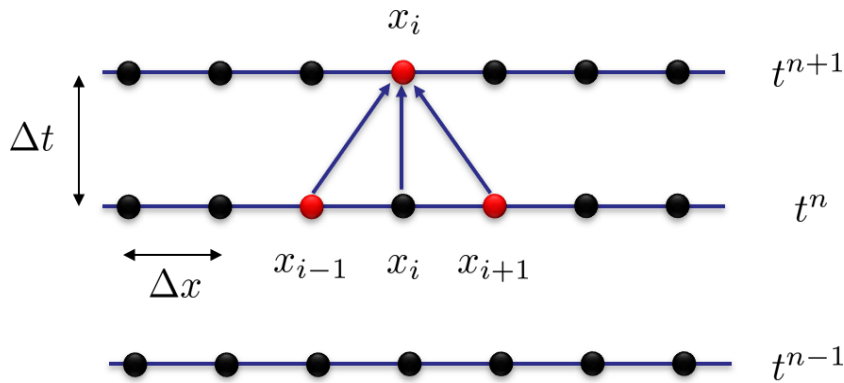


Figure 4.1: Schematic representation of the explicit forward scheme for time discretization and central scheme for space discretization in solving a 1D equation. The values at t^{n-1} and t^n are known and the values at t^{n+1} are to be calculated.

However, for solving PDEs, which describe phenomena with wave-like behaviour, these symmetric schemes are not useful anymore. In these problems, the spatial derivatives should be approximated by considering the direction of the flow or propagation of variables. Upwind schemes are designed to handle problems where the variables propagate in a specific direction, and they are particularly useful when solving convection-dominated problems. Let us consider the convection equation.

$$\frac{\partial u}{\partial t} + v \frac{\partial u}{\partial x} = 0 \quad (4.8)$$

where v is a non-zero constant velocity. The first-order upwind discretization scheme for the PDE 4.8 is:

$$\frac{u_i^{n+1} - u_i^n}{\Delta t} = \begin{cases} -v \frac{u_i^n - u_{i-1}^n}{\Delta x} & v > 0 \\ -v \frac{u_{i+1}^n - u_i^n}{\Delta x} & v < 0 \end{cases} \quad (4.9)$$

This scheme is based on the position of the upstream and implies that for a positive velocity, the information flows from left to right. In this case, a backward scheme assists to obtain the required information from the point x_{i-1} at the left side of the given point x_i . But when the velocity is negative and the flow is from right to left, it makes sense to look to the right side to know what is going to happen at the given point x_i . Fig. 4.2 represents the first-order upwind scheme for different propagation directions.

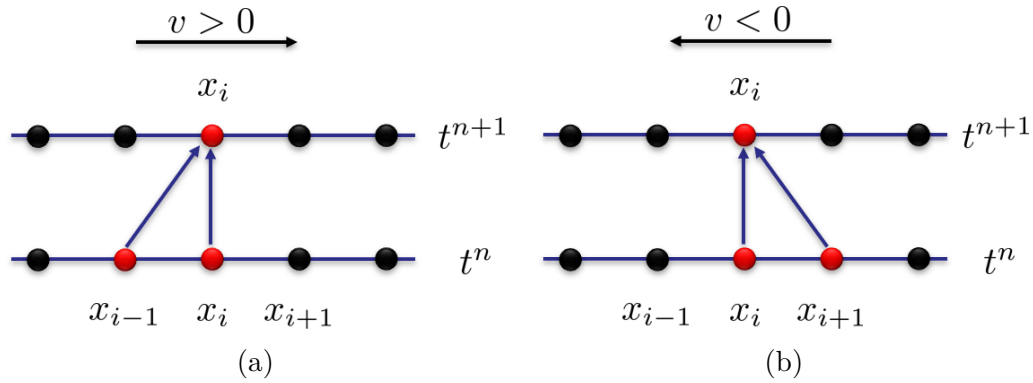


Figure 4.2: Schematic representation of first-order upwind discretization scheme for (a) $v > 0$ and (b) $v < 0$. The values at t^n are known and the values at t^{n+1} are to be calculated.

Since the convection term in equation (3.52) consists of a term specifying the direction of flow, an upwind discretization scheme is of interest here. This argument is also applicable to the migration terms in both equations because the mathematical structure of the migration term is the same as in the convective part. The resulting scheme is simple and does not require

solving a set of coupled equations. As a disadvantage though, the scheme is of limited stability. Later in this chapter, the stability and convergence of the adopted FDM schemes will be discussed in more detail.

4.1.1 Solving the System of Discrete Equations

The governing system of equations 3.52, 3.53 and 3.55 can be solved by applying the chosen discretization schemes in the previous section. For a better demonstration of the results, the concentration equation is written in terms of the main transport equations. Considering n as the time discretization index and i as the space discretization index, the 1D explicit FDM formulation of these equations can be written as follows:

$$\frac{c_i^{n+1} - c_i^n}{\Delta t} = \tag{4.10}$$

Sink: $\frac{A_1}{\rho_0 + A_2 c_i^n + A_3 (p_i^n - p_{0,i}^n)} [c_i^n (1 - c_i^n)] +$

Diffusion: $\frac{D}{\rho_0 + A_2 c_i^n + A_3 (p_i^n - p_{0,i}^n)} \left[\frac{c_{i+1}^n - 2c_i^n + c_{i-1}^n}{\Delta x^2} \right] +$

Migration: $\frac{z^e FD}{(\rho_0 + A_2 c_i^n + A_3 (p_i^n - p_{0,i}^n)) R \theta} \left[\text{grad} \phi \frac{c_{i+1}^n - c_{i-1}^n}{2\Delta x} \right. + \left. \left| \text{grad} \phi \right| \frac{c_{i+1}^n - 2c_i^n + c_{i-1}^n}{2\Delta x} + c_i^n \text{div}(\text{grad} \phi) \right] +$

Convection: $\frac{1}{K} \left(n^f \frac{p_{i+1}^n - p_{i-1}^n}{2\Delta x} - (\rho_0 + A_2 c_i^n + A_3 (p_i^n - p_{0,i}^n)) g \right) \frac{c_{i+1}^n - c_{i-1}^n}{2\Delta x} + \left| \frac{1}{K} \left(n^f \frac{p_{i+1}^n - p_{i-1}^n}{2\Delta x} - (\rho_0 + A_2 c_i^n + A_3 (p_i^n - p_{0,i}^n)) g \right) \right| \frac{c_{i+1}^n - 2c_i^n + c_{i-1}^n}{2\Delta x}$

As can be seen in equation 4.10, the spatial discretization for each term correlates to the chosen schemes explained in the previous section and depends strongly on the nature of these terms and the challenges associated with numerical stability and accuracy.

Following the same logic, the FDM formulation for the pressure and electric

field equations can be obtained as follows:

$$\begin{aligned}
\frac{p_i^{n+1} - p_i^n}{\Delta t} = & \frac{1}{A_3} \left[(A_1 c_i^n) \left(1 - \frac{A_2}{\rho_0 + A_2 c_i^n + A_3(p_i^n - p_{0_i}^n)} (1 - c_i^n) \right) \right. \\
& - \frac{A_2 D}{\rho_0 + A_2 c_i^n + A_3(p_i^n - p_{0_i}^n)} \left[\frac{c_{i+1}^n - 2c_i^n + c_{i-1}^n}{\Delta x^2} \right. \\
& + \frac{z^e F}{R\theta} (\text{grad}\phi \frac{c_{i+1}^n - c_{i-1}^n}{2\Delta x} + \left| \text{grad}\phi \right| \frac{c_{i+1}^n - 2c_i^n + c_{i-1}^n}{2\Delta x} \\
& \left. \left. + c_i^n \text{div}(\text{grad}\phi) \right) \right] + \frac{\rho_0 + A_2 c_i^n + A_3(p_i^n - p_{0_i}^n)}{K} \\
& \left[n^f \frac{p_{i+1}^n - 2p_i^n + p_{i-1}^n}{\Delta x^2} - g \left(A_2 \frac{c_i^n - c_{i-1}^n}{\Delta x} + A_3 \frac{p_i^n - p_{i-1}^n}{\Delta x} \right) \right] \\
& \left. + \frac{A_3}{K} \left(n^f \left(\frac{p_i^n - p_{i-1}^n}{\Delta x} \right)^2 - \left(\rho_0 + A_2 c_i^n + A_3(p_i^n - p_{0_i}^n) \right) g \frac{p_i^n - p_{i-1}^n}{\Delta x} \right) \right] \quad (4.11)
\end{aligned}$$

$$\frac{E_i^{n+1} - E_i^n}{\Delta t} = \frac{1}{\epsilon} (I_{\text{ext}} - F z^e \frac{J_{i+1}^n - J_i^n}{\Delta x}) \quad (4.12)$$

4.1.2 Predictor-Corrector Step: Runge-Kutta Method

In this study an explicit Runge-Kutta method [72, 74] has also been adapted which serves as an additional predictor-corrector step [68]. The idea was to modify the computations by using a weighted average of old and computed values and to obtain a method with better convergence characteristics.

The predictor-corrector approach is a two-step process that combines a predictor step and a corrector step. It's commonly used in time-dependent problems where iterative refinement of the solution is desired in order to achieve accurate results. In the predictor step, based on the current state of the solution and the governing equations, an initial estimate of the solution at the next time or spatial step is computed. This step is often simpler and faster but may introduce some errors. Then this predicted solution is used as an intermediate solution, and additional correction terms are calculated. These correction terms are typically based on the residual errors introduced

in the predictor step. The corrector step aims to refine the solution and improve accuracy.

Let us consider the differential equation as:

$$\frac{\partial u}{\partial t} = F(u, t) \quad (4.13)$$

The general k -stage Runge–Kutta method (RK(k)) can be written as:

$$u^{n+1} = u^n + \Delta t \sum_{i=1}^k b_i f_i \quad (4.14)$$

where:

$$f_i = F(t^n + c_i \Delta t, u^n + \Delta t \sum_{j=1}^k a_{ij} f_j) \quad (4.15)$$

The coefficients a_{ij} are the arrays of the matrix A which indicates the dependence of the stage on the derivatives found at other stages. The vector b are the weights and the vector c indicates the positions, within the step, of the evaluated functions. These coefficients are chosen from the arrays in the Butcher tableau [74] which for a k -stage Runge-Kutta method is of the general form:

$$\begin{array}{c|c} c & A \\ \hline & b^T \end{array}$$

By choosing the following arrays, the second-order Runge-Kutta method (RK(2)) is obtained.

$$\begin{array}{c|cc} 0 & 0 & 0 \\ 1 & 1 & 0 \\ \hline & 1/2 & 1/2 \end{array}$$

This scheme is also called Heun's scheme which is second-order accurate and it is conditionally stable [68]. The method involves two function evaluations per time step and computes an intermediate estimate using Euler's method.

The final estimate is then computed using a weighted average of the initial and intermediate estimates. The intermediate estimation of the solution can be served as the predictor step which will yield an initial solution as follows:

$$\tilde{u}^{n+1} = u^n + \Delta t F(u^n, t^n) \quad (4.16)$$

Then, the update formula for Heun's method serves as the corrector step and uses the intermediate estimate for the solution in the previous step and improves it further.

$$u^{n+1} = u^n + \frac{\Delta t}{2} [F(\tilde{u}^{n+1}, t^{n+1}) + F(u^n, t^n)] \quad (4.17)$$

4.1.3 Convergence, Stability, and Consistency

The performance of a numerical method should be evaluated based on the *convergence*, *stability* and *consistency* of the solutions [75]. These criteria serve as essential benchmarks in ensuring the accuracy, reliability, and robustness of the method, which ultimately results in the most efficient and suitable choice of numerical scheme. However, these concepts have been developed only for special cases. In the case of the complex non-linear coupled PDEs defined in this study, seeking assistance from the theory in combination with performing numerical experimentation is the only approach to proceed. In the following, these concepts are discussed in more detail [75, 76].

Convergence

In numerical simulations, the aim is for the solution of the finite difference equations to converge to the solution of the corresponding partial differential equation. In all the grid-based numerical schemes the accuracy of the numerical results depends on the computational grid size. The goal is to achieve to a grid-converged solution, i.e. a solution that does not change significantly when more grid points are employed.

Convergence study is a typical way to anticipate the sensibility of the numerical solution. This is done by comparing the results obtained from successive iterations of mesh refinements. Assuming \mathbf{u} to be the exact solution vector

and \mathbf{u}^h is the numerical solution vector for a mesh size h . Then the error can be defined as [75]:

$$E = \|\mathbf{u} - \mathbf{u}^h\|_2 \quad (4.18)$$

In this equation, $\|\bullet\|$ is the Euclidean norm and defined as:

$$\|\mathbf{u}\|_2 = \sqrt{\sum_{i=1}^N |u_i|^2} \quad (4.19)$$

A finite difference method is called convergent if the error E tends to zero as the mesh size tends to zero. In the present study, due to the lack of an exact solution, u is obtained by an extremely fine mesh size.

Based on the Lax Theorem, an FDM scheme for solving a linear PDE can be proved to be convergent if it is both consistent and stable [75, 76]. Although this theory can not be directly applied to non-linear PDEs, the study of consistency and stability gives valid information and contributes to finding a convergent scheme [72]. Thus in the following these concepts are investigated.

Stability and Consistency

A consistent FD scheme is obtained when the truncation error tends to zero as the mesh size tends to zero. That means that a consistent scheme should provide a good approximation to the PDE when the mesh is sufficiently fine. However, a consistent scheme does not necessarily yield an accurate numerical solution to the PDE. By a Taylor expansion of the relevant functions, the consistency of the FDM schemes that have been used in this study is guaranteed. The major issue is to find the stability criteria.

A finite difference scheme is called stable if the errors remain bounded with time. The FDM scheme used to solve this system of PDEs is an explicit scheme. The stability of explicit schemes is highly restricted by the maximum allowable time step. To find the maximum allowable time step it is needed to perform a stability analysis. However, the stability analyses have been developed only for simple and special cases. To find the maximum stable time step for complex PDEs without analytical solutions, a combination of theoretical concepts and heuristic calculations is needed.

For explicit finite difference methods, the stability criteria derived from the

von Neumann analysis depends on the specific PDE being solved and the discretization scheme being used. In the case of the convection equation 4.8 the von Neumann stability criterion can be expressed in terms of the Courant–Friedrichs–Lewy (CFL) number [75] which is defined as:

$$\text{CFL} = \frac{v\Delta t}{\Delta x} \quad (4.20)$$

For the explicit finite difference scheme applied to the convection equation the stability criterion is typically:

$$|\text{CFL}| \leq 1 \quad (4.21)$$

If the CFL number exceeds this critical value, the numerical solution is likely to be unstable, leading to oscillations or nonphysical behaviour.

For diffusion-dominated problems, the stability considerations are generally controlled by the diffusion coefficient D . The stability of explicit finite difference schemes for diffusion problems is generally defined as [75]:

$$\frac{D\Delta t}{(\Delta x)^2} \leq \frac{1}{2} \quad (4.22)$$

The available stability criteria for simple problems can be used as a general guideline to reach stability in solving the more complicated PDEs. It should also be borne in mind that these criteria are just necessary conditions for stability and hence convergence, and not sufficient [75]. Therefore, some numerical experiments and parameter tuning are needed to achieve the desired outcome.

4.2 Transformation to Normalized Form

The derived coupled equation system involves numerous parameters and the discretization of this PDE system can be very sensitive to the range of these parameters. This phenomenon becomes even more evident when the parameters come from orders of magnitude that are vastly different from each other. Normalization offers the advantage of scaling the variables to a common scale,

often between 0 and 1, regardless of their physical dimensions. The aim is to bring variables onto a comparable scale to improve the numerical stability and convergence in algorithms and facilitate the interpretation of the results. The process typically involves mapping the variable values to a specific range (e.g., $[0, 1]$). To normalize time $t \in [0, T]$ and space $x \in [0, L]$ variables in the equation system 3.52, 3.53 and 3.58, the following normalized parameters are defined:

$$t^* = \frac{t}{T} \quad (4.23)$$

$$x^* = \frac{x}{L} \quad (4.24)$$

Then:

$$\frac{\partial}{\partial t^*} = T \frac{\partial}{\partial t} \quad (4.25)$$

$$\frac{\partial}{\partial x^*} = L \frac{\partial}{\partial x} \quad (4.26)$$

$$\frac{\partial^2}{\partial x^{*2}} = L^2 \frac{\partial^2}{\partial x^2} \quad (4.27)$$

Using the above definitions, the number representing the domain length and the total process time is 1.

5

Results and Discussion

In this chapter, the performance of the proposed method is examined. Different problems with different conditions will be considered to show the many potentials of the model to investigate and simulate the electrodeposition process from different aspects.

In the first section, by breaking down the concentration equation into the generally known equations, the performance of the solution algorithm and accuracy of the developed FDM code are validated. This code is developed in MATLAB[®]. After making sure that the code yields reliable results, a simplified model for a one-dimensional domain is considered in the second section. The general conditions of the experiment and the magnitudes of physical parameters are specified. In this section, the one- and double-sided material models are solved and the influence of different parameters is studied. Moreover, the performance of the numerical method is examined by doing a convergence study. In the third section, using the proposed model, the Ni/PU coating process is simulated on a two-dimensional domain and the numerical results are compared and validated with the experimental results.

5.1 Validation of the Developed FDM Code

Before solving the coupled problem of the full deposition process, it is necessary to validate the calculations performed by the developed code and check the correctness of the results.

The proposed model consists of three coupled non-linear equations. Due to the complexity of these equations, there is no available analytical solution. Therefore, they need to be handled according to the general classifications of PDEs with existing analytical solutions.

To do so, the concentration equation 3.52 is considered and constant values are assumed for pressure and electrical potential. Equation 3.52 consists of four terms, each representing different transport mechanisms which can be reformulated as follows:

$$\text{Sink term: } \quad \frac{\partial c}{\partial t} = \frac{A_1}{\rho^f} [c(1 - c)] \quad (5.1)$$

$$\text{Diffusion term: } \quad \frac{\partial c}{\partial t} = \frac{D}{\rho^f} [\text{div}(\text{grad}c)] \quad (5.2)$$

$$\text{Migration term: } \quad \frac{\partial c}{\partial t} = \frac{z^e F D}{\rho^f R \theta} [\text{grad}c \cdot \text{grad}\phi + c \text{div}(\text{grad}\phi)] \quad (5.3)$$

$$\text{Convection term: } \quad \frac{\partial c}{\partial t} = \frac{1}{K} (n^f \text{grad}p - \rho^f \mathbf{g}) \cdot \text{grad}c \quad (5.4)$$

The above-mentioned coefficients in front of each term can be substituted by a single representative coefficient:

$$\lambda_S = \frac{A_1}{\rho^f} \quad (5.5)$$

$$\lambda_D = \frac{D}{\rho^f} \quad (5.6)$$

$$\lambda_M = \frac{z^e F D}{\rho^f R \theta} \quad (5.7)$$

$$\lambda_C = \frac{1}{K} \quad (5.8)$$

The pressure is assumed to have a constant linear distribution in the spatial direction z for all time steps, as:

$$p(z, t) = (p_{max} - p_0) \frac{N - z}{N} \quad (5.9)$$

where N is the total number of spatial nodes and z is the spatial coordinate corresponding to each node. Moreover, the electric field is considered as:

$$\frac{d\mathbf{E}}{dt} = \frac{\mathbf{I}_{ext}}{\epsilon} \quad (5.10)$$

In the following, different benchmark tests corresponding to each elementary process are presented. By considering all the coefficients equal to zero except for one, each process can be easily considered one at a time and be compared with its corresponding analytical solution.

5.1.1 Reaction: Sink

In the present study, the reaction term is a sink-type since electrodeposition leads to the reduction of ion concentration. Considering the reaction equation:

$$\frac{\partial c}{\partial t} = \lambda_S [c(1 - c)] \quad (5.11)$$

It can be noticed that there is no spatial derivative in this PDE. Hence, the variable magnitude changes only in time and not in space direction. To obtain the analytical solution, we can separate variables and then integrate them. Solving for c results in:

$$c(z, t) = \frac{Be^{\lambda_S t}}{1 + Be^{\lambda_S t}} \quad (5.12)$$

where B is a constant which can be specified by the initial condition value.

Let us assume the following conditions:

$$0 \leq t \leq 1; \quad \Delta t = 10^{-2} \quad (5.13)$$

$$0 \leq z \leq 1; \quad \Delta z = 10^{-1} \quad (5.14)$$

$$\text{Initial Condition: } c(z, 0) = f(z) = C_\infty \quad (5.15)$$

The numerical and analytical transient results with 11 spatial grid points and $\lambda_S = -2$ and $C_\infty = 10^{-1}$ are compared and shown in Fig. 5.1. The analytical solution is shown with red lines, while the blue asterisks belong to the numerical results. As can be seen, the results overlapped completely.

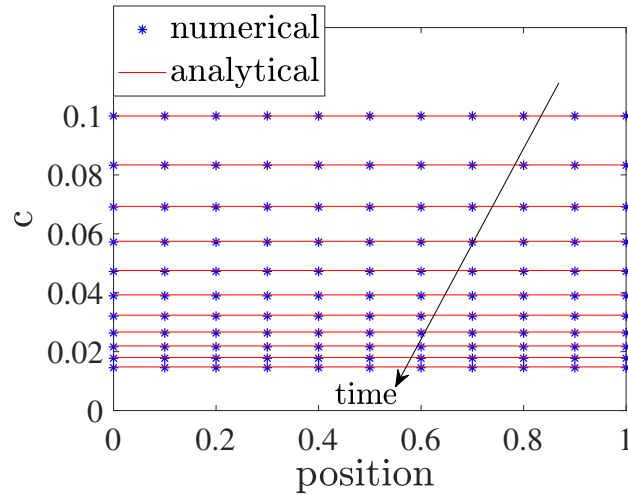


Figure 5.1: The comparison of numerical and analytical solution of reaction equation.

5.1.2 Diffusion

Diffusion is a transport mechanism which is realized due to random molecular motions from a lower to higher concentration area. Diffusion equation, also known as heat conduction equation, is a mathematical equation derived by Fourier [77, 78]. Therefore, the analytical solution to the diffusion equation

is based on the Fourier transform series.

Let us consider the diffusion equation on a 1D domain $\Omega = [0, L]$ as:

$$\frac{\partial c}{\partial t} = \lambda_D [\text{div}(\text{grad}c)] \quad (5.16)$$

The general analytical solution to this equation is:

$$c(z, t) = \sum_{m=1}^{\infty} B_m \exp\left(-\left(\frac{m\pi}{L}\right)^2 \lambda_D t\right) \sin \frac{m\pi}{L} z \quad (5.17)$$

where:

$$B_m = \frac{2}{L} \int_0^L f(z) \sin \frac{m\pi}{L} z dz \quad (5.18)$$

The term $f(z)$ is the initial condition data. To specify the analytical solution, it is necessary to specify the initial and boundary conditions. The following initial and Dirichlet boundary conditions are assumed:

$$c(z, 0) = f(z) = C_{\infty} \quad (5.19)$$

$$c(0, t) = c(L, t) = 0 \quad (5.20)$$

Using the initial and boundary conditions defined in equations 5.19 and 5.20 the analytical solution can be written as:

$$c(z, t) = \sum_{m=1}^{\infty} \frac{4C_{\infty}}{(2m-1)\pi} \exp\left(-\left(\frac{(2m-1)^2 \lambda_D \pi^2 t}{L^2}\right)\right) \sin \frac{(2m-1)\pi z}{L} \quad (5.21)$$

Assuming $\lambda_D = 10^{-2}$, the time and spatial steps must be chosen in a way to satisfy the stability criteria in equation 4.22. The numerical and analytical responses for the following time and space conditions and $C_{\infty} = 10^{-1}$ are presented in Fig. 5.2.

$$0 \leq t \leq 1; \quad \Delta t_1 = 10^{-2} \quad (5.22)$$

$$0 \leq z \leq 1; \quad \Delta z_1 = 10^{-1} \quad (5.23)$$

The qualitative comparison of the two graphs shows a very good agreement between the results.

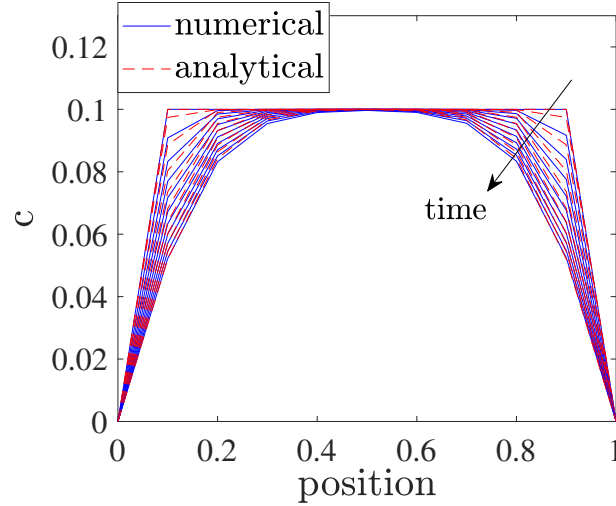


Figure 5.2: The comparison of numerical and analytical solution of diffusion equation. The analytical solution is based on Fourier transform series.

To investigate the influence of time and spatial step size, the problem is solved again by considering a smaller time step and a smaller space grid (equations 5.24 and 5.25). Therefore, taking into account the stability criteria of equation 4.22, the following values are considered:

$$\Delta t_2 = 10^{-3}; \quad \Delta z_2 = 10^{-1} \quad (5.24)$$

$$\Delta t_3 = 10^{-3}; \quad \Delta z_3 = 10^{-2} \quad (5.25)$$

The results for these two sets of parameters are shown in Fig. 5.3. By a qualitative comparison of the results, it seems that increasing the time step size does not improve the results significantly (Fig. 5.2 vs. Fig. 5.3 (a)). However, by increasing the element number, the precision of the calculations increases as well and the results overlap even better (Fig. 5.3 (a) vs. Fig. 5.3 (b)).

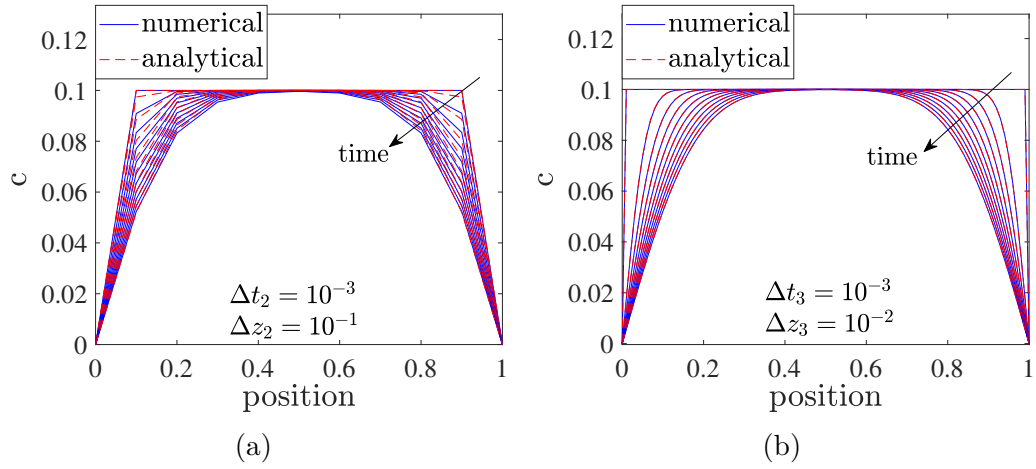


Figure 5.3: The comparison of numerical and analytical solution of diffusion equation with (a) smaller time step size ($\Delta t_2 = 10^{-3}$) and (b) smaller space grid size ($\Delta z = 10^{-2}$).

To investigate the influence of the size of time and space discretization in more detail, the error E according to equation 4.18 is calculated for different sets of discretization parameters. Fig. 5.4 illustrates the calculated errors for four different spatial mesh sizes $\Delta z = \{10^{-1}, 5 \times 10^{-2}, 10^{-2}, 5 \times 10^{-3}\}$ with three time step sizes $\Delta t = \{10^{-3}, 10^{-4}, 10^{-5}\}$.

The dominant influence of spatial size over time step size is evident in this graph. While for all the time step sizes, the results show almost the same behaviour, the error decreases with the decrease of spatial mesh. This can be due to the nature of the diffusion equation, where the FDM central scheme used for the second-order spatial derivative is second-order accurate ($\mathcal{O}(\Delta x^2)$) and the error decreases quadratically with the spatial step size.

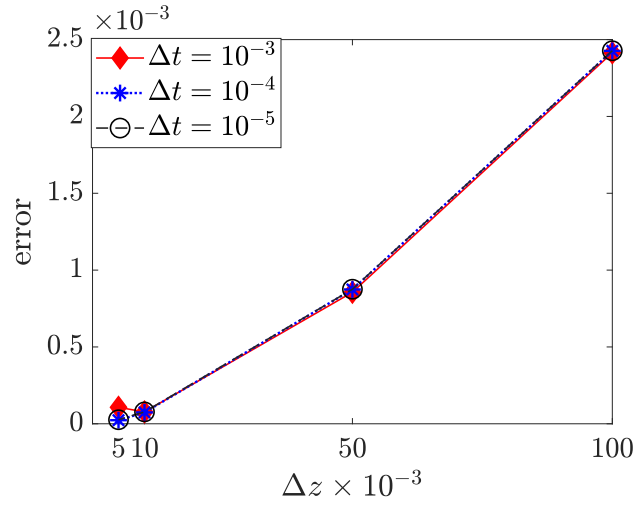


Figure 5.4: The comparison of error between numerical and analytical solutions of diffusion equation, for the different sets of time and spatial discretizations.

Choosing smaller discretization steps in general leads to more precise results. However, it's crucial to establish a reasonable limit. Excessive reduction may result in either high unnecessary computational costs or even unstable answers.

5.1.3 Convection and Migration

The convection equation, also known as the advection equation, describes the forced transport of a quantity due to the average velocity of the bulk fluid motion. The typical analytical solution to the convection equation represents a wave moving in the direction of the velocity.

In this section, for the sake of simplicity, constant functions for pressure and electrical potential distribution according to equations 5.9 and 5.10 have been assumed. Equation 5.10 results in:

$$\mathbf{E} = -\text{grad}\phi = \frac{\mathbf{I}_{\text{ext}}}{\epsilon} t \quad (5.26)$$

$$\operatorname{div}\mathbf{E} = -\operatorname{div}(\operatorname{grad}\phi) = \frac{\mathbf{I}_{\text{ext}}}{\epsilon} \quad (5.27)$$

With this in mind, by comparing the migration and convection equations 5.3 and 5.4, it can be seen that they have a similar mathematical format. However, due to the additional term in migration equation, finding an analytical solution to this equation is not possible. Therefore, in this section, only the convection equation is considered and validated. However, due to its similarity with convection equation, the same numerical approach has been utilized to solve the migration equation.

Let us write the convection equation 5.4 as follows:

$$\frac{\partial c}{\partial t} + v \operatorname{grad} c = 0 \quad (5.28)$$

where

$$v = -\lambda_C (n^f \operatorname{grad} p - \rho^f \mathbf{g}) \quad (5.29)$$

A smooth initial condition consisting of a hill-shaped profile and a periodic boundary condition are assumed.

$$c(z, 0) = f(z) = \begin{cases} \exp(-100(z - 0.2)^2) & 0 \leq z \leq L \\ 0 & \text{otherwise} \end{cases} \quad (5.30)$$

$$c(0, t) = c(L, t) \quad (5.31)$$

The problem is solved for the following choice of parameters:

$$\begin{aligned} \lambda_C &= 10^{-4} \\ n^f &= 0.9 \\ \rho^f &= 1000 \\ g &= 9.81 \\ p_{max} &= 100; \quad p_0 = 0 \end{aligned}$$

Considering the CFL stability condition for convection (equation 4.21), the

problem conditions can be written as follows:

$$0 \leq t \leq 1; \quad \Delta t = 10^{-3} \quad (5.32)$$

$$0 \leq z \leq 1; \quad \Delta z = 10^{-2} \quad (5.33)$$

The analytical solution to equation 5.28 is:

$$c(z, t) = f(z - vt) = \begin{cases} \exp(-100(z - vt - 0.2)^2) & 0 \leq z - vt \leq L \\ 0 & \text{otherwise} \end{cases} \quad (5.34)$$

The analytical and numerical responses are illustrated in Fig. 5.5. As can be seen in Fig. 5.5, while the hill travels to the right with constant velocity, in the numerical approximation the height of the hill profile decreases with time and the solution experiences damping. This behaviour is often associated with numerical dispersion, which is an inherent characteristic of certain FDM schemes. To have a better comparison the results are shown in Fig. 5.6 for four different time steps.

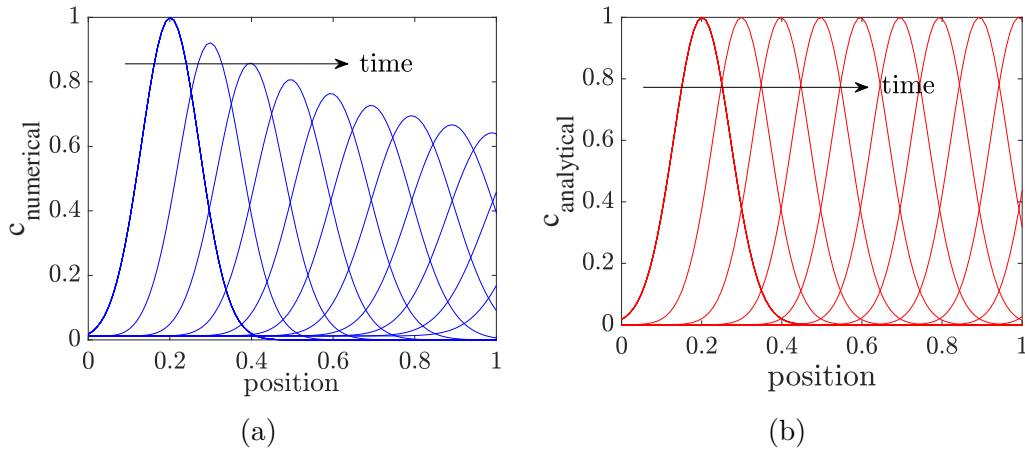


Figure 5.5: The qualitative comparison of (a) numerical and (b) analytical solution of convection equation for $\Delta t = 10^{-3}$ and $\Delta z = 10^{-2}$.

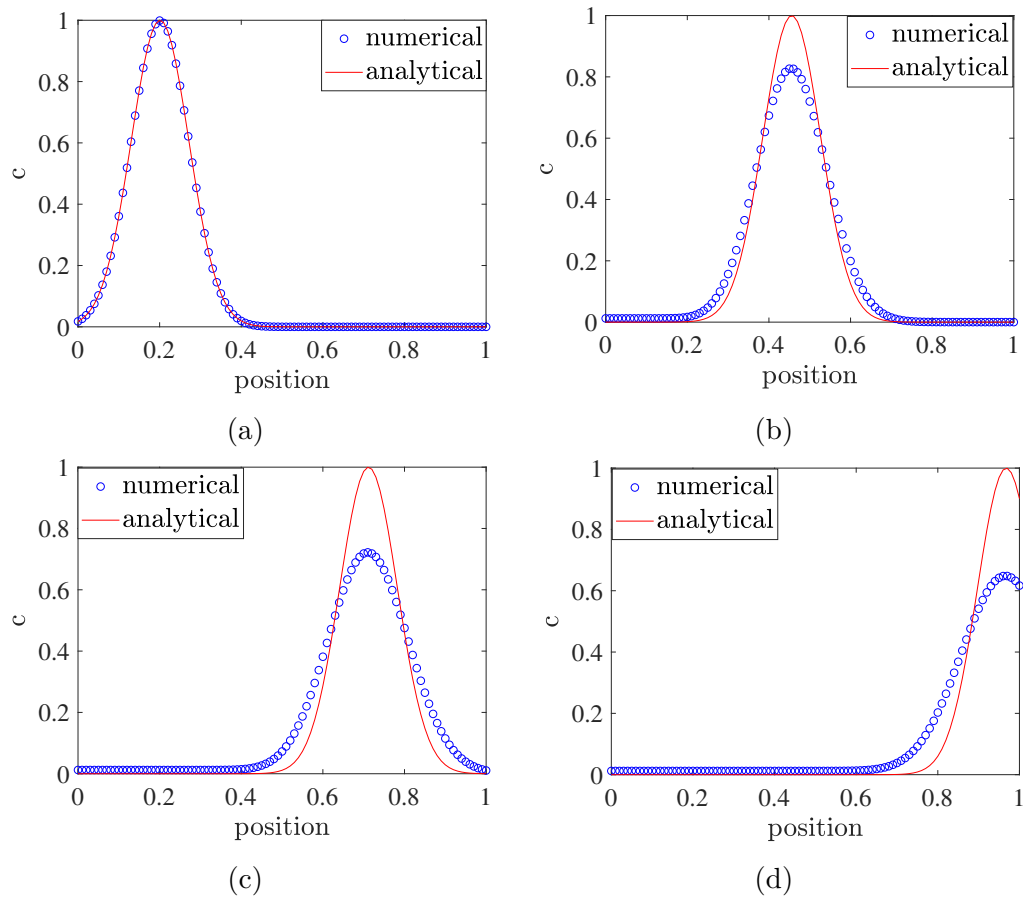


Figure 5.6: The quantitative comparison of numerical and analytical solution of convection equation with $\Delta t = 10^{-3}$ and $\Delta z = 10^{-2}$ at (a) $t = 0$, (b) $t = 0.25$, (c) $t = 0.5$ and (d) $t = 0.75$.

Many FDM schemes, particularly first-order schemes like the upwind scheme, can introduce numerical dispersion. As a result, over time, the solution may become smeared or spread out, leading to the appearance of the hill getting smaller. The first-order upwind scheme can be reinterpreted as the second-order central difference scheme plus an artificial diffusion term which is responsible for the damping. According to the von Neumann stability analysis and the CFL condition of equation 4.21, the upwind scheme is conditionally stable. To guarantee stability, the physical velocity v should be equal to or smaller than the numerical method's spreading velocity $\Delta x/\Delta t$. By choosing a smaller grid size, the difference between

these two velocities reduces and this effect will disappear [72].

The problem is solved another time with $\Delta t = 10^{-3}$ and $\Delta z = 10^{-3}$. The results are shown in Fig. 5.7. As can be seen in these graphs, the numerical dissipation has been omitted by making the spatial discretization smaller.

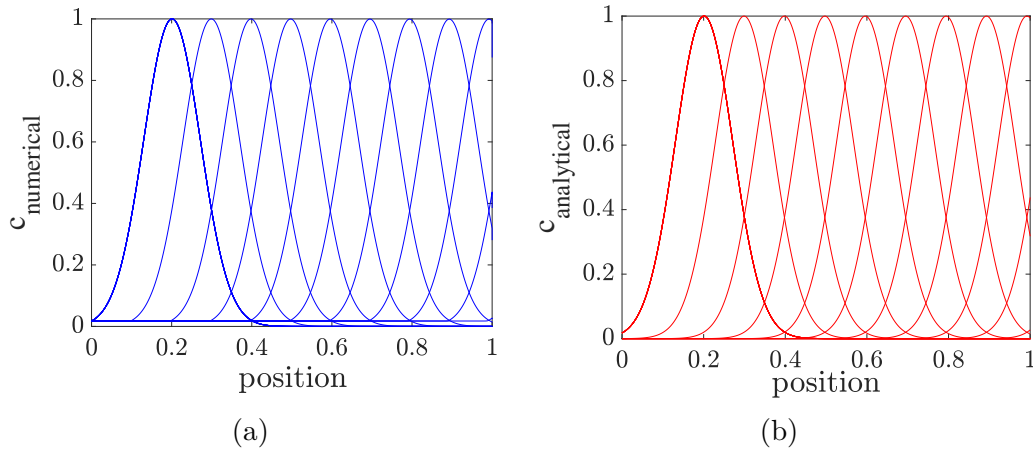


Figure 5.7: The comparison of numerical and analytical solution of convection equation for $\Delta t = 10^{-3}$ and $\Delta z = 10^{-3}$.

The purpose of the previous investigations is to validate the performance of the adopted FDM schemes and identify the role that each parameter plays in reaching accurate numerical results. These results can confirm the accuracy of the developed code and the reliability of the solutions.

However, the full set of governing equations involves multiple parameters and the values of these parameters significantly influence the outcome. Therefore, solving the full set of equations is a challenging task due to the high sensitivity of the equations to parameter values. The focus of the next section is to discuss the parameter tuning to obtain the desired results. Additionally, various potentials of the proposed model are discussed.

5.2 Implementing the Model on a One-Dimensional Domain

In this section, the solution to the complete sets of coupled equations is obtained using the adopted FDM scheme and parameter tuning. A hypothetical problem has been defined to investigate the performance of the proposed model. For the sake of simplicity and an efficient interpretation of results, normalized values are defined for the time and space domains. Therefore, the model is validated on a computational domain with a length of 1, as shown in Fig. 5.8. Moreover, the electric field due to the movement of ions is neglected and it is assumed that it is only formed by the applied external current (see equations 5.26 and 5.27). Based on the 1D assumption, the problem is only solved in the flow direction in the mid-plane of the cylindrical specimen.

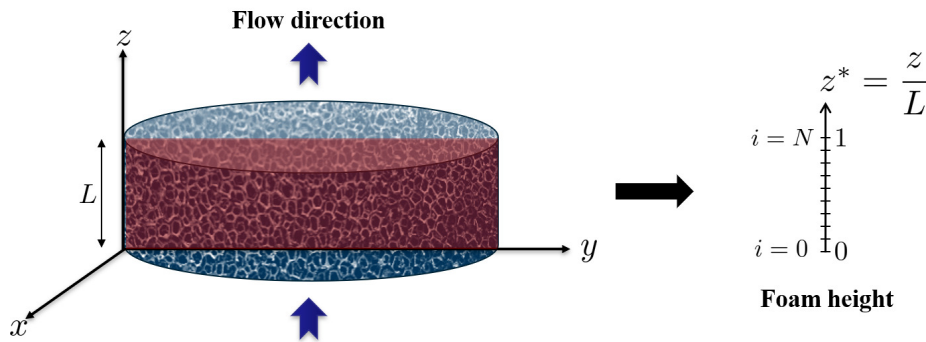


Figure 5.8: Problem domain with the direction of flow against gravity.

A general overview of the experiment has been given in section 2.2.1. The purpose of this section is to illustrate the performance of the solution scheme and various potentials of the proposed model. Hence, the corresponding initial and boundary conditions are defined in such a way to represent the experiment's conditions in [8] and yet be as simple as possible.

In the following, the normalized parameters are shown simply without an

asterisk. Therefore:

$$0 \leq t \leq 1; \quad \Delta t = 10^{-2} \quad (5.35)$$

$$0 \leq z \leq 1; \quad \Delta z = 10^{-3} \quad (5.36)$$

It is assumed that the process is performed under a constant temperature of 50°C, with an external current density of 16.5 A/m² for 108.5 h. The height of the PU foam specimen is 40 mm with 90 percent porosity [8]. The magnitudes of different physical constants in equations 3.52, 3.53 and 3.55 and the back-coupling parameters are listed in Table 5.1.

Table 5.1: Magnitudes of problem's physical constants

| Constant | Value | Constant | Value |
|------------|---------------------------------------|------------------|------------------------------|
| ρ_0 | 1000 kg/m ³ | D | 6.8×10^{-10} kg/m s |
| z | 2 | F | 96485.33 C/mol |
| R | 8.31 Nm/K mol | θ | 323 K |
| ϵ | 70 C ² /Nm ² | I_{ext} | 16.5 A/m ² |
| K | 1.3×10^5 kg/m ³ s | n^f | 0.9 |
| MW^{ni} | 5.87×10^{-2} kg/mol | g_z | 9.8 m/s ² |
| β | 8 | η | 0.2 V |

The diffusion coefficient D is assumed to be equal to the ionic diffusion coefficient of Ni^{2+} in free water [79]. The drag coefficient K is computed based on equation 3.36 and according to the magnitudes of foam permeability and electrolyte viscosity provided by the experiment [8]. Moreover, the exponent β is an empirical parameter and chosen based on the data found in [67]. For the sake of simplicity, the over-potential η is assumed to be constant during the process and its value is chosen based on the Tafel diagram corresponding to the initial reference condition [80].

It is assumed that at the beginning of the process, the pump is off, and also

no electrical current is applied to the system. Keeping this in mind alongside the assumption of an infinite ion reservoir, the initial conditions are defined as follows:

$$c(z, 0) = C_\infty \quad (5.37)$$

$$p(z, 0) = p_0 \quad (5.38)$$

$$E(z, 0) = E_0 \quad (5.39)$$

When the pump is turned on, it is assumed that it takes a time t_1 to reach the designated pressure p_{max} at the inlet. Moreover, the applied external electric current alongside the infinite ion reservoir results in the definition of the following boundary conditions at the inlet of the foam:

$$c(0, t) = C_\infty \quad (5.40)$$

$$p(0, t) = \begin{cases} \frac{p_{max} (t - 1)}{t_1} & t \leq t_1 \\ p_{max} & t > t_1 \end{cases} \quad (5.41)$$

$$E(0, t) = E_1 \quad (5.42)$$

On the outlet of the foam, the ion concentration is influenced both by the flow of electrolyte (the pump), and the the upper anode (see Fig. 2.1). Hence, a Robin boundary condition can be a suitable choice to describe the convection and diffusion effects. Moreover, the pressure reaches the constant outlet pressure p_0 . Hence, the boundary conditions at the outlet are defined as:

$$a c(1, t) + (1 - a) \frac{\partial c(1, t)}{\partial z} = a C_\infty \quad (5.43)$$

$$p(1, t) = p_0 \quad (5.44)$$

$$E(1, t) = E_1 \quad (5.45)$$

The coefficient a in equation 5.43 is the parameter determining the ratio of convection and diffusion influence.

Using the above-mentioned magnitudes and considering the corresponding initial and boundary conditions, the concentration, pressure, and electrical field distributions can be calculated by solving the equation system 3.52, 3.53, and 3.55. By doing a heuristic parameter tuning, the limit of the input parameters A_1 , A_2 and A_3 and the sensitivity of the responses to their magnitudes are determined. Moreover, by changing the corresponding coefficients in equations 5.5 - 5.8, the influence of each process can be easily investigated. In the following, different examples are discussed and the model is explored from different aspects. In these examples, only the results at the last time step are illustrated.

5.2.1 Influence of Input Parameters

The magnitudes of the input parameters A_1 , A_2 and A_3 are determined by numerical experimentation while taking into account the definitions of the constitutive equations. By considering constant values for other parameters and changing the value of one parameter at a time, the limits and effects of each parameter are investigated.

According to the defined equation 3.50 for the production term, A_1 is a sink constant and therefore must be negative. Moreover, the value of A_1 has a direct influence on the concentration value. Higher magnitudes of A_1 results in more distribution of ion concentration, as shown in Fig. 5.9. Hence, this parameter should be tuned based on the measured data from the experiments.

The constants A_2 and A_3 are mostly influential on the pressure responses, since the pressure formulation 3.53 developed from the constitutive equation 3.51.

Based on equation 3.51 and the incompressibility assumption, the effect of pressure change on the electrolyte density is negligible compared to the concentration change. Hence, the pressure constant A_3 must be much smaller than the concentration constant A_2 . However, taking a glance at equation 3.53 there should be a limit for A_3 as the equation is divided by A_3 and it can lead to numerical instabilities.

Fig. 5.10 shows the influence of different choices of A_2 . From a physical

point of view, the pressure should neither be negative nor exceed the maximum pump pressure. Therefore, the values of $A_2 = 1000$ or $A_2 = 5000$ can not be an appropriate choice of numbers. Moreover, the value of A_2 should be chosen in a way to guarantee a semi-linear behaviour for the pressure distribution between the inlet and outlet of the foam. Hence, the value of $A_2 = 1500$ seems to be a suitable choice.

Meanwhile, the parameter A_3 not only should result in physically meaningful pressure distribution but also should be set in a way to avoid numerical instabilities. On the one hand, very small values of A_3 in the denominator results in a highly ill-conditioned numerical problem, which will increase the sensitivity to numerical errors and amplification of fluctuations. This phenomenon is characterized by a gradual escalation of numerical instabilities, ultimately leading to divergence in the solution. On the other hand, this value should be small enough not to contradict the fluid density definition of equation 3.51.

The lower limit for A_3 is equal to 2×10^{-1} . Lower values than this result in instabilities and divergent solutions. Fig. 5.11 depicts the influence of A_3 parameter on the pressure responses. Larger values of A_3 lead to faster changes of the pressure and hence, higher pressure gradients. This parameter can be tuned according to the fluid velocity data from the experiment.

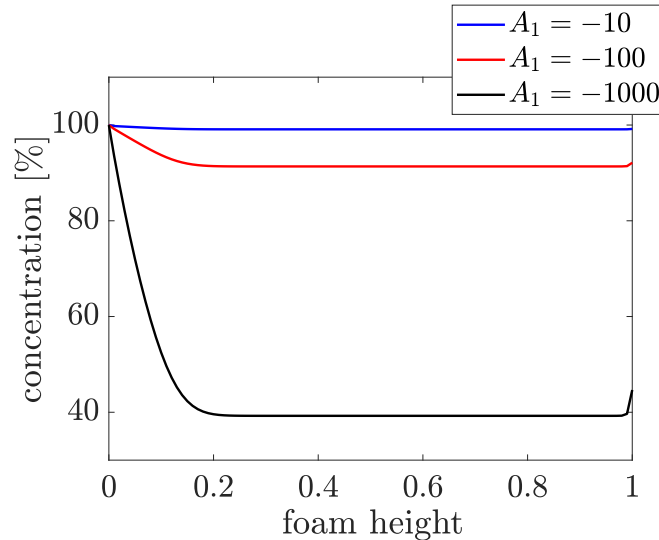


Figure 5.9: The influence of A_1 values on the concentration response.

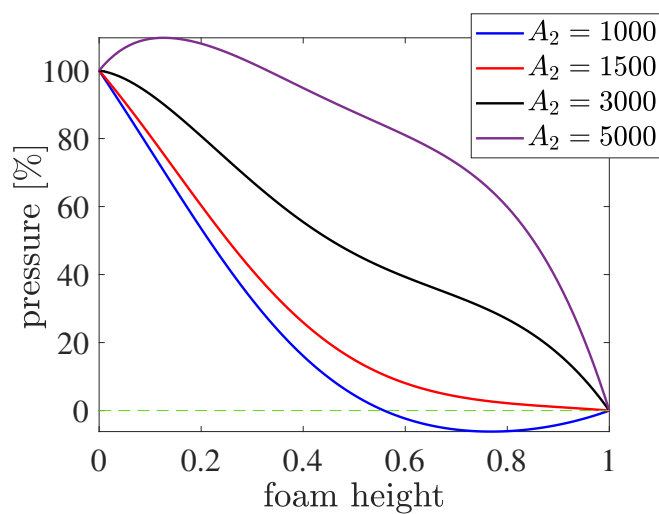


Figure 5.10: The influence of A_2 values on the pressure response.

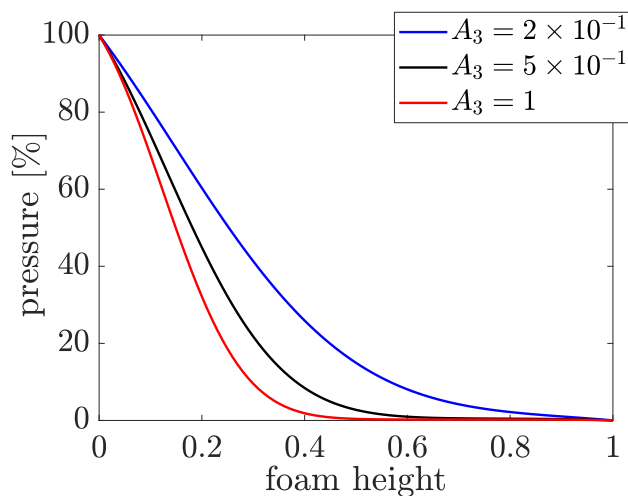


Figure 5.11: The influence of A_3 values on the pressure response.

The influence of different magnitudes of parameter a in the Robin boundary condition of equation 5.43 on the concentration trend is illustrated in Fig. 5.12. The value of parameter a can have a significant impact on the behaviour of the boundary condition and the overall behaviour of the

system it describes. As can be seen in Fig. 5.12, when $a = 0$ the boundary condition simplifies to the Neumann boundary condition. In this case, there is no diffusive flux at the boundary $z = 1$, and the boundary condition is entirely dominated by convection. It represents a situation where there is no mass diffusion across the boundary, and the value of C_∞ controls the rate of convection at the boundary. On the other hand, when $a = 1$ the boundary condition is Dirichlet type. In this case, there is no convection at the boundary $z = 1$, and the boundary condition is entirely dominated by diffusion. It represents a situation where the value of concentration at the boundary is fixed at C_∞ and there is no convective transfer of mass. For any other value of $0 \leq a \leq 1$, the boundary condition is a combination of both diffusion and convection.

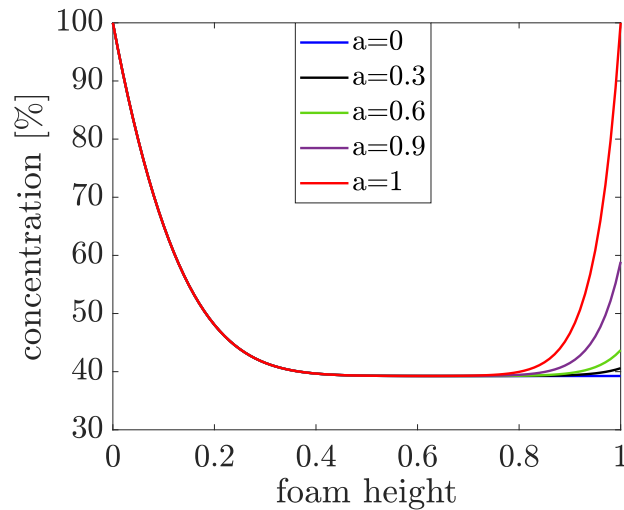


Figure 5.12: The 1D simulation of the concentration response for different values of Robin boundary condition parameter a .

Hence, to proceed with the model investigations, the input parameters are chosen as listed in Table 5.2. For the back-coupling calculations, the volume elements are assumed to be cubes with edge length $dz = 1 \times 10^{-2}$.

Table 5.2: Assumed magnitudes of input parameters

| Constant | Value | Constant | Value |
|----------|--------------------|----------|--------------------|
| A_1 | -1×10^3 | A_2 | 1.5×10^3 |
| A_3 | 2×10^{-1} | a | 9×10^{-1} |

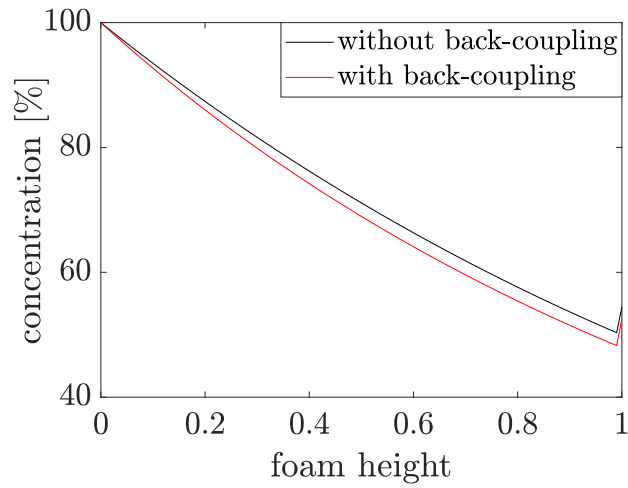
5.2.2 Influence of Back-Coupling Calculations

The following examples deal with the influence of back-coupling calculations on the results and compare the results obtained from a convection-dominant process with the results obtained from a diffusion-dominant process. Each problem is solved once by considering constant geometrical parameters (without back-coupling) and once by considering the changes in geometrical parameters (with back-coupling).

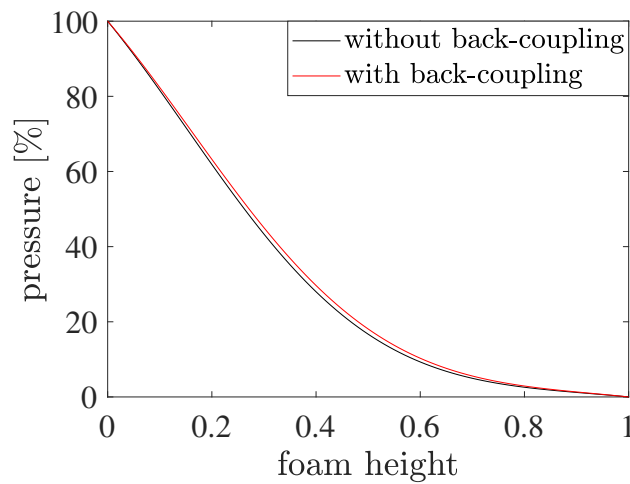
Convection-Dominant Process

In the first example, the process is mainly driven by convection ($\lambda_C \gg \lambda_D$). Fig. 5.13 illustrates the concentration and pressure results obtained with and without back-coupling considerations.

As it is expected the geometry changes have an influence on the coating process in a convection-dominant process. The coating of the foam reduces the pore space and, as a consequence, reduces the permeability. This leads to a reduction in the flow velocity. According to Darcy's law (see equation 3.46), velocity has a direct relation with pressure gradient and lower velocity leads to lower pressure gradient, which can be noticed in Fig. 5.13(b). With the reduction of flow velocity, the concentration of available ions in the electrolyte will reduce accordingly (Fig. 5.13(a)).



(a)



(b)

Figure 5.13: The comparison of (a) concentration distribution and (b) pressure distribution with and without back-coupling calculations, in a convection-dominant process.

The transient concentration response for this example is presented in Fig. 5.14. In these graphs, the green line is the initial state of variables and the red line is the last time step. The effect of flow velocity reduction due to permeability reduction is illustrated in these figures clearly.

Taking a glance at Fig. 5.14(a), it can be seen that the rate of concentration

change remained constant in all the time steps since the permeability is assumed to be constant during the deposition time. While the trends in Fig. 5.14(b) show that the process has become slower over time and the concentration changes at a slower rate as a result of the reduction of permeability in each time step.

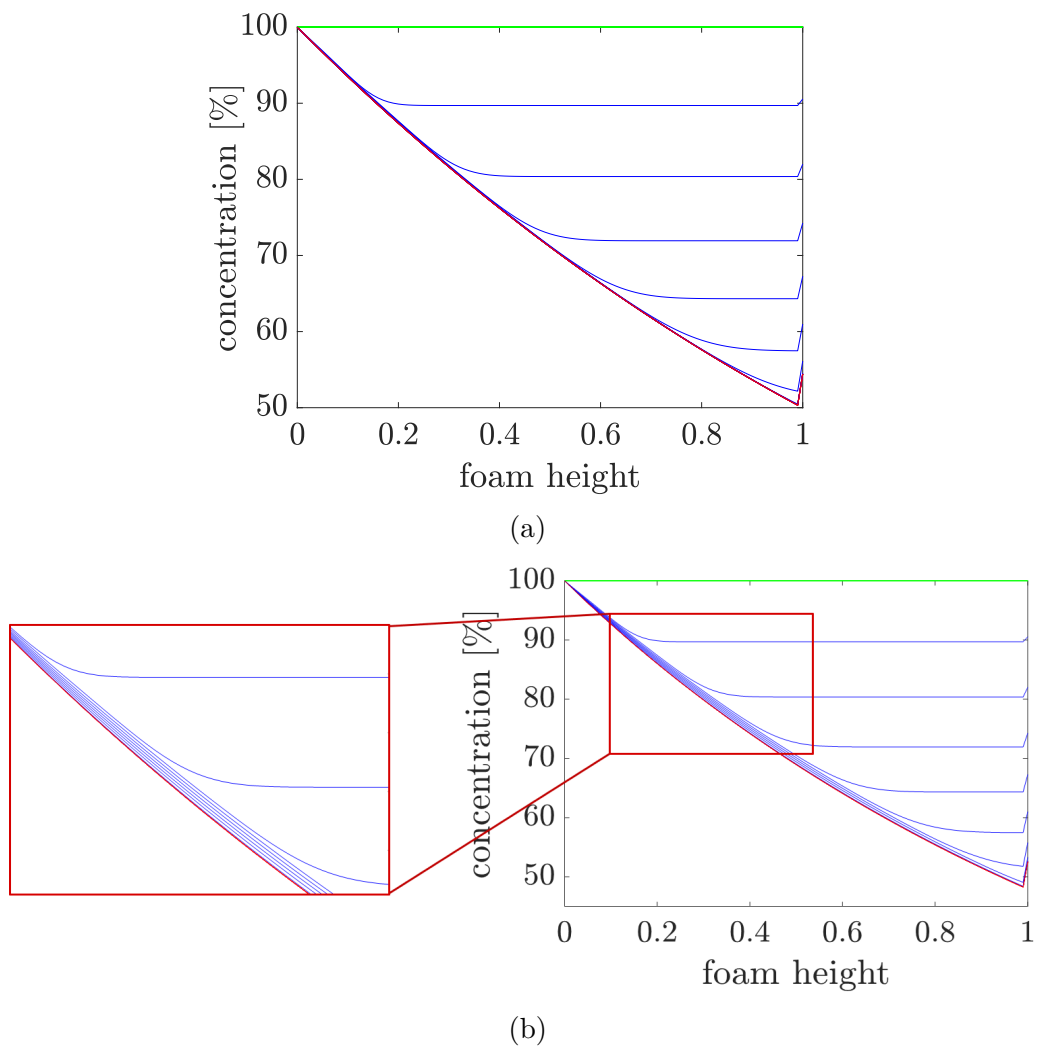


Figure 5.14: The transient concentration response in a convection-dominant process (a) without and (b) with the back-coupling calculations.

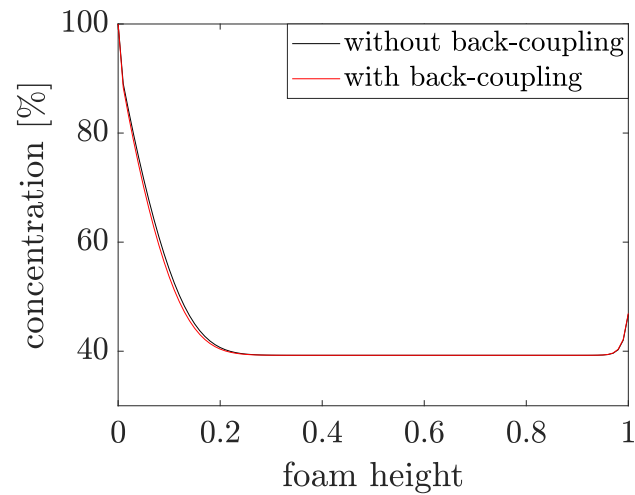
Diffusion-Dominant Process

In the second example, a diffusion-dominant process is considered ($\lambda_D \gg \lambda_C$). Fig. 5.15 shows the concentration and pressure results for such a process. As mentioned before, due to the permeability reduction, the velocity is reduced which, based on Darcy's law, leads to a decrease in pressure gradient (Fig. 5.15(b)). However, a diffusion-dominant process is driven mainly by the concentration gradient and hence, the velocity changes have no considerable effects on the concentration changes. Therefore, as it is shown in Fig. 5.15(a), in a diffusion-dominant process the concentration responses are almost independent of back-coupling calculations.

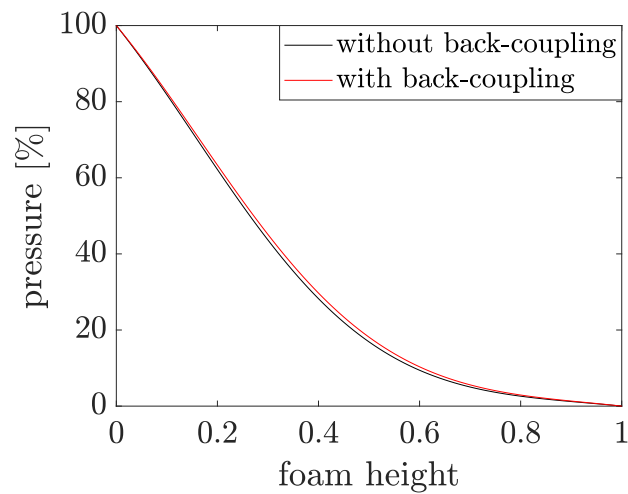
5.2.3 Influence of Diffusion and Convection Intensities

The last example deals with the influence of diffusion and convection intensities on the concentration trend and compares three cases when the diffusion is dominant, when the convection is dominant, and when both mechanisms have the same magnitude of effect. Fig. 5.16 shows the results for the last time step in these cases. The comparison is made once when the diffusion is constant and the change in the ratio only happens through changes in the convection coefficient (Fig. 5.16(a)), and once with the constant convection and varying diffusion coefficient (Fig. 5.16(b)).

Comparing the results shown in Fig. 5.16, one can notice the high sensitivity of the process to the convection influence. It is evident from Fig. 5.16(a) that the change in the convection coefficient, i.e. flow velocity, leads to noticeable changes in the concentration rate. However, by doing a comparable investigation on the diffusion coefficient, the changes in results are negligible (Fig. 5.16(b)). Also comparing the magnitude of ratios, it is apparent that a smaller variation in convection coefficient leads to much noticeable changes in concentration. While to obtain a specific concentration change due to variation in diffusion coefficient, the variation should be of higher orders.

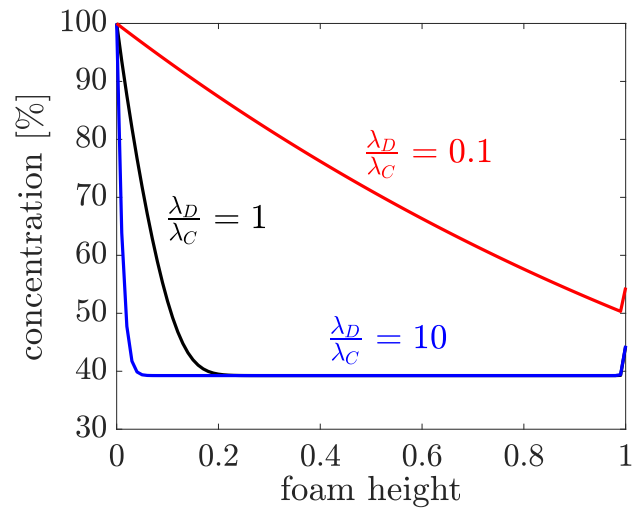


(a)

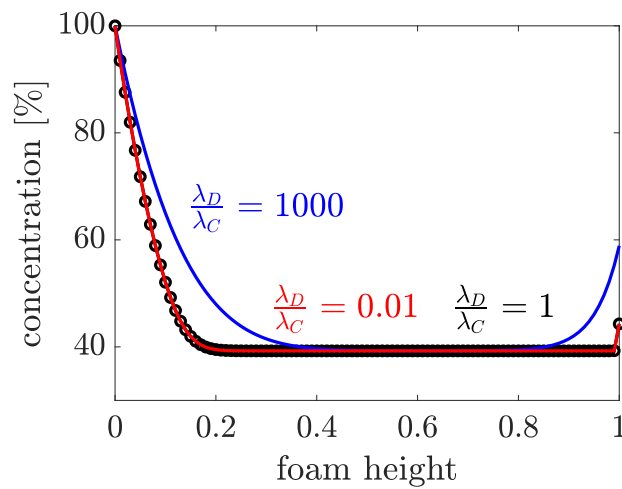


(b)

Figure 5.15: The comparison of (a) concentration distribution and (b) pressure distribution with and without back-coupling calculations, in a diffusion-dominant process.



(a)



(b)

Figure 5.16: Influence of $\lambda_D \backslash \lambda_C$ on the concentration distribution with (a) constant diffusion coefficient and (b) constant convection coefficient.

5.2.4 The Solution to the Full Two-Sided Model

Finally, using the mentioned magnitudes in Table 5.1 and 5.2, and considering the initial and boundary conditions (equations 5.35 - 5.43), the transient response of the equation system (3.52) and (3.53) are calculated.

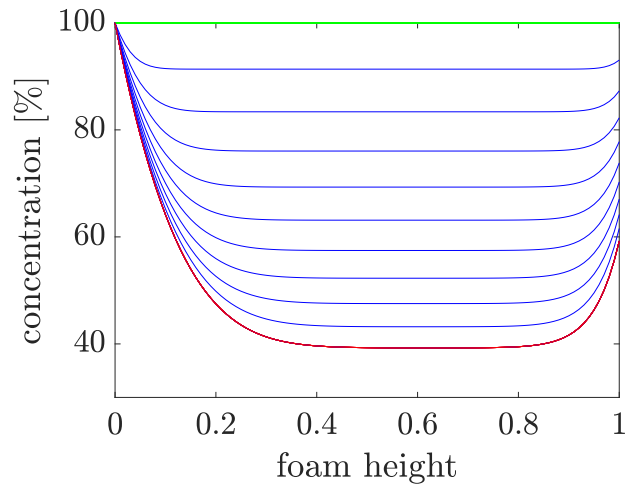
In the presented graphs, the green line is the initial state of variables and the red line is the last time step. As can be seen in Fig. 5.17(a), the concentration of available nickel ions in the electrolyte reduces over time which means that the ions are either deposited on the struts or left the foam through the outlet. Moreover, the trends suggest that at the inlet and outlet of the foam, the concentration of ions is considerably higher than for the areas within the foam. This behaviour has also been observed in the experiments [8, 13]. On the other hand, Fig. 5.17(b) predicts the behaviour of pressure. From a physical point of view, it is expected that the pressure changes show a semi-linear behaviour, which is demonstrated clearly in Fig. 5.17(b).

The back-coupling calculation related to the coating thickness and changes in permeability is shown in Fig. 5.18.

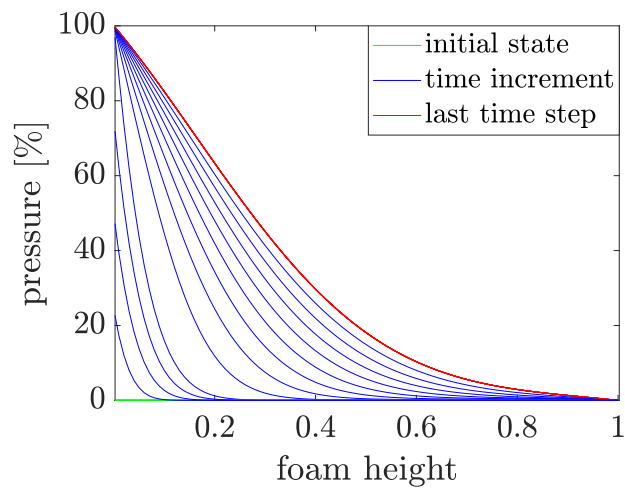
Fig. 5.18(a) represents the final coating thickness of the foam at the end of the process. With the start of the coating process, as the coating thickness increases, the permeability of the foam reduces accordingly. Since the coating thickness is higher at the inlet and outlet of the foam, the permeability is smaller in these areas than in the middle part of the foam.

By Knowing the local transient values of permeability and porosity, and calculating the local pressure gradient at each point of the domain, the local transient velocity can be calculated using the Darcy equation. Fig. 5.19 shows the influence of coating on the velocity magnitudes over the foam height. This figure depicts that the velocity generally decreases with time. This reduction is due to the increasing ion deposition during the time. As the coating thickness increases, the permeability and hence the flow velocity will decrease. Comparing Fig. 5.18 (b) and Fig. 5.19, it is noticeable that the velocity had more significant drops at the inlet and outlet of the foam, where the permeability showed lower values as well.

In addition, another aspect revealed by the graph is a sharp velocity difference at the initial time steps of the process. The reason can be that at the initial stages of the process, it takes some time for the pump to reach



(a)



(b)

Figure 5.17: The transient distribution of (a) concentration and (b) pressure within the foam height in the direction of flow.

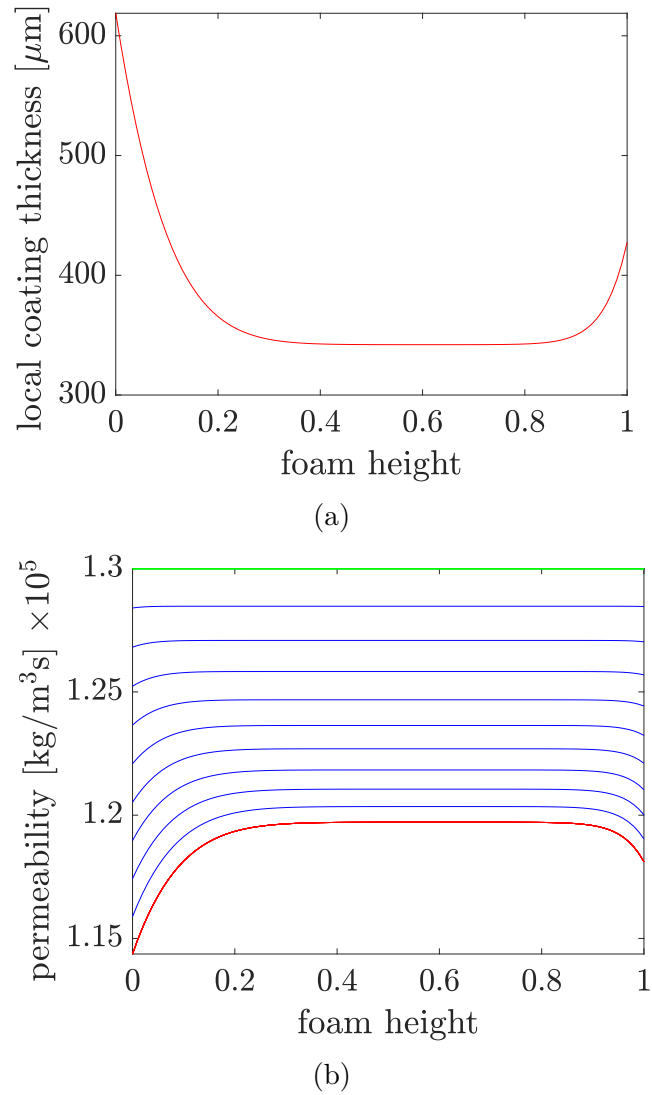


Figure 5.18: The back-coupling results of (a) coating thickness evolution and (b) permeability changes within the foam height in the direction of flow.

its full capacity (see pressure boundary condition equation 5.41) and for the flow to reach a homogeneous velocity over the foam height and therefore, the velocity is higher at the inlet, where the pump is. After a short time, the flow velocity reaches a constant magnitude over the foam height. With the start of the deposition, the velocity would be mostly influenced by the changes in the foam geometry.

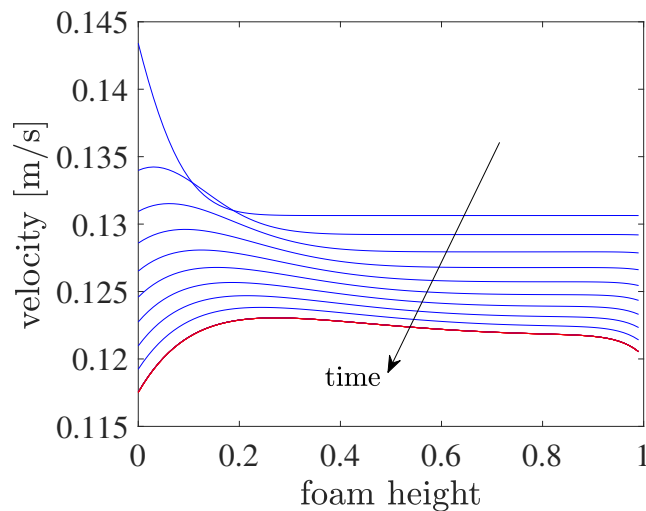


Figure 5.19: The transient velocity distribution over the foam height.

The purpose of this investigation was to show some of the many potentials of the proposed model. This model offers the possibility to investigate the influence of different parameters on the results and to show the share of each transfer mechanism in the coating process separately. All the results shown so far were computed considering a constant coefficient for migration and sink term. The model can be used for further investigations of the influence of these mechanisms on the final results. In addition, the definition of the constitutive equations for the production term and the fluid density gives three more controlling parameters to adjust the model in order to obtain physically meaningful results.

The calculated reduced ion concentration as shown in Fig. 5.17(a) is partly due to the deposition and partly related to the ions that left the volume element with the flow of electrolyte. The proposed method to calculate the coating thickness makes it possible to distinguish the share of concentration related to the deposited ions.

Furthermore, differences to the experiment may be used to further modify the model by adjusting the input parameters and the boundary conditions.

5.2.5 Convergence Study

The obtained solutions from numerical methods are accompanied with deviations from the analytical solutions of PDEs. The magnitudes of these deviations can be influenced by the size of time and space discretization. Performing convergence studies on the adopted numerical method is a standard approach to estimate the sensibility of the numerical solution.

The problem is solved for different values of Δz and Δt and the error E is calculated according to equation 4.18. Table 5.3 lists the corresponding numerical errors and calculation times for the solved problem in section 5.2.4. For a better comparison, the error is also depicted in Fig. 5.20.

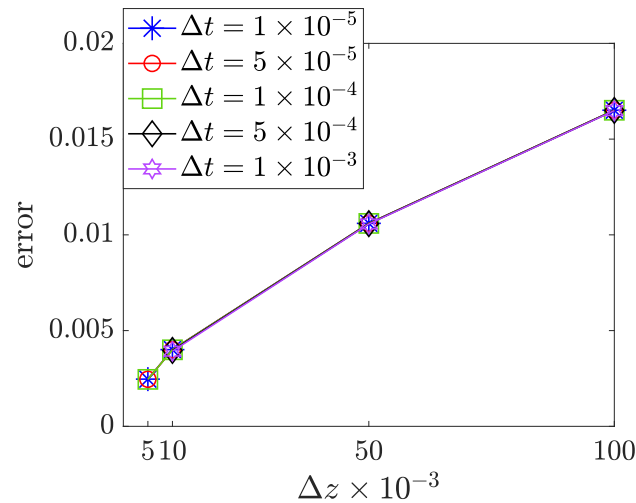


Figure 5.20: Numerical error for the test problem of section 5.2.4 for different sets of discretization parameters.

As can be seen, choosing a smaller spatial grid size results in a lower magnitude of error. However, the size of the time step does not have any influence on the accuracy of the solution and only results in an unnecessary increase of the time costs.

Table 5.3: Numerical comparisons for different sets of discretization parameters for the test problem of section 5.2.4

| Δt | Δz | $E \times 10^{-3}$ | Time (s) |
|--------------------|--------------------|--------------------|----------|
| 1×10^{-3} | 1×10^{-2} | 3.9 | 0.73 |
| | 5×10^{-2} | 10.6 | 0.64 |
| | 1×10^{-1} | 16.5 | 0.68 |
| 5×10^{-4} | 1×10^{-2} | 4 | 1.07 |
| | 5×10^{-2} | 10.6 | 0.95 |
| | 1×10^{-1} | 16.5 | 1.02 |
| 1×10^{-4} | 5×10^{-3} | 2.5 | 5.85 |
| | 1×10^{-2} | 4 | 5.28 |
| | 5×10^{-2} | 10.6 | 4.31 |
| | 1×10^{-1} | 16.5 | 4.2 |
| 5×10^{-5} | 5×10^{-3} | 2.5 | 20.19 |
| | 1×10^{-2} | 4 | 18.79 |
| | 5×10^{-2} | 10.6 | 13.62 |
| | 1×10^{-1} | 16.5 | 14.45 |
| 1×10^{-5} | 5×10^{-3} | 2.5 | 455.89 |
| | 1×10^{-2} | 4 | 447.48 |
| | 5×10^{-2} | 10.6 | 387.30 |
| | 1×10^{-1} | 16.5 | 355.53 |

The proposed model consists of different physical terms. Corresponding to the nature of each term, a combination of first- and second-order schemes have been used. For a better comparison of the influence of each scheme, the convergence study has been performed for a diffusion-dominant and a convection-dominant problem. The problem is solved

for three magnitudes of $\Delta t = \{10^{-5}, 10^{-4}, 10^{-3}\}$ and four magnitudes of $\Delta z = \{5 \times 10^{-3}, 10^{-2}, 5 \times 10^{-2}, 10^{-1}\}$. As shown in Fig. 5.21, in both convection- and diffusion-dominant cases, the time step size does not have any influence on the solution and the error is only reduced by choosing a smaller spatial discretization. However, it can be seen that the convergence of the diffusion-dominant problem is second-order which corresponds to the chosen second-order FDM scheme, while the convection-dominant problem has a first-order convergence according to the chosen upwind scheme. Therefore, depending on the problem's parameters and weighing of these different effects, the convergence should move between first- and second-order.

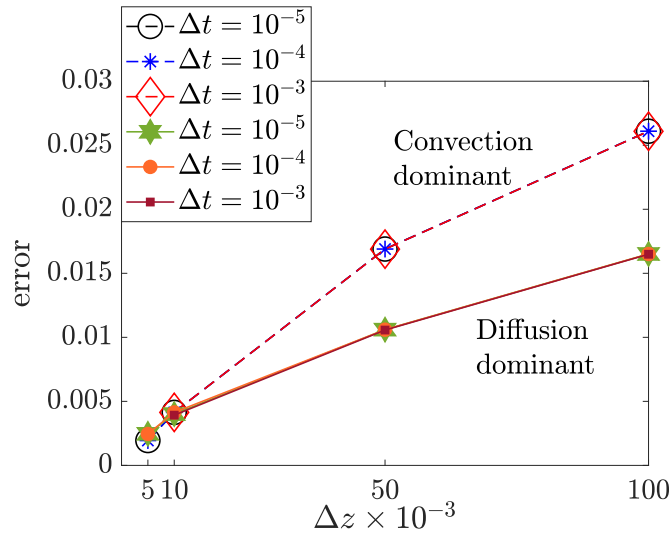


Figure 5.21: Comparison of the order of convergence in a convection-dominant problem and a diffusion-dominant problem.

5.3 Modelling the Ni/PU Coating Process: Simulation vs. Experiment

In this section, the real experimental conditions of the Ni/PU coating process are considered and simulated using the proposed model. However, to investigate the problem numerically it is important to reduce the number of parameters by assuming the process as simple as possible. Moreover, due to the large disparity between real time and space domain ranges, divergence and stability issues can arise. In this case, normalizing can help balance the discretization and improve the accuracy of simulations. Hence, inspired by the previous section, by suitable substitutions of variables and characteristic numbers, temporal and spatial domains as well as the process variables are normalized. Therefore, the problem is modeled on a square computational domain with a length of 1, in the $y - z$ plane in the middle of the foam, as shown in Fig. 5.22. The square numerical domain has been scaled according to the lengths of the rectangular sample domain.

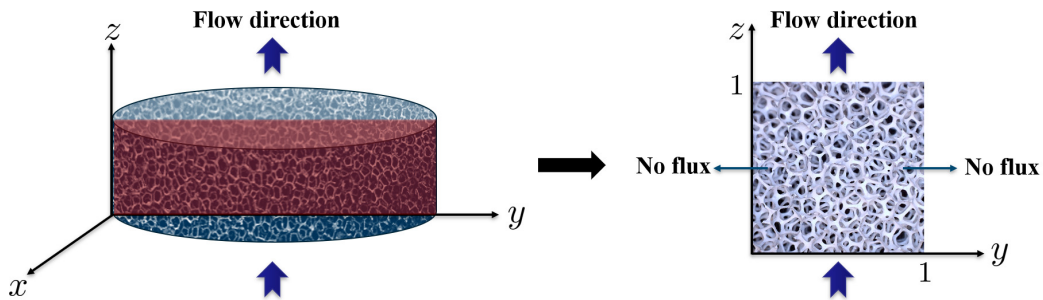


Figure 5.22: Normalized 2-dimensional problem domain from the $y - z$ foam's mid-plane, with the direction of flow against gravity.

The investigated domains for the experimental results are cuboid specimens with the size of $20 \text{ mm} \times 20 \text{ mm} \times 40 \text{ mm}$, being cut from the cylindrical, disc-like foam with the diameter of 210 mm and thickness of 40 mm (see Fig. 5.23) [8, 81]. The global investigations are done on the plane $y - z$ parallel to the flow (Fig. 5.22), as well as the plane $x - y$ perpendicular to the flow (Fig. 5.23(a)). The local and semi-local results are investigated on three specimens

taken from both sides and the center of the foam and at three positions (top, bottom, and center) of each of these specimens (Fig. 5.23(b)).

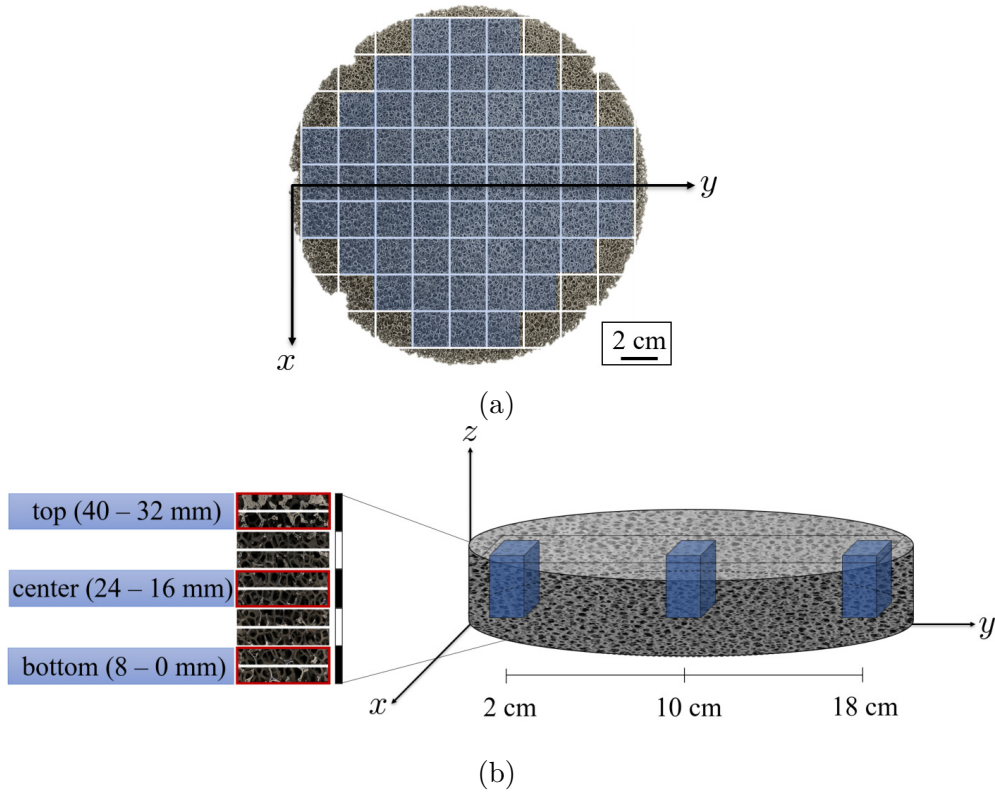


Figure 5.23: Cuboid specimens cut out of the disc-like foam specimen and the analysed top, center, and bottom domains [8, 81].

Hence, for the numerical modelling, the respective dimensions and positions are specified on the normalized domain according to the experimental assumptions.

Considering the problem domain in Fig. 5.22, the corresponding initial and boundary conditions are defined in such a way to represent the experiment's conditions in [8] and yet be as simple as possible.

Initially, under the absence of any applied pressure or electrical current, the foam is plunged into the electrolyte with a homogeneously distributed ion concentration realized from the infinite ion reservoirs. Hence, the initial conditions at any point $\mathbf{x} = (y, z)$, are:

$$c(\mathbf{x}, 0) = C_\infty \quad (5.46)$$

$$p(\mathbf{x}, 0) = p_0 \quad (5.47)$$

$$E(\mathbf{x}, 0) = E_0 \quad (5.48)$$

According to the experiment, the process starts when the pump reaches the designated pressure P_{max} at the inlet. Moreover, an inhomogeneous inlet flow velocity has been reported in experimental measurements [8, 81]. Hence, based on Darcy's law, the pressure distribution at the inlet of the foam should be inhomogeneous. On the other hand, the lower anode in the reactor setup of Fig. 2.1 provides an infinite ion reservoir at the inlet. The concentration of the ions in this area is kept constant via the ion reservoir (anode) and can be described using a Dirichlet type boundary condition. In the simplified model, it is assumed that the electrical field at the inlet of the foam is only affected by the applied external electric current. All in all, the inlet boundary conditions are:

$$c(y, 0, t) = C_\infty \quad (5.49)$$

$$p(y, 0, t) = (P_{max} - P_0)y \quad (5.50)$$

$$E(y, 0, t) = E_1 \quad (5.51)$$

Similar to the arguments in the previous section, the ion concentration on the outlet of the foam can be described by a Robin boundary condition to take into account the influence of convection (the pump) and diffusion (the upper anode). Moreover, the pressure reaches the constant outlet pressure p_0 . Hence, considering the same argument about the electrical field at the inlet, the boundary conditions at the outlet are:

$$a c(y, 1, t) + (1 - a) \frac{\partial c(y, 1, t)}{\partial z} = a C_\infty \quad (5.52)$$

$$p(y, 1, t) = p_0 \quad (5.53)$$

$$E(y, 1, t) = E_1 \quad (5.54)$$

In the simplified model, it is assumed that there will be no flux from the right and left sides of the foam. Hence, a Neumann type boundary condition will be defined for all the variables on both sides:

$$\frac{\partial c(0, z, t)}{\partial z} = \frac{\partial c(1, z, t)}{\partial z} = 0 \quad (5.55)$$

$$\frac{\partial p(0, z, t)}{\partial z} = \frac{\partial p(1, z, t)}{\partial z} = 0 \quad (5.56)$$

$$\frac{\partial E(0, z, t)}{\partial z} = \frac{\partial E(1, z, t)}{\partial z} = 0 \quad (5.57)$$

According to the experiment conditions described in [8, 81], the process temperature is assumed to be kept constant at 50° C, and an external current density of 16.5 A/m² is applied on a PU foam with 90 percent initial porosity [8]. The magnitudes of different physical constants in the proposed model are listed in Table 5.1.

The input parameters in the problem are chosen as listed in Table 5.4.

Table 5.4: Assumed magnitudes of input parameters

| Constant | Value | Constant | Value |
|----------|--------------------|----------|--------------------|
| A_1 | -1×10^2 | A_2 | 1.5×10^3 |
| A_3 | 2×10^{-1} | a | 9×10^{-1} |

The representative normalized time and space ranges and steps are defined as:

$$0 \leq t \leq 1; \quad \Delta t = 10^{-3} \quad (5.58)$$

$$0 \leq y \leq 1; \quad \Delta y = 10^{-2} \quad (5.59)$$

$$0 \leq z \leq 1; \quad \Delta z = 10^{-2} \quad (5.60)$$

In the following, the simulation results using the parameters in Tables 5.1

and 5.4 are presented. Moreover, the experimental results are simulated with the proposed model and compared with the respective numerical results.

5.3.1 Numerical Simulation: Global Results

The last time step responses of the defined problem at the considered domain of Fig. 5.22 are presented in this section.

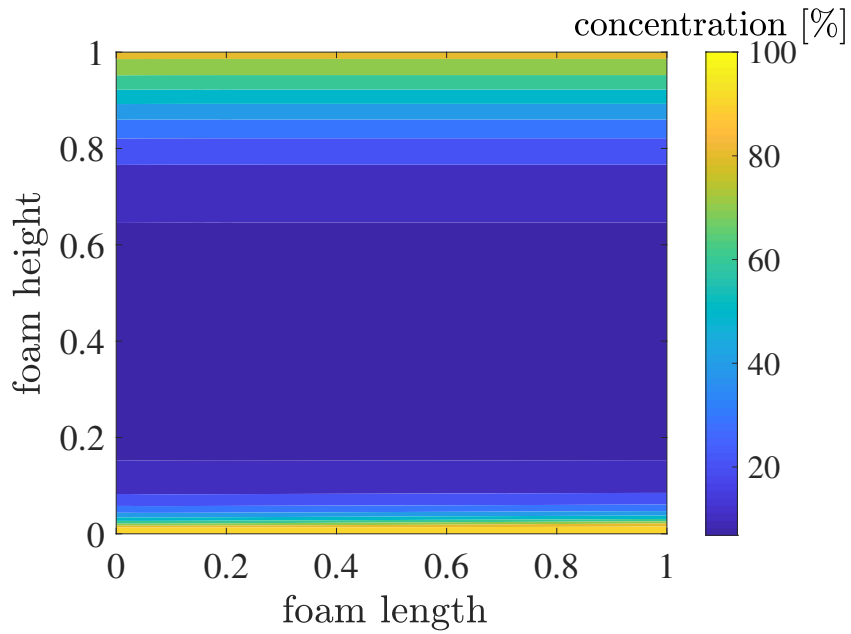
Fig. 5.24 (a) presents the ion concentration distribution in the foam domain. The concentration of ions is considerably higher at the inlet and outlet of the foam and it reaches an almost constant value in the central areas. This behaviour has been also reported in the experimental observations [8].

The z -component of the electrical field distribution in the domain is calculated based on the equation (3.55) and depicted in Fig. 5.24 (b). The experimental analysis of the coating thickness distribution shows significantly increased amounts of nickel in the upper (outlet) and lower (inlet) areas of the foam. The higher coating thicknesses in these areas can be explained by a higher ion concentration. The decrease of the concentration towards the foam center can be explained by the reduced mass transport. The decreasing electric field to the foam center is related to the open porous, conductive hybrid foam structure as well as the Faraday law.

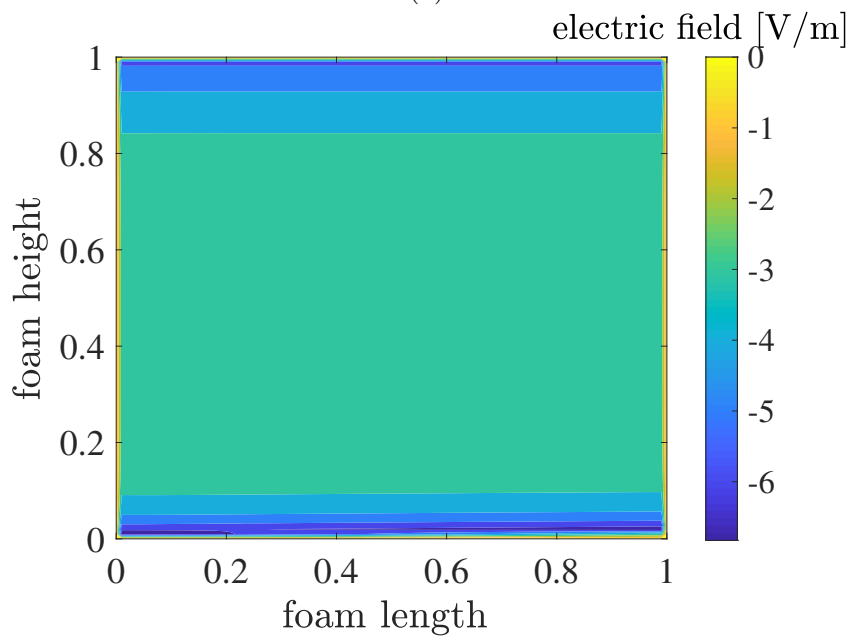
As mentioned in the previous section, the discretization size plays an important role in the accuracy of the obtained results. The problem is solved again for a bigger spatial grid. Fig. 5.25 depicts the concentration and electric field for $\Delta z = 5 \times 10^{-2}$. Comparing Fig. 5.24 and Fig. 5.25, the influence of discretization size on the boundary layer is evident.

The pressure distribution inside the foam domain is presented in Fig. 5.26 (a). The effect of a heterogeneous inlet flow has been modelled and shown here. The pressure distribution in Fig. 5.26 (a) represents the velocity distribution reported in experimental results [8, 81], which gives a qualitative agreement between the experiment and the simulation results.

Furthermore, it is expected that the pressure change from the inlet to the outlet has a semi-linear behaviour. The transient pressure response in the direction of the flow at the middle of the foam at $y = 0.5$ is shown in Fig. 5.26 (b). In this figure, the green line is the initial pressure and the red line is the last time step.

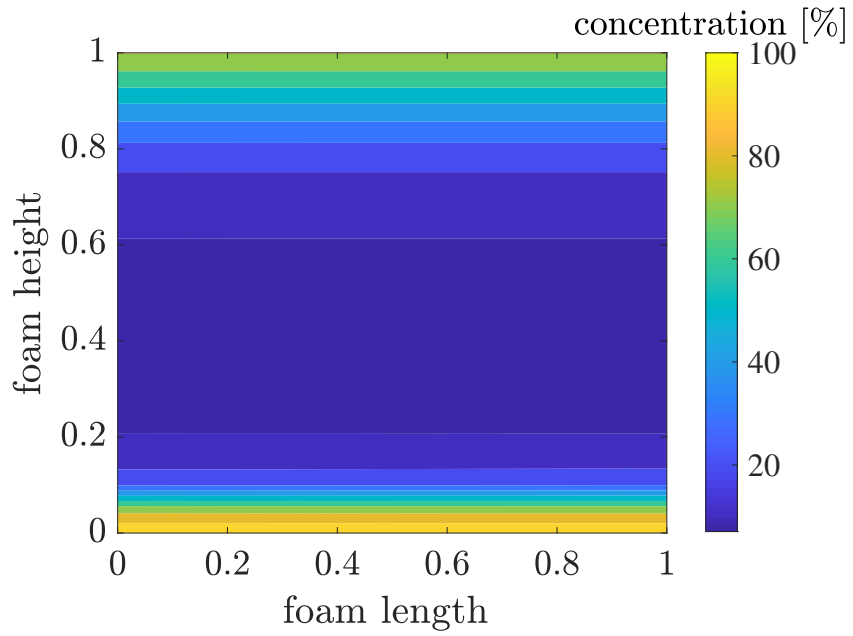


(a)

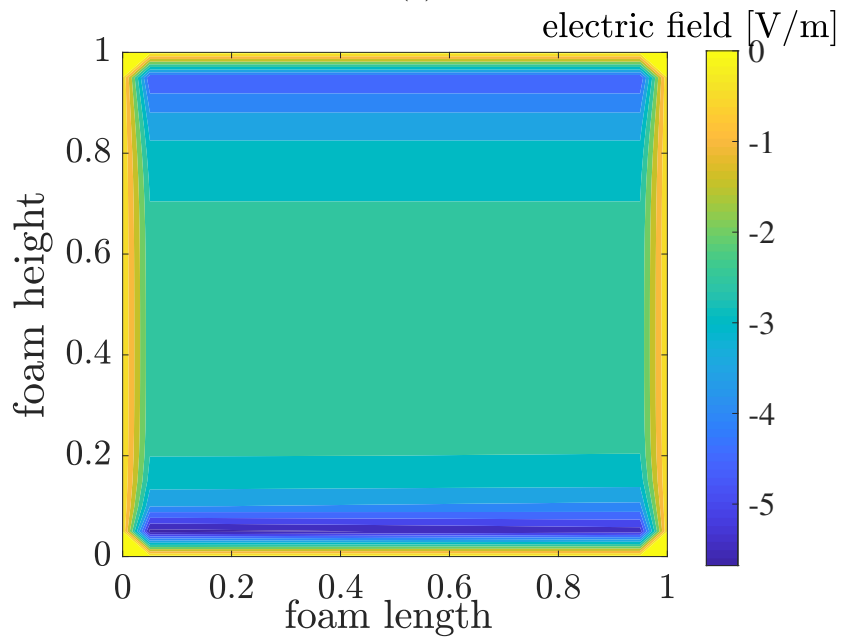


(b)

Figure 5.24: The 2D simulation of the distribution of (a) concentration and (b) electrical field (E_z) in the $y-z$ plane.

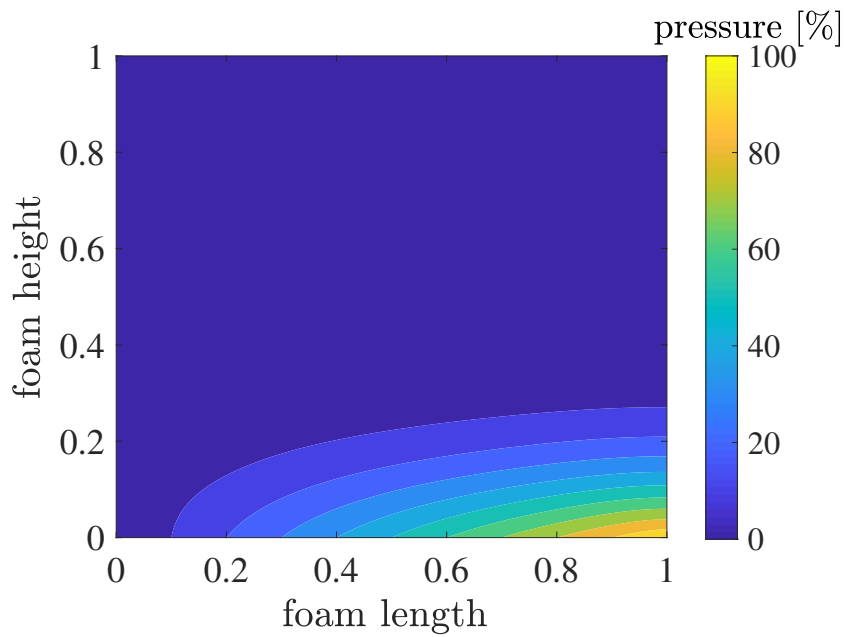


(a)

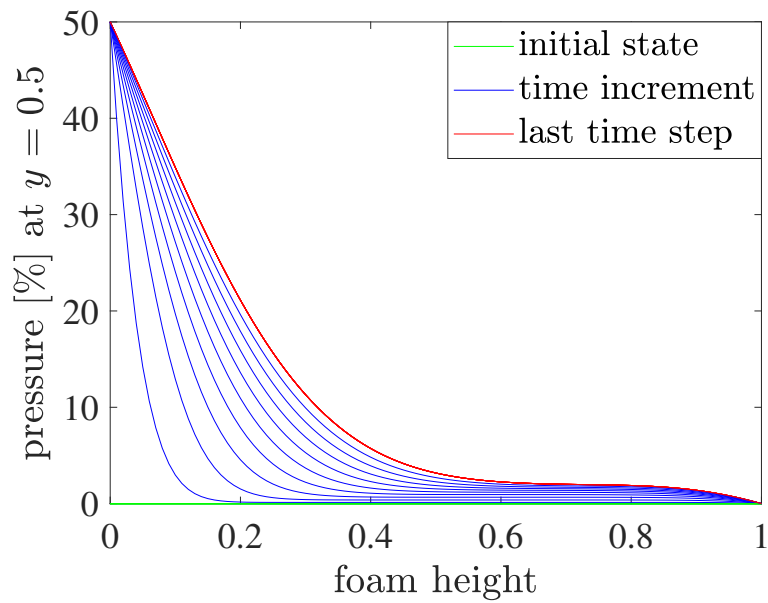


(b)

Figure 5.25: The 2D simulation of the distribution of (a) concentration and (b) electrical field (E_z) in the $y - z$ plane with a bigger spatial grid $\Delta z = 5 \times 10^{-2}$.



(a)



(b)

Figure 5.26: (a) The 2D pressure distribution simulation in the $y - z$ plane. (b) The 1D transient pressure distribution at the middle of inlet ($y = 0.5$) in the flow direction.

5.3.2 Numerical vs. Experimental Results: Global Coating Thickness Distribution

The experimental gravimetric measurements of global specific density distribution in the cuboid specimens of the Ni/PU foam, specified by the red line (Fig. 5.27 (a)) are depicted in Fig. 5.27 (b) [8, 81].

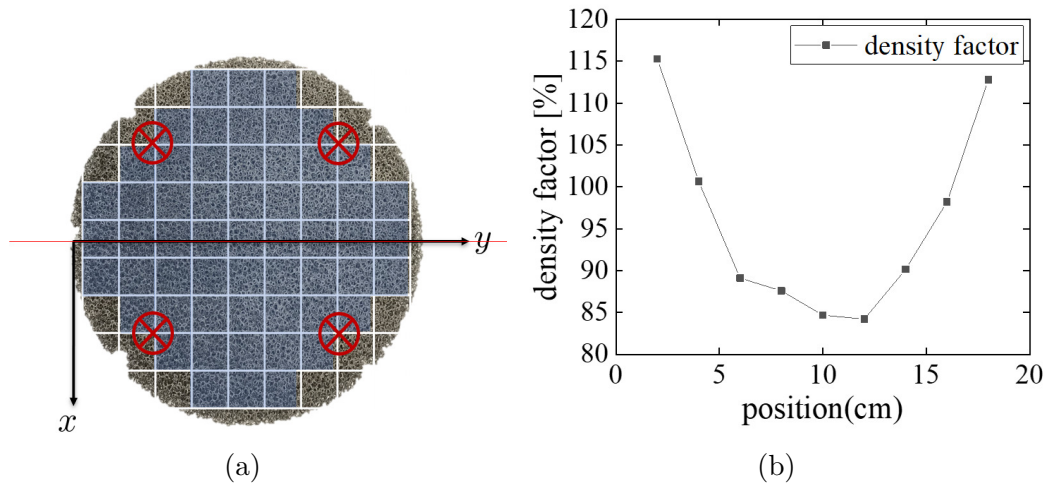


Figure 5.27: **Experimental results:** (b) Gravimetric measurements of global specific density distribution in the cuboid specimens on the red line shown in (a). The crossed circles (\otimes) show the inlet points of the current during electrodeposition [8, 81].

To obtain a comparable numerical result corresponding to Fig. 5.27 (b), the specific density can be associated with the normalized total coating thickness in each specimen. Using the proposed model, the global coating thickness in the $y - z$ plane in the middle of the foam is calculated and divided by the average total coating thickness of all specimens. The result is presented in Fig. 5.28.

The trends in both experimental and numerical analysis show that the coating distribution is higher at the edges and it reduces in the inner areas of the foam. The numerical result shows a good qualitative agreement with the trend in Fig. 5.27 (b). However, the quantitative comparison of experimental measurements with numerical calculations, shows 9.5% and 16.5% deviations

in the highest and lowest magnitudes, respectively.

The coating distribution inhomogeneities can be the result of different factors such as the locations of introduced electric current (Fig. 5.27 (a)) which can lead to a non-homogeneous electric field and edge effects [82], or the non-homogeneous flow velocity. Therefore, in order to reach a more accurate simulation, it is important to consider the experimental conditions in the initial and boundary conditions.

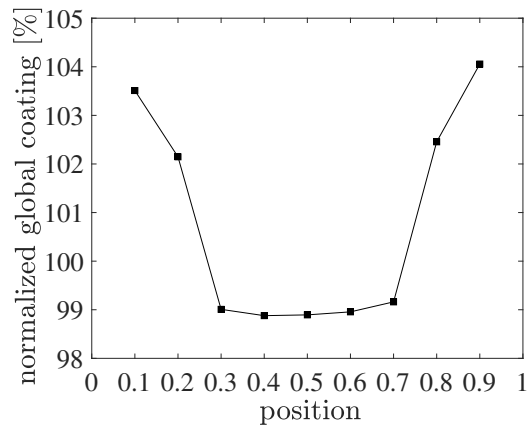


Figure 5.28: **Numerical results:** Computed global normalized coating thickness distribution along the red line shown in Fig. 5.27(a).

5.3.3 Numerical vs. Experimental Results: Local and Semi-local Coating Thickness Distribution

In this section, the semi-local and local coating thickness is investigated in three specimens taken from both sides and from the center of the foam (Fig. 5.23 (b)). The experimental results are compared with the simulation results at the respective positions of the numerical domain.

Fig. 5.29 shows the experimental measurements of the semi-local (Fig. 5.29 (a)) and local (Fig. 5.29 (b)) coating thickness at the intended cuboid specimens and the mentioned locations on each specimen [8, 81].

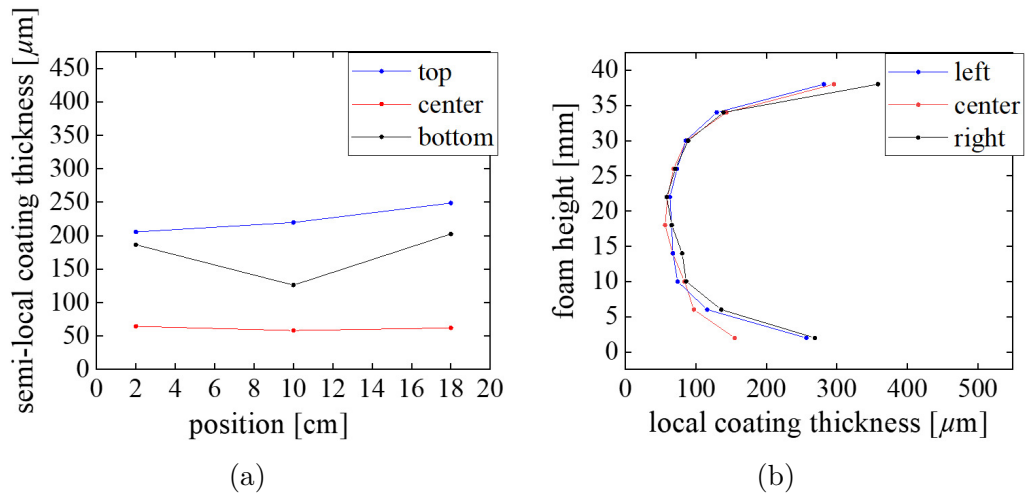


Figure 5.29: **Experimental results:** Analysis of three characteristic cuboid specimens from the hybrid foam plate in Fig. 5.23 (b). (a) Semi-local coating thickness distribution with the averaged thickness values of the top, center, and bottom of the cuboid specimen and (b) local coating thickness distribution within each analysed cuboid specimen [8, 81].

Fig. 5.30 depicts the simulation results for the semi-local and local coating distribution in the considered specimens. The semi-local trends depict the high coating thickness on the top (outlet) and bottom (inlet) parts and lower coating thickness for the center of the specimens. These trends indicate the same observations as the previous results, where higher thicknesses are observed on the edges and the coating distribution decreases toward the inner of the foam.

The trends qualitatively show a good agreement between the model and the experimental results. The quantitative comparison represents a close agreement of the results for the bottom and center and an offset of $20 \mu\text{m}$ for the top of the foam.

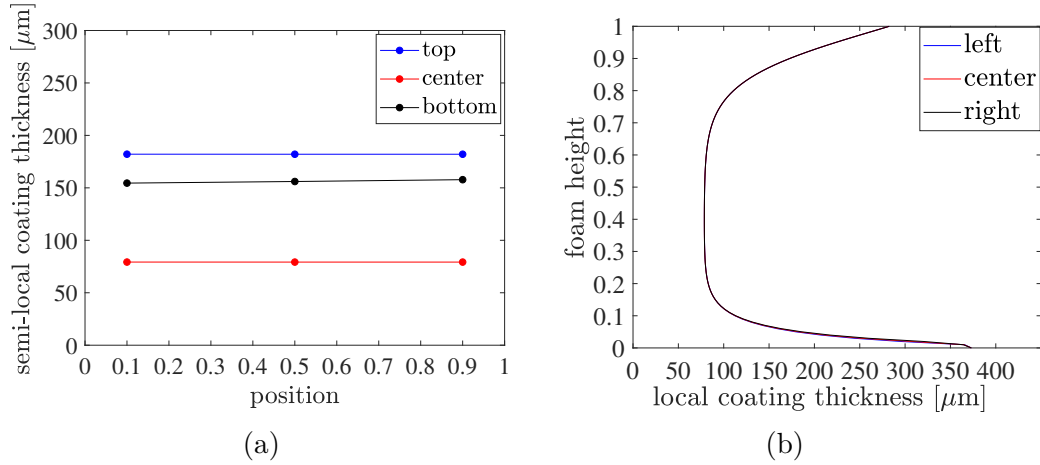


Figure 5.30: **Numerical results:** Numerical simulations of the analysis of three characteristic cuboid specimens shown in Fig. 5.23 (b). (a) Semi-local coating thickness distribution with the averaged thickness values of the top, center, and bottom of the cuboid specimen and (b) local coating thickness distribution within each analysed cuboid specimen.

The difference in the semi-local results for the bottom of the specimens is due to the definition of the boundary condition in this area. For the sake of simplicity, a constant Dirichlet boundary condition has been defined (see equation 5.49) and the occurring turbulence on both sides of the inlet near the walls has been neglected. This turbulent flow can affect the distribution of ions in these areas and cause a non-homogeneous ion distribution. Hence, the inlet area can be divided into the parts near the walls with high ion concentration and an inner central part with lower concentration levels. Considering the influence of the flow turbulence in the local distribution of ions in the electrolyte, the inlet concentration boundary condition can be modified and assumed as follows:

$$c(y, 0, t) = \begin{cases} C_\infty & 0 \leq y \leq 0.2 \\ 0.7 C_\infty & 0.2 < y < 0.8 \\ C_\infty & 0.8 \leq y \leq 1 \end{cases} \quad (5.61)$$

Moreover, taking a look at Fig. 5.27 (a), the local influence of the electrical field at both sides of the foam should also be considered. Therefore, the electrical boundary condition at the inlet and outlet of the foam is not of a homogeneous Dirichlet type; rather, it should be modified as follows:

$$E(y, 0, t) = E(y, 1, t) = \begin{cases} E_1 & 0 \leq y \leq 0.2 \\ 0.7 E_1 & 0.2 < y < 0.8 \\ E_1 & 0.8 \leq y \leq 1 \end{cases} \quad (5.62)$$

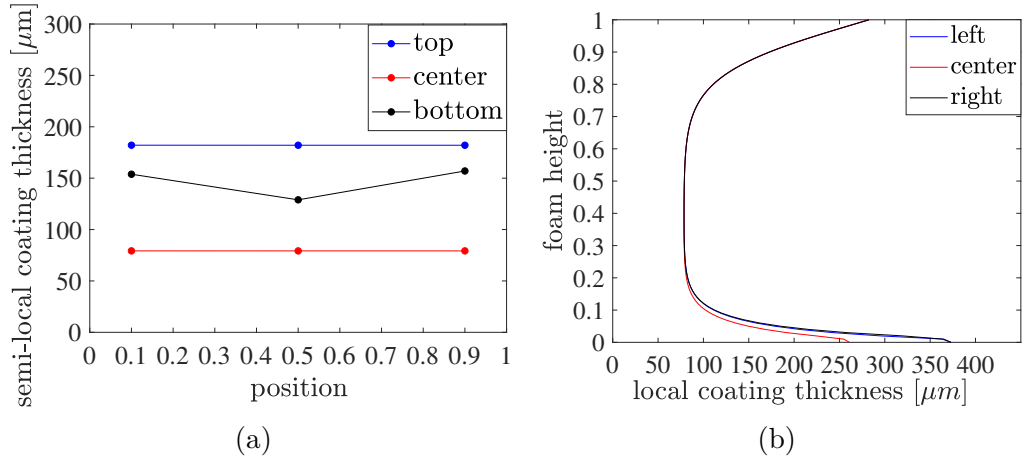


Figure 5.31: **Numerical results:** Using modified boundary conditions in numerical simulations of the analysis of three characteristic cuboid specimens shown in Fig. 5.23 (b). (a) Semi-local coating thickness distribution with the averaged thickness values of the top, center, and bottom of the cuboid specimen and (b) local coating thickness distribution within each analysed cuboid specimen.

The simulation results for the modified boundary condition in equations (5.61) and (5.62) are shown in Fig. 5.31. They show an improved agreement with the experimental results of Fig. 5.29. The comparison between Fig. 5.30 and 5.31 gives an emphasis on the importance of the proper choice of boundary conditions to obtain a more precise simulation.

5.3.4 Numerical vs. Experimental Results: Investigation of Flow

Investigating and understanding the flow behaviour through the open-cell foam assists in understanding its influence on the coating characteristics. It can help identify the coating-related problems and implement appropriate corrective measures. Fig. 5.32 depicts the components of flow velocity along the inlet of the foam. This estimation has been derived using CFD simulation developed by Autodesk. The input data are based on the conditions and measured parameters in the experiment. Moreover, an .stl file describing the geometry of the foam was used as the input data of software to compute the internal flow velocity. A detailed description can be found in [8].

The proposed model in this study is capable of the calculation of pressure distribution in the domain. According to Darcy's law, the velocity is related to the negative pressure gradient ($\mathbf{v} \propto -\text{grad}p$). The negative pressure gradient corresponding to the z - and y -velocity component in the direction of the inlet is shown in Fig. 5.33. Once more, the qualitative comparison of the trends reveals the ability of the model to predict the experimental conditions.

The flow velocity has been calculated using the obtained results of pressure gradient and Darcy's law. Fig. 5.34 depicts the z and y components of velocity corresponding to the Fig. 5.32. Comparing the two figures, the numerical results for V_y show a very good qualitative and quantitative agreement with the CFD simulations. The obtained result for V_z from the model, seems to be in an acceptable range, comparing with the CFD simulation. However, the qualitative comparison shows a different trend at the start of the foam. This deviation can be due to the simplifying assumption of laminar condition for the flow and neglecting the turbulence effects at the inlet which consequently led to the use of Darcy's law.

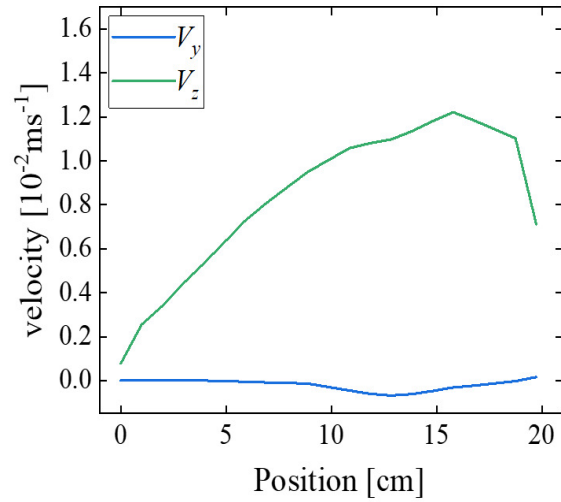


Figure 5.32: **Results obtained from experimental input data:** CFD simulation of the electrolyte flow velocity inside the deposition area along (V_z) and across (V_y) the inlet direction [8].

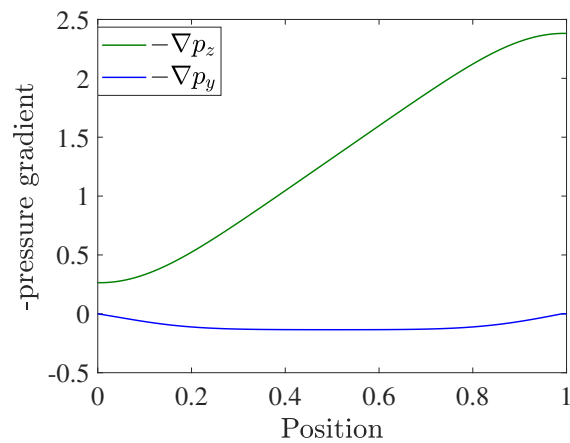


Figure 5.33: **Numerical results:** Numerical modelling of the pressure gradient inside the deposition area along and across the inlet direction.

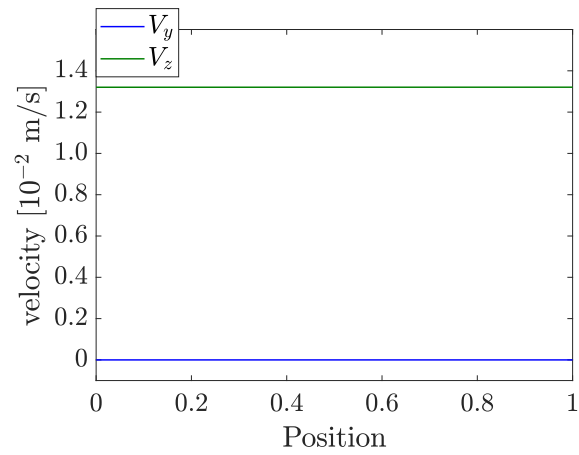


Figure 5.34: **Numerical results:** Numerical modelling of the velocity inside the deposition area along (V_z) and across (V_y) the inlet direction using the Darcy relation.

6

Conclusion and Future Works

6.1 Conclusion

The aim of this work was to propose a method to model the coating process of polyurethane foams with nickel via electrodeposition. A comprehensive description of the physical process and the experiment's conditions has been given and the process variables and the flow behaviour have been accordingly modelled. The problem has been investigated in the framework of continuum mechanics for mixtures and the main transport mechanisms, namely, diffusion, convection and migration, have been taken into account. Moreover, the deposition of ions has been considered via an additional sink term.

In this regard, the governing system of equations for this problem has been derived using the fundamental balance equations of mass and momentum for each constituent and the mixture as a whole. Considering simplifying assumptions and defining suitable constitutive equations for the secondary unknowns, a closed system of equations has been obtained which results in the calculation of time-derivatives of concentration and pressure distribution throughout the foam. Using the displacement current equation, a third equation has been coupled to the system of equations to calculate the electrical

potential from the electric field.

The proposed model is capable of dealing with the gradual geometrical changes with deposition and updating the parameters by introducing a back-coupling technique. Using the Butler-Volmer equation along with Faraday's law of electrolysis, the coating thickness has been calculated. Therefore, the parameter changes during the process and their influences on the deposition have been taken into account.

The finite difference method has been used to solve the equations and the accuracy of the solution has been examined by performing a convergence study along with other validation techniques.

The results obtained from the simulations exhibit the ability of the model to describe the experimental observations. The proposed model is able to investigate the influence of different processes and parameters on the concentration distribution. The comparison of numerical and experimental results exhibits a strong qualitative correlation and a promising capability of the model to improve the coating process and the homogeneity of coating.

The main results and conclusions can be summarized as follows:

- Different fields, such as the transient response of concentration, pressure and electric field distribution, local and global coating thickness and permeability changes can be obtained from the proposed model.
- Reducing the spatial grid size plays a significant role in the accuracy and convergence of the responses. Whereas reducing the time step size does not have any influence on the convergence of the responses and only results in an unnecessary increase of computational costs.
- The back-coupling calculations play a more noticeable role in a convection-dominant process in comparison to a diffusion-dominant process.
- The process parameters are more sensitive to the flow velocity and thus convection than to the diffusion. Changes in the intensity of convection result in considerable changes in the concentration responses.
- The simulation results show a higher coating thickness at the boundaries of the foam and a decrease towards the centre. This behaviour has also been observed in the experiments.
- The comparison of the experimental and numerical results shows a very good qualitative agreement between the trends.
- A quantitative comparison of the coating thickness results shows small deviations between the simulation and experiment.

- The results show that an appropriate choice of boundary conditions is crucial for at least a qualitatively correct simulation of the experiment.

All in all, the model is capable of describing the process and the obtained simulation results were in an acceptable range in comparison to the experimental results.

6.2 Outlook

This model can be modified in future by modifying the initial simplifying assumptions and by taking into account the effects which were overlooked in this study.

Darcy's law in the current model was obtained based on the laminar flow assumption. However, the experimental results report a turbulent flow and hence the flow velocity can be improved by considering the turbulent flow behaviours and using the Brinkman or Forchheimer Equations.

Moreover, the magnitudes of the input parameters A_1 , A_2 , A_3 and a have been identified by numerical experimentation and according to the experimental results. These input parameters can be identified and related to the local physical quantities such as conductivity of the foam or electrical field. Knowing the physical meanings of these parameters, it will be possible to identify the best conditions to have a homogeneously coated foam. The optimum values of different influencing factors can be suggested and the electrodeposition process can be performed under the suggested conditions.

In the present study, the influence of the magnetic and electric forces has been neglected in the momentum balance. In future studies, the influence of the magnetic and electric fields in the applied body forces can be taken into account.

Thus, this study can be extended for future research and investigate the coating process with more details and from different aspects.

Bibliography

- [1] Z. Chen, G. Huan, and Y. Ma. *Computational methods for multiphase flows in porous media*. SIAM, 2006.
- [2] M.P. Lautenschlaeger, J. Weinmiller, B. Kellers, T. Danner, and A. Latz. Homogenized lattice boltzmann model for simulating multi-phase flows in heterogeneous porous media. *Advances in Water Resources*, 170: 104320, 2022.
- [3] J. Banhart. Manufacture, characterisation and application of cellular metals and metal foams. *Progress in materials science*, 46(6):559–632, 2001.
- [4] I. Duarte, N. Peixinho, A. Andrade-Campos, and R. Valente. Special issue on cellular materials. *Science and Technology of Materials*, 30(1): 1–3, 2018.
- [5] P.S. Liu and G.F. Chen. *Porous Materials: Processing and Applications*. Elsevier Science, 2014.
- [6] A. Jung and S. Diebels. Hybrid metal foams: experimental observations and phenomenological modelling. *Technische Mechanik-European Journal of Engineering Mechanics*, 34(1):12–22, 2014.
- [7] A. Jung and S. Diebels. Synthesis and mechanical properties of novel Ni/PU hybrid foams: a new economic composite material for energy absorbers. *Advanced Engineering Materials*, 18(4):532–541, 2016.
- [8] F. Kunz and A. Jung. Investigation of the structural coating homogeneity in open-porous Nickel/Polyurethane hybrid foams produced by flow-controlled electrodeposition. *Advanced Engineering Materials*, 24(11):2200262, 2022.

-
- [9] K.J. Euler. Die Änderung der Stromverteilung in porösen positiven Elektroden von Akkumulatoren und galvanischen Primärzellen während Ladung und Entladung. *Electrochimica Acta*, 13(7):1533–1549, 1968.
- [10] K.J. Euler. Stromverteilung in und auf porösen Elektroden. *Chemie Ingenieur Technik*, 37(6):626–631, 1965.
- [11] K.J. Euler. Spatial current distribution in non-isotropic conductors (with implication for porous electrodes). *Electrochimica Acta*, 18(5):385–387, 1973.
- [12] N. Ghiasi, A. Jung, and S. Diebels. Modelling the electrodeposition of Nickel on Polyurethane foam. *Continuum Mechanics and Thermodynamics*, Submitted, 2023.
- [13] C. Grill, M. Fries, A. Jung, and S. Diebels. Numerical and experimental investigations of the electrodeposition process on open porous foams, determination of the parameter influence on the coating homogeneity. *International Journal of Heat and Mass Transfer*, 180:121791, 2021.
- [14] R.M. Bowen, R.A. Grot, and G.A. Maugin. *Continuum Physics, volume III: Mixtures and EM Field Theories*. Academic Press, New York, San Francisco, London, 1976.
- [15] W. Ehlers and J. Bluhm. *Porous media: theory, experiments and numerical applications*. Springer Science & Business Media, 2002.
- [16] C. Truesdell and R. Toupin. The classical field theories. In S. Flügge, editor, *Principles of classical mechanics and field theory/Prinzipien der Klassischen Mechanik und Feldtheorie*, pages 226–858. Springer, New York, 1960.
- [17] G.M. Gladysz and K.K. Chawla. *Voids in materials: from unavoidable defects to designed cellular materials*. Elsevier, 2020.
- [18] A. Jung. *Offenporige, nanobeschichtete Hybrid-Metallschäume — Herstellung und mechanische Eigenschaften*. PhD thesis, 01 2012.
- [19] A. Jung and S. Diebels. Micromechanical characterization of metal foams. *Advanced Engineering Materials*, 21(8):1900237, 2019.
- [20] A. Jung, H. Natter, S. Diebels, E. Lach, and R. Hempelmann. Nanonickel coated aluminum foam for enhanced impact energy absorption. *Advanced Engineering Materials*, 13(1-2):23–28.

- [21] A. Jung, M.R. Koblichka, E. Lach, S. Diebels, and H. Natter. Hybrid metal foams: Mechanical testing and determination of mass flow limitations during electroplating. *Int. J. Mater. Sci.*, 2(1):97–107, 2012.
- [22] B.A. Bouwhuis, J.L. McCrea, G. Palumbo, and G.D. Hibbard. Mechanical properties of hybrid nanocrystalline metal foams. *Acta Materialia*, 57(14):4046–4053, 2009.
- [23] Y. Boonyongmaneerat, C.A. Schuh, and D.C. Dunand. Mechanical properties of reticulated aluminum foams with electrodeposited Ni–W coatings. *Scripta Materialia*, 59(3):336–339, 2008.
- [24] Y. Sun, R. Burgueño, A.J. Vanderklok, S.A. Tekalur, W. Wang, and I. Lee. Compressive behavior of aluminum/copper hybrid foams under high strain rate loading. *Materials Science and Engineering: A*, 592:111–120, 2014.
- [25] Y. Sun, R. Burgueño, W. Wang, and I. Lee. Effect of annealing on the mechanical properties of nano-copper reinforced open-cell aluminum foams. *Materials Science and Engineering: A*, 613:340–351, 2014.
- [26] Y. Sun, R. Burgueño, W. Wang, and I. Lee. Modeling and simulation of the quasi-static compressive behavior of Al/Cu hybrid open-cell foams. *international journal of solids and structures*, 54:135–146, 2015.
- [27] K. Terzaghi. *Erdbaumechanik auf bodenphysikalischer Grundlage*. F. Deuticke, 1925.
- [28] R. De Boer. *Theory of porous media: Highlights in historical development and current state*. Springer Science & Business Media, 2012.
- [29] M.A. Biot. General theory of three-dimensional consolidation. *Journal of applied physics*, 12(2):155–164, 1941.
- [30] M. Hassanizadeh. Derivation of basic equations of mass transport in porous media, part 1. Macroscopic balance laws. *Advances in Water Resources*, 9(4):196–206, 1986.
- [31] M. Hassanizadeh. Derivation of basic equations of mass transport in porous media, part 2. Generalized Darcy’s and Fick’s laws. *Advances in water resources*, 9(4):207–222, 1986.
- [32] M. Hassanizadeh and W.G. Gray. General conservation equations for multi-phase systems: 1. Averaging procedure. *Advances in water resources*, 2:131–144, 1979.

- [33] M. Hassanizadeh and W.G. Gray. General conservation equations for multi-phase systems: 2. Mass, momenta, energy, and entropy equations. *Advances in water resources*, 2:191–203, 1979.
- [34] M. Hassanizadeh and W.G. Gray. General conservation equations for multi-phase systems: 3. Constitutive theory for porous media flow. *Advances in water resources*, 3(1):25–40, 1980.
- [35] W.G. Gray. General conservation equations for multi-phase systems: 4. Constitutive theory including phase change. *Advances in water resources*, 6(3):130–140, 1983.
- [36] M. Miyan and P.K. Pant. Flow and diffusion equations for fluid flow in porous rocks for the multiphase flow phenomena. *American Journal of Engineering Research (AJER)*, 4(7):139–148, 2015.
- [37] K. Hiltunen, A. Jäsberg, S. Kallio, H. Karema, M. Kataja, A. Koponen, M. Manninen, and V. Taivassalo. Multiphase flow dynamics. *Theory and Numerics. Tech. Rep*, 722, 2009.
- [38] C. Truesdell. Sulle basi della termomeccanica. *Rend. Lincei*, 22(8):33–38, 1957.
- [39] C. Truesdell, I. Liu, and I. Müller. *Thermodynamics of mixtures of fluids*. Springer, 1984.
- [40] C. Truesdell and W. Noll. *The non-linear field theories of mechanics*. Springer, 2004.
- [41] K. Wilmanski. *Thermomechanics of continua*. Springer Science & Business Media, 2012.
- [42] I. Muller. Rational thermodynamics of mixtures of fluids, thermodynamics and constitutive equations. *Lecture Notes in Physics*, 228, 1985.
- [43] P. Sharma and S. Diebels. A mixture theory for the moisture transport in polyamide. *Continuum Mechanics and Thermodynamics*, 33(4):1891–1905, 2021.
- [44] M. Manninen, V. Taivassalo, and S. Kallio. On the mixture model for multiphase flow. 1996.
- [45] K. Hiltunen, A. Jäsberg, S. Kallio, H. Karema, M. Kataja, A. Koponen, M. Manninen, and V. Taivassalo. Multiphase flow dynamics theory and numerics. *VTT Technical Research Centre of Finland, Vuorimiehentie*, 3.

- [46] T. Ricken, A. Schwarz, and J. Bluhm. A triphasic theory for growth in biological tissue—basics and applications. *Materialwissenschaft und Werkstofftechnik: Entwicklung, Fertigung, Prüfung, Eigenschaften und Anwendungen technischer Werkstoffe*, 37(6):446–456, 2006.
- [47] G. Del Bufalo, L. Placidi, and M. Porfiri. A mixture theory framework for modeling the mechanical actuation of ionic polymer metal composites. *Smart Materials and Structures*, 17(4):045010, 2008.
- [48] S. Diebels. Mikropolare Zweiphasenmodelle: Modellierung auf der Basis der Theorie Poröser Medien. 2000.
- [49] S. Diebels. A micropolar theory of porous media: Constitutive modelling. *Transport in Porous Media*, 34:193–208, 1999.
- [50] M.R. Hughes, N. Strussevitch, C. Bailey, K. McManus, J.G. Kaufmann, D. Flynn, and M.P.Y. Desmulliez. Numerical algorithms for modelling electrodeposition: Tracking the deposition front under forced convection from megasonic agitation. *International Journal for Numerical Methods in Fluids*, 64:237–268, 2010.
- [51] V. Joeekar-Niasar, L. Schreyer, M. Sedighi, M. Icardi, and J. Huyghe. Coupled processes in charged porous media: From theory to applications. *Transport in Porous Media*, 130(1):183–214, 2019.
- [52] C. Grill, A. Jung, and S. Diebels. Modelling and simulation of the coating process on open porous metal foams. *PAMM*, 18(1):e201800254, 2018.
- [53] C. Grill, A. Jung, and S. Diebels. Investigation of the electrodeposition parameters on the coating process on open porous media. *PAMM*, 19(1):e201900106, 2019.
- [54] S. Diebels. *Micropolar mixture models on the basis of the theory of porous media*. Springer, 2002.
- [55] P. Haupt. *Continuum mechanics and theory of materials*. Springer Science & Business Media, 2002.
- [56] W.M. Lai, D. Rubin, and E. Krempl. *Introduction to continuum mechanics*. Butterworth-Heinemann, 2009.
- [57] J.I. Siddique, A. Ahmed, A. Aziz, and C.M. Khaliq. A review of mixture theory for deformable porous media and applications. *Applied Sciences*, 7(9):917, 2017.

- [58] W.B. Fulks, R.B. Guenther, and E.L. Roetman. Equations of motion and continuity for fluid flow in a porous medium. *Acta Mechanica*, 12(1):121–129, 1971.
- [59] J. Newman and N.P. Balsara. *Electrochemical systems*. John Wiley & Sons, 2021.
- [60] J.J. Jasielec. Electrodiffusion phenomena in neuroscience and the Nernst–Planck–Poisson equations. *Electrochem*, 2(2):197–215, 2021.
- [61] H. Cohen and J.W. Cooley. The numerical solution of the time-dependent Nernst-Planck equations. *Biophysical Journal*, 5(2):145–162, 1965.
- [62] M. Kamata and M. Paku. Exploring Faraday’s law of electrolysis using Zinc–Air batteries with current regulative diodes. *Journal of chemical education*, 84(4):674, 2007.
- [63] A. Mahapatro and S.K. Suggu. Modeling and simulation of electrodeposition: Effect of electrolyte current density and conductivity on electroplating thickness. *Adv. Mater. Sci*, 3(2):1, 2018.
- [64] J. Kauffman, J. Gilbert, and E. Paterson. Multi-physics modeling of electrochemical deposition. *Fluids*, 5(4):240, 2020.
- [65] D.A. Noren and M.A. Hoffman. Clarifying the Butler–Volmer equation and related approximations for calculating activation losses in solid oxide fuel cell models. *Journal of Power Sources*, 152:175–181, 2005.
- [66] E.J.F. Dickinson and A.J. Wain. The Butler-Volmer equation in electrochemical theory: Origins, value, and practical application. *Journal of Electroanalytical Chemistry*, 872:114145, 2020.
- [67] J. Hommel, E. Coltman, and H. Class. Porosity–permeability relations for evolving pore space: A review with a focus on (bio-) geochemically altered porous media. *Transport in Porous Media*, 124(2):589–629, 2018.
- [68] Z. Li, Z. Qiao, and T. Tang. *Numerical solution of differential equations: Introduction to finite difference and finite element methods*. Cambridge University Press, 2017.
- [69] M.H. Holmes. *Introduction to numerical methods in differential equations*. Springer, 2007.

- [70] R.J. LeVeque. Finite difference methods for differential equations. *Draft version for use in AMath*, 585(6):112, 1998.
- [71] W.F. Ames. *Numerical methods for partial differential equations*. Academic press, 2014.
- [72] W.H. Hundsdorfer and J.G. Verwer. *Numerical solution of time-dependent advection-diffusion-reaction equations*, volume 33. Springer, 2003.
- [73] G.D. Smith. *Numerical solution of partial differential equations: finite difference methods*. Oxford university press, 1985.
- [74] J.C. Butcher. *Numerical methods for ordinary differential equations*. John Wiley & Sons, 2016.
- [75] J.W. Thomas. *Numerical partial differential equations: finite difference methods*, volume 22. Springer Science & Business Media, 2013.
- [76] H.G. Roos. *Robust numerical methods for singularly perturbed differential equations*. Springer, 2008.
- [77] E. Kreyszig, K. Stroud, and G. Stephenson. Advanced engineering mathematics. *Integration*, 9(4), 2008.
- [78] J. Crank. *The mathematics of diffusion*. Oxford university press, 1979.
- [79] H. Sato, M. Yui, and H. Yoshikawa. Ionic diffusion coefficients of Cs^+ , Pb^{2+} , Sm^{3+} , Ni^{2+} , SeO_4^{2-} and TcO_4^- in free water determined from conductivity measurements. *Journal of Nuclear Science and Technology*, 33(12):950–955, 1996.
- [80] A.J. Bard, L.R. Faulkner, et al. Fundamentals and applications. *Electrochemical methods*, 2(482):580–632, 2001.
- [81] N. Ghiasi, F. Kunz, A. Jung, and S. Diebels. A 2-dimensional modelling of the coating process of Nickel on Polyurethane foam via electrodeposition. *Journal of Porous Materials*, Submitted, 2024.
- [82] Tzayam Pérez, Luis F Arenas, Daniel Villalobos-Lara, Nan Zhou, Shuncai Wang, Frank C Walsh, José L Nava, and Carlos Ponce de León. Simulations of fluid flow, mass transport and current distribution in a parallel plate flow cell during nickel electrodeposition. *Journal of Electroanalytical Chemistry*, 873:114359, 2020.

Appendix

A Publications

- **N. Ghiasi**, A. Jung, & S. Diebels (2023). Modelling the electrodeposition of Nickel on Polyurethane foam. *Continuum Mechanics and Thermodynamics*, Submitted.
- **N. Ghiasi**, F. Kunz, A. Jung, & S. Diebels (2024). A 2-dimensional modelling of the coating process of Nickel on Polyurethane foam via electrodeposition. *Journal of Porous Materials*, Submitted.

B Presentations

- **N. Ghiasi** & S. Diebels (Jul. 2022). "Numerical modelling of Nickel electrodeposition on Polyurethane foams". Advanced Computational Engineering and Experimenting (ACEX2022) conference, Florence, Italy.
- **N. Ghiasi** & S. Diebels (Jul. 2022). "Considering the incompressibility of electrolyte and developing a new model for coating process of Ni/PU foams". Mechanics Today workshop, Oberwesel, Germany.
- **N. Ghiasi** & S. Diebels (Sep. 2022). "Numerical modelling of the Ni/PU hybrid foams coating process". 14th Continuum Mechanics Workshop, Travemünde, Germany.

- **N. Ghiasi** & S. Diebels (Jun. 2023). "Numerical modelling of Nickel electrodeposition on Polyurethane foams". Coupled-2023 conference, Chania, Crete, Greece.

C Poster Presentation

- **N. Ghiasi** & S. Diebels (Nov. 2021). "Numerical modelling of the coating process of Ni/PU hybrid foams". Doktorandentag der Naturwissenschaftlich Technischen Fakultät III der Universität des Saarlandes.